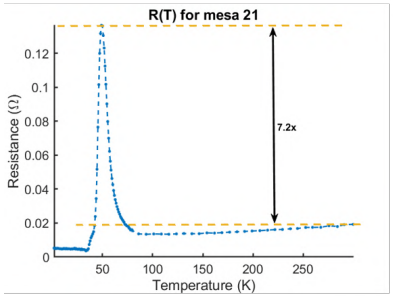

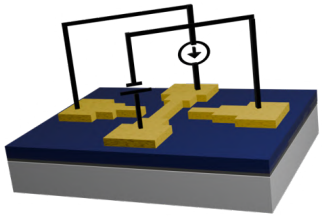

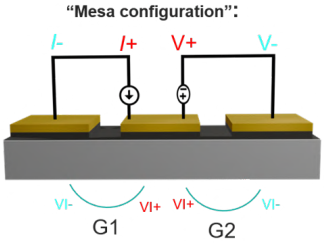

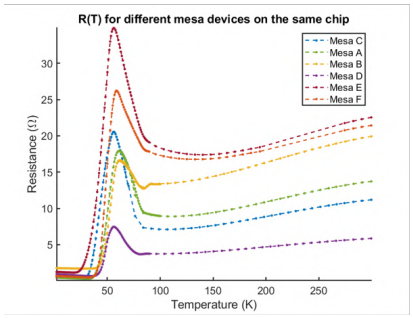

"Groove configurations":

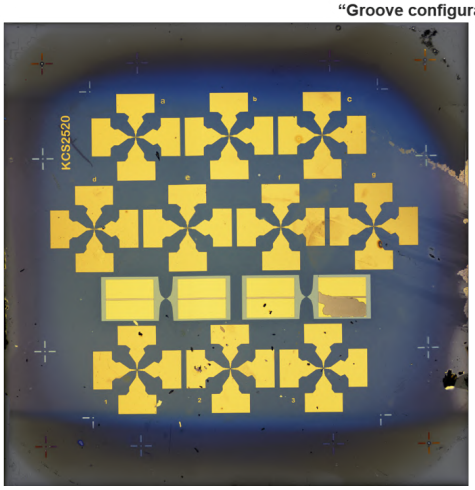

C-axis transport in YBCO nanostructures

Erasmus Mundus (EMM-Nano) - Master's thesis in Nanotechnology and Nanoscience

KLINTI SINOJMERI

DEPARTMENT OF MICROTECHNOLOGY AND NANOSCIENCE

CHALMERS UNIVERSITY OF TECHNOLOGY AND KU LEUVEN
Gothenburg, Sweden 2025
www.chalmers.se • www.kuleuven.be

Master's Thesis 2025

C-axis transport in YBCO nanostructures

KLINTI SINOJMERI

CHALMERS
UNIVERSITY OF TECHNOLOGY

Chalmers University of Technology

KU Leuven

Department of Microtechnology and Nanoscience
Division of Quantum Device Physics
Quantum Materials and Nanodevices (QManD)
Chalmers University of Technology
Gothenburg, Sweden 2025

C-axis transport in YBCO nanostructures
KLINTI SINOJMERI

Supervisors: Thilo Bauch, Floriana Lombardi and Alessia Garibaldi
Co-supervisor: Bart Soree
Department of Microtechnology and Nanoscience
Examiner: Thilo Bauch, Department of Microtechnology and Nanoscience

Master's Thesis 2025
Department of Microtechnology and Nanoscience
Erasmus Mundus Master of Science in Nanotechnology and Nanoscience - Quantum Computing Track
Division of Quantum Device Physics
Quantum Materials and Nanodevices (QManD)
Chalmers University of Technology
SE-412 96 Gothenburg
Telephone +46 31 772 1000

Cover: The sketch illustrates the single-lithography and three-lithography mesa designs, alongside the measurement setup. The plots on the left-hand side depict two key experimental results: the $R(T)$ behavior for c-axis transport in a single-lithography mesa and a summary of c-axis behavior in the three-lithography mesas.

Printed by Chalmers Reproservice
Gothenburg, Sweden 2025

C-axis transport in YBCO nanostructures
KLINTI SINOJMERI
Department of Microtechnology and Nanoscience
Chalmers University of Technology

Abstract

Despite nearly four decades since the discovery of high-temperature superconductivity (HTS) in cuprates, the underlying microscopic mechanisms remain one of the most profound open questions, in Condensed Matter Physics. The presence of multiple, intertwined electronic orders, driven by strong electron-electron correlations, adds further complexity to their behavior. This is reflected by a highly intricate phase diagram. Specifically we focus on $YBa_2Cu_3O_{7-\delta}$ (YBCO), as our choice of HTS.

While in-plane transport (ab-plane) has been extensively studied, little is known about the out-of-plane (c-axis) transport, especially in thin film systems. This is due to the challenges associated with growing the film in other, suitable orientations (most convenient and highest quality YBCO films are c-axis oriented) or fabricating suitable nanostructures to probe it. In addition, the out-of-plane conduction pathway is significantly more resistive than the in-plane one.

Despite these challenges, thin film platforms offer the ability to investigate properties that are inaccessible in bulk, single crystals. Modifications of the YBCO ground state by an engineered superpotential can only manifest in thin film systems, where the substrate morphology has been patterned into a superstructure (for example, nanofacets). This superpotential has been shown to induce changes such as enhancement of superconductivity, unidirectional Charge-Density Wave (CDW) and even nematicity. Therefore, developing a platform to gain access to c-axis transport properties in thin films (where the effect of such superpotential modifications on c-axis can also be observed) offers a complementary perspective to the ab-plane studies. Together, they may hold the key to unlocking the mystery of HTS.

Previous studies on c-axis transport in YBCO are mostly performed on bulk single crystals. They have revealed that charge transport along the c-axis differs fundamentally from that in the ab-plane. In underdoped samples, a crossover from metallic to semiconducting behavior is observed with decreasing temperature. This behavior could be related with the opening of the pseudogap. Moreover, the anisotropy between the in-plane and out-of-plane responses becomes more pronounced at lower dopings, suggesting a quasi-two-dimensional character.

This thesis focuses on creating a reliable platform for probing the out-of-plane transport by mesa devices. These devices are made on thin film YBCO, which is grown by pulsed-laser-deposition (PLD). Furthermore, we describe two fabrication routes for the mesa devices using single-lithography (but with larger areas), or by utilizing a more intricate three-lithography method, which grants much smaller areas. Then we use them to probe the c-axis transport on 50nm thick, YBCO films.

Keywords: HTS, YBCO thin films, c-axis transport, underdoped, mesa

Acknowledgements

First and foremost, I would like to express my heartfelt gratitude to my supervisors, Thilo Bauch and Floriana Lombardi, for warmly welcoming me into the group and giving me the opportunity to work on such a fascinating topic, one that has truly sparked my passion for pursuing an academic career. Your combined guidance, encouragement, and belief in me have helped me a lot. I'm especially grateful for the time you always found (no matter how busy you were) to listen to my ideas, answer my many questions, and discuss results or theories in great depth. Thilo, your thoughtful explanations and brilliant comments, have been really important to me. Floriana, I am deeply thankful for your passion, creative ideas, encouragement, and the energy you bring to every discussion. Beyond your scientific insight, I truly appreciate the warm encouragement you gave me during more difficult stages of the project. Working under you both, has been motivating in a way that goes beyond the pages of this thesis.

I also wish to thank Alexei Kalaboukhov for your help and guidance in operating deposition and characterization tools, as well as for sharing the practical skills, tips, and tricks that helped me grow into a more capable and confident experimentalist. Your expertise and patience have left a lasting mark on my approach to experimental work.

I am equally grateful to Riccardo Arpaia. Although I did not have the chance to work with you directly throughout most of my thesis, I truly appreciated your help in interpreting my measurement results during the Summer (and for the very nice midnight chat. It was both very fun and very insightful). Thanks to your explanations, I learned a great deal about new and fascinating phenomena. I look forward to, and will always welcome, your advice and guidance as I continue my academic journey.

Special thanks are also due to the other members of the group, whose help, camaraderie, and kindness I will always remember. Working in a place full of brilliant and genuinely wonderful people has truly been a privilege.

I am especially grateful to Karn Rongrueangkul, who first introduced me to the cleanroom and the PLD machine, and for the fun we had working together. The countless discussions and jokes we have shared together, have made this journey incredibly fun! During hard times, your kindness and generosity have meant a lot.

I also wish to thank Kiryl Niherysh for his advice and insights on fabrication, as well as for his steady support throughout this journey.

Everyone in the group has been incredibly welcoming, and I truly feel lucky to have been part of such an amazing team.

I would also like to thank my newfound friends Lars Sjöström (who has the best and most impeccable comedic timing for some reason. You always passed by at the best moments possible (and sometimes gave silent judgements)), Roselle Ngaloy (you were being such a ray of sunshine always. Though seriously, thanks a lot for the jokes, support and being there. You are a very, very good friend), Maha Khademi (the nicest and kindest person of them all), and Adithi Udupa (my good friend during Summer for all the kitchen and coffee breaks. Thank you for being there during the lonely Summer period). Thanks a lot everybody. The conversations, stories, and laughter we shared during kitchen breaks made this journey not only easier, but also much more fun and memorable.

Of course, I cannot stay without mentioning the person who played the biggest part in my thesis, and this master journey, Alessia Garibaldi. Officially my daily advisor, but in reality so much more. Honestly, there's enough to say about you that I could fill several pages, but I'll try to keep it short. You taught me everything I know about the cleanroom,

nanofabrication, measurements, and most importantly, how to think like a researcher. You've been there with me from the very beginning of my journey (when I was a shy nerd with trembling hands failing to load the PLD) to where I am today (where you "kick me off" to get new licenses). You listened to all of my wild theories, entertained my ideas, and supported me through both the good times and the tough ones.
All of our adventures, jokes, discussions, lunches and dinners, post-midnight sessions, after-credits moments, walks home and hours of gossip, I will cherish them all. I am truly lucky to have worked with a researcher (and person) like you. Team Mesa wouldn't have existed without you, Second Brain and Speed/buddy/brothe'/partner in crime. You made everything better and a whole lot more fun (I can fully say, it is the best to work with you).

Finally, I would like to thank my family, who have been my unwavering support for as long as I can remember. Even during the most difficult times, the three of you have been there for me without hesitation. A special mention goes to my father, for being a steadfast pillar of support in both good and challenging times. I could not have made it this far without all of your love and encouragement.

Klinti Sinojmeri, Gothenburg, August 2025

List of Acronyms

Below is the list of acronyms that have been used throughout this thesis listed in alphabetical order:

AF	Antiferromagnetic
ARPES	Angle-resolved photoemission spectroscopy
BCS	Bardeen–Cooper–Schrieffer
BSCCO/Bi2212	$Bi_2Sr_2CaCu_2O_{8+x}$
C_4	Four-fold rotational symmetry
CDW	Charge Density Wave
$d_{x^2-y^2}$	d-Wave Order Parameter
e-ph	Electron-Phonon Coupling
HTS	High-Temperature Superconductivity
LBCO	$La_{2-x}Ba_xCuO_4$
LSCO	$La_{2-x}Sr_xCuO_4$
PLD	Pulsed laser deposition
RIXS	Resonant Inelastic X-ray Scattering
SEM	Scanning Electron Microscope
STM	Scanning Tunning Microscope
YBCO	$YBa_2Cu_3O_{7-\delta}$
PDW	Pair Density Wave

Parameters

Δ	Superconducting Energy Gap
ΔT_c	A parameter that shows the broadening of the superconducting transition
B_c	Critical Magnetic Field
J_s	Supercurrent Density
K_B	Boltzmann constant
n_s	Superconducting Electron Density
T_c	Critical Temperature
T_c^{on}	Onset of the superconducting transition
Λ	London Parameter
λ_L	London Penetration Depth
μ_0	Vacuum permeability
ξ	coherence length
ψ	Order Parameter
ω_D	Debye Frequency

Contents

List of Figures

List of Tables

1
Introduction

Superconductivity is one of the most important and intriguing phenomena in Condensed Matter Physics. In this field, in 1986, a major milestone was reached with the discovery of the first high-temperature superconductor (HTS), which exhibited a critical temperature (T_c) of 30K [5]. This breakthrough challenged the current understanding at the time, which had been established by the Bardeen-Cooper-Schrieffer's (BCS) microscopic theory. Up to this point, that theory had provided a successful framework for low-temperature, conventional superconductivity [6]. The material responsible for this great leap forward, belonged to the family of ceramic cooper-oxides (referred to as cuprates later on). Since then, the search for new superconductors with even higher even higher T_c began [7, 8]. The ultimate goal of this research is the discovery of the room-temperature superconductor, a breakthrough that would revolutionize modern technology. Despite substantial progress over the past decades, there is still a lack of a complete microscopic theory to explain the underlying mechanisms behind HTS. This continues to limit the practical application of these materials.

Such a difficulty arises from the strongly correlated electrons in these materials, where the traditional single-particle approximation breaks down. Therefore, it is unable to accurately describe the system's behavior [9, 10]. Current computational methods, even with supercomputers, struggle to model these strong electron-electron correlations with enough precision to predict the properties of HTS compounds. Over the past decades, numerous theoretical models have been proposed to decode the underlying mechanisms driving superconductivity in HTS [11–17], yet no single framework has succeeded in capturing its full complexity.

Beyond their unconventional superconducting behavior, the normal state of cuprates introduces additional layers of complexity. Due to pronounced electron-electron interactions, various forms of spin and charge orders emerge, contributing to a rich and intricate electronic phase diagram [10]. Although the precise origin of these local orders remains elusive, some theoretical studies suggest that they may be connected with the superconducting phase itself [18]. A particularly interesting region in the cuprates' phase diagram lies is the pseudogap phase, located in the underdoped regime. As its name implies, this phase is marked by a partial suppression of the electronic density of states, specifically along the anti-nodal directions of the Fermi-Surface [19, 20]. The consequence is a transformation from the continuous hole-like cylindrical Fermi surface, to disconnected segments known as Fermi arcs [21–23]. Two important quantities characterize this phase, the critical doping p^* and the onset temperature T^*. Despite decades of research, the precise connection between the pseudogap and superconductivity remains an open question. Some experimental and theoretical works suggest a competitive interplay, noting that the emergence of d-wave superconductivity near T_c coincides with the collapse of the Fermi arcs close to the nodal regions [24]. In contrast, other studies propose a precursor scenario where the pseudogap contains pre-formed Cooper pairs lacking phase coherence

[20, 25–27]. Up to this day, the pseudogap stands as one of the central and most enduring mysteries of HTS.

In our context, out-of-plane (c-axis) transport offers a particularly powerful probe of the pseudogap region. C-axis conduction depends on the anti-nodal states, the very states suppressed by the opening of the pseudogap. This makes transport along this direction very sensitive to the pseudogap or modifications of the anti-nodal states [19, 28]. Most studies in c-axis transport have been done in single crystals. However, recent developments in thin films (such as superpotentials induced via substrate effects, like nanofacets in MgO (110) [29]) have shown the ability to modify the ground state of superconductors ($YBa_2Cu_3O_{7-\delta}$ (YBCO) for example). One of the consequences of this modifications, is inducing a nematic transformation to the Fermi Surface. Therefore, it becomes important to have a c-axis platform on thin films, as it can be used to indirectly probe nematicity. A nematic distortion of the Fermi surface would lead to an additional suppression of the anti-nodal states [29, 30], leaving a distinct fingerprint in the c-axis transport.

1.1 Thesis Objectives and Scope

In this thesis, we focus on the c-axis transport properties of YBCO, a very well-studied HTS. Our ultimate goal, is to investigate c-axis transport in thin film YBCO nanostructures, where its ground state properties have been modified by the presence of a superpotential. That said, there are several difficulties with probing c-axis transport in thin film systems. Therefore, in this specific work, we focus on creating a reliable platform for probing the c-axis, and comparing our measurements with results reported in single-crystal systems.

Our investigation is carried out in the underoped regime of YBCO, with a hole concentration of $p \approx 0.11$ and an average superconducting transition temperature ($\bar{T}_c$) in the range of 52-55K. At higher doping levels, YBCO exhibits more three-dimensional superconducting behavior, while in the underdoped regime, its quasi-two-dimensional nature and transport anisotropy are more pronounced.

In-plane transport has been extensively studied in the past (in both thin film and single crystal platforms), partly due to its strong connections with superconductivity originating in the CuO_2 planes. In contrast, much less is known about c-axis transport, especially in thin film systems. This knowledge gap stems from inherent challenges associated with measuring along the c-axis, the main one being to fabricate suitable nanostructures for such measurements. To mention some of these difficulties are:

1. Establish reliable electrical contact from the top.
2. Small device areas are required to obtain measurable resistances
3. Out-of-plane conduction is inherently less favorable, making it highly sensitive to structural or process-induced damage.

One could in principle grow the films in another orientation to study c-axis transport, however, in the experience of our group this is quite a complicated process [31] as well. In addition, it prevents us from having the tunability over the material's properties by superstructure effects, which is the ultimate goal of our investigation. An example of this superstructure are the nanofacets on MgO(110) created by modifying the substrate's morphology by annealing [29, 30, 32, 33]. Such tunability and control over the material's properties, is invaluable for disentangling the intertwined orders present in the intricate phase diagram of cuprates, thereby deepening our understanding of their fundamental

properties. As two examples that are only available in thin film platforms, are the nematic transformation of the Fermi surface or the unidirectional Charge-Density Wave (CDW), which occur only in ultrathin films (10nm), modified by the nanofacets [30, 32]. This ground state modifications also lead to enhanced superconducting properties. Such effects are not accessible for bulk single crystals. In addition, we can indirectly probe the nematicity of the Fermi Surface, and look for any modifications to the pseudogap phase. Thin films also provide additional insight (compared to single crystal results), as they do induce confinement effects. Combining c-axis knowledge with in-plane measurements, could be the key elements to unraveling the mystery behind HTS.

For testing our measurement platform, we will be focusing on probing the behavior of underdoped YBCO thin films within the pseudogap regime.

Experimentally, the pseudogap manifests in Resistance versus Temperature ($R(T)$ measurements below the characteristic temperature T^*. Below this temperature, the in-plane resistance decreases, despite the opening of an energy gap, a counterintuitive behavior commonly observed in underdoped YBCO [34].

In c-axis transport studies for bulk single crystals [28], a crossover from metallic to semiconducting behavior has been observed with decreasing temperature. This change is often linked to the opening of the pseudogap. Notably, T^* (associated with the onset of in-plane pseudogap behavior) is lower than T' (the temperature at which an upturn in c-axis resistance occurs). There are many theories attempting to explain this disparity, such as the Resonance Valence Band (RVB) model [17]. In this work, we expect to observe a similar transition from metallic to semiconducting behavior in our out-of-plane transport measurements and look for any hints of anisotropic signatures through the differing values for ab-plane and c-axis transport.

Another objective of this thesis is to characterize the YBCO-Au interface (superconductor-normal metal (SN)), using conductance spectroscopy, for underdoped samples. This technique provides information about the symmetry of the superconducting order parameter and the possible presence of subgap features, Zero-Bias Conductance Peaks (ZBCPs), Andreev reflections, zero energy Andreev Bound States (ABS). All of these phenomena are essential for understanding charge transport across the boundary. Understanding these phenomena is not only critical from a fundamental physics standpoint, but also for the development and optimization of quantum devices, where such interfaces play a pivotal role. More importantly, we can search for any modulations to gap features, that can be induced by the presence of a superpotential in the substrate.

The structure of this thesis is organized as follows:

- **Chapter 2** provides a brief overview of the history of superconductivity and HTS, including key properties of YBCO such as its electronic phase diagram, nematicity, some brief background on Andreev Physics
- **Chapter 3** describes the YBCO thin film deposition and its electrical characterization
- **Chapter 4** presents a detailed overview of the nanofabrication process used to define YBCO mesa devices with a thickness of 50nm. The first section discusses the fabrication of 100×100 μm^2-area mesas and their limitations. The second sections explores the miniaturization to 10×10 μm^2-area mesas, requiring a more intricate fabrication process
- **Chapter 5** explains the types of measurements conducted on the mesa devices for investigating c-axis transport, the experimental setup and theoretical calculations
- **Chapter 6** discusses the experimental results of c-axis transport measurements.

The first section focuses on the 100×100 μm^2-area devices, while the second on the 10×10 μm^2-area mesas. During this second section, a comparison with nanobridge measurements (fabricated on the same chip) as representatives of ab-plane transport is also presented

- **Chapter 7** concludes the thesis by summarizing the key findings, and proposing directions for future research

2
Background

This chapter provides an essential foundation about superconductivity. The first part offers a brief historical summary of key developments and fundamental laws that govern superconductors. The second part focuses on unconventional superconductors, also called HTS. Particularly describing cuprates, specifically YBCO and its complex phase diagrams. This information will form the basis to comprehend the work presented in this thesis.

2.1 History of Superconductivity

Superconductivity was first discovered in 1911 by Onnes in Leiden. He was able to measure the electrical resistivity of mercury as a function of temperature using liquid helium [35]. In his experiment, the resistivity of mercury vanished abruptly at 4.2 K (a superconducting transition occurred). The temperature at which a material undergoes this phase transition to a zero resistive state, is known as the critical temperature, T_c. Materials who exhibit this property are called superconductors.

A second essential property to classify a material as a superconductor, is perfect diamagnetism. It was discovered in 1933 by Meissner and Ochsenfeld [36]. When a superconductor is cooled below T_c (even in the presence of a magnetic field), it will expel all external magnetic fields from their interior. In their honor, this phenomenon was named the Meissner effect. It is what distinguishes superconductors from perfect conductors. The Meissner effect can be broken not only by temperature, but also if the applied magnetic field exceeds a critical field H_c, which is material specific.

In 1935, the London brothers developed the first electrodynamic theory of superconductivity, introducing what nowadays are known as the London equations [37]. The superconducting state was modeled as a two-fluid system, consisting of a superfluid. Its carriers were superelectrons with zero viscosity and entropy. And the other part was a normal fluid with regular electrons. The London equations are:

$$\vec{E} = \Lambda \frac{\partial \vec{J}_s}{\partial t} \tag{2.1}$$

$$\vec{B} = -\Lambda \nabla \times \vec{J}_s \tag{2.2}$$

where $\Lambda = \frac{m^*}{n_s e^{*2}}$ is the London parameter, $m^* = 2m$ and $e^* = 2e$ represent the effective mass and charge of the superconducting charge carriers (later called Cooper pairs after BCS), and n_s is the carrier density of these superelectrons. Equation (2.1) describes the dissipationless current of the superconducting state, while equation (2.2) accounts for the expulsion of magnetic fields (explains the Meissner effect). By using Ampere's law, $\nabla \times \vec{B} = \mu_0 \vec{J}_s$, and substituting into equation (2.2), one can obtain:

$$\nabla^2 \vec{B} = \frac{1}{\lambda_L^2} \vec{B}, \qquad \lambda_L = \sqrt{\frac{\Lambda}{\mu_0}} \tag{2.3}$$

where λ_L is known as the London penetration depth. This is a very important, characteristic length scale that describes the extent to which a magnetic field can penetrate into a superconductor.

Although the London equations were able to describe two essential features of superconductivity, they weren't able to account for all properties of superconductors. Therefore, a more comprehensive phenomenological theory was proposed by Ginzburg and Landau in 1950 [38]. It is a thermodynamical theory, based on phase transitions (superconductivity is second order phase transition). Ginzburg–Landau (GL) theory introduces a complex order parameter $\psi(\vec{r}) = |\psi(\vec{r})|e^{i\theta}$, where $|\psi|^2 = n_s$ is the density of superconducting carriers. Using GL formalism, the free energy of the system is expressed as:

$$F = F_N + \int \left[\alpha|\psi|^2 + \frac{1}{2}\beta|\psi|^4 + \frac{1}{2m} \left| \left(-i\hbar\nabla - e^* \vec{A}\right) \psi \right|^2 + \frac{1}{2\mu_0}|\vec{B}|^2 \right] dV \tag{2.4}$$

where F_N is the free energy of the normal state, $\vec{A}$ is the magnetic vector potential, and α, β are the phenomenological parameters related to the system's thermodynamics. Minimizing the free energy with respect to ψ^* or $\vec{A}$ leads to the two GL equations:

$$\alpha\psi + \beta|\psi|^2\psi + \frac{1}{2m}\left(-i\hbar\nabla - e^*\vec{A}\right)^2 \psi = 0 \tag{2.5}$$

$$\vec{J_s} = -\frac{ie^*\hbar}{2m}\left(\psi^*\nabla\psi - \psi\nabla\psi^*\right) - \frac{(e^*)^2}{m}|\psi|^2\vec{A} \tag{2.6}$$

This theory was a great success in describing the macroscopic properties of superconductors. It is also possible to re-derive the London equations, from the 2 GL equations. The boundary condition associated with these equations, $(-i\hbar\nabla\psi - e^*\vec{A}\psi) \cdot \vec{n} = 0$, implies that the supercurrent $\vec{J_s}$ cannot exit the superconducting material, which is quite logical.

From equation (2.5), a second characteristic length scale was discovered. This was the coherence length ξ and it can easily be derived by assuming the Rigid Gauge (superfluid phase θ is constant), negligible magnetic field, and a slowly varying, real-valued ψ. The equation reduces to:

$$\nabla^2\psi = \frac{\psi}{\xi^2}, \qquad \xi = \sqrt{\frac{\hbar^2}{2m|\alpha|}} \tag{2.7}$$

By combining the 2 characteristic lengths, a dimensionless ratio $\kappa = \lambda_L/\xi$ was discovered. This is used to classify superconductors into two types: Type I ($\kappa < 1/\sqrt{2}$), where magnetic flux is completely expelled up to H_c, and Type II ($\kappa > 1/\sqrt{2}$). Type II allow for partial flux penetration through Abrikosov vortices in their mixed state ($H_{c1} < H_< H_{c2}$. The vortices were called Abrikosov vortices, as the theoretical basis for their behavior in Type II superconductors was developed by Abrikosov in 1957 [39]. In such materials, flux enters the superconductor during the mixed state $H_{c1} < H < H_{c2}$. Below H_{c1} the system is in the Meissner state and acts a perfect diamagnet, while above H_{c2} superconductivity is broken.

2.1.1 Microscopic Theory - BCS

Another important experimental milestone occurred in 1950, when E. Maxwell observed that the critical temperature of mercury changed with the isotope mass [40]. This isotope effect hinted at a connection between lattice vibrations (phonons) and superconductivity. Independently, Fröhlich [41] and Bardeen [42] proposed that electron-phonon (e-ph) interactions played a fundamental role in the formation of the superconducting state. The observed relation $T_c \propto M^{-1/2}$, where M is the isotope's mass, supported this view, as phonon frequencies also scaled with $M^{-1/2}$.

Building on all of these developments, Bardeen, Cooper, and Schrieffer formulated the first microscopic theory of superconductivity in 1957. This was known as the BCS theory [43, 44]. The central idea is that in certain materials, there is an attractive interaction between electrons, mediated by phonons (could also be another kind of boson, but experimental data due to the isotope effect, suggests phonons). This attractive interaction is strong enough, that it can overcome Coulombic repulsion. Such an attractive potential, leads to the formation of correlated electron pairs (Cooper pairs), with opposite spin and momentum (this gives the maximum overlap between the Fermi surfaces of the two pairing-electrons). These pairs can then condense into a macroscopic quantum state below T_c.

Under the BCS framework, the density of states near the Fermi level is assumed constant, $N(\varepsilon_F) = N_0$, and the interaction potential, matrix element is approximated as constant (no momentum dependence), $V_{kk'} = V_0$, within an energy window determined by the Debye frequency ω_D. These approximations are referred to as the weak-coupling limit and are valid for conventional, low temperature superconductors with s-wave order parameter. The superconducting gap Δ at zero temperature can be derived as:

$$k_B T_c \approx 2\hbar\omega_D e^{-1/N_0 V_0} \tag{2.8}$$

and is related to the energy gap by:

$$\Delta(0) = 1.76\, k_B T_c \tag{2.9}$$

Although the BCS theory successfully explains the features of conventional superconductors, it predicts a maximum T_c of approximately 40 K even in the strong coupling limit [45], a limitation that fails to account for the significantly higher critical temperatures observed in HTS. In addition, most unconventional superconductors arise from a non-metallic ground state and have a very complicated normal state. BCS theory fails to account for either of these traits.

2.2 High T_C Superconductor and $YBa_2Cu_3O_{7-\delta}$

One of the reasons HTS are considered unconventional (among many), is due to their critical temperatures surpassing the limits predicted by BCS. Despite many decades of research, a complete description of the mechanisms underlying their behavior remains a mystery. This section provides a concise overview of HTS materials, before focusing on the specific cuprate used in this work: $YBa_2Cu_3O_{7-\delta}$ (YBCO).

2.2.1 Brief History and Roadmap of HTS

In 1986, Bednorz and Müller discovered the first HTS material, which belonged to the cuprate family, $La_{2-x}Ba_xCuO_4$ (LBCO), with a critical temperature of 35 K [5]. This cuprate exceeded expectations, not only by breaking the BCS's theoretical T_c limit, but also by demonstrating superconductivity in a material type, whose ground state was insulating and not metallic. All conventional, low-T_c superconductors explained by BCS, originated from a metallic ground state. Soon after, another cuprate, $YBa_2Cu_3O_{7-\delta}$ (YBCO), was discovered with a T_c near 92 K [46]. This was a bigger milestone, as it was the first material to show superconductivity above the boiling point of liquid nitrogen (77 K). Such a discovery made cryogenic applications more accessible and cost-effective than with liquid helium, which was absolutely necessary for low-T_c.

After this breakthrough, more cuprates with even higher T_c values were identified under ambient pressure, reaching up to 135 K in mercury-based compounds by 1999 [10]. Unconventional superconductors don't belong only to the cuprate family. Soon after, new HTS families emerged in the 2000s. **Figure 2.1** highlights key milestones in the development of HTS materials [8]. Among these, YBCO remains as one of the most extensively studied, alongside $Bi_2Sr_2CaCu_2O_{8+x}$ (Bi2212) and $La_{2-x}Sr_xCuO_4$ (LSCO), due to its high critical temperature and practical relevance.

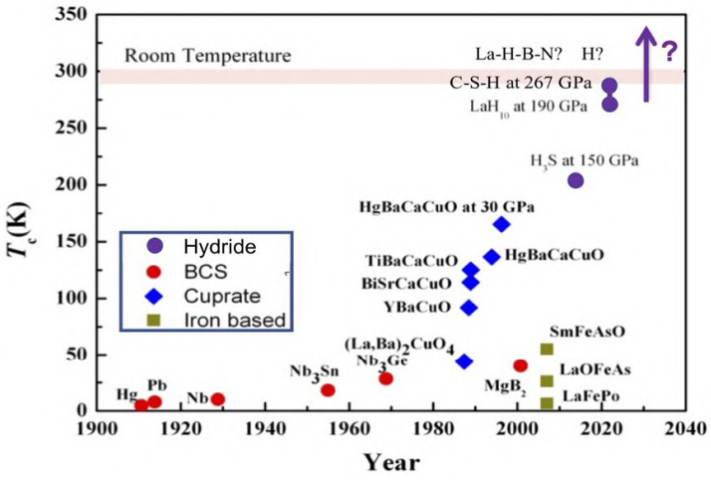

Figure 2.1: Roadmap of High-Temperature Superconductivity [4].

2.2.2 Structure and Properties of $YBa_2Cu3O7 - \delta$

Cuprate superconductors are known for their layered, quasi-two-dimensional crystal structures. These materials consist of conducting CuO_2 planes, that are separated by insulating blocks. These insulating blocks act as charge reservoirs and provide structural stability. The CuO_2 planes are the primary sites of superconductivity, while the weak interlayer coupling between these planes (due to the presence of the insulating layers) leads to anisotropy between the in-plane (ab) and out-of-plane (c-axis) transport. In particular, YBCO has a complex unit cell composed of three perovskite layers, with Yttrium sandwiched between two Barium, containing layers, as shown in **Figure 2.2** [30].

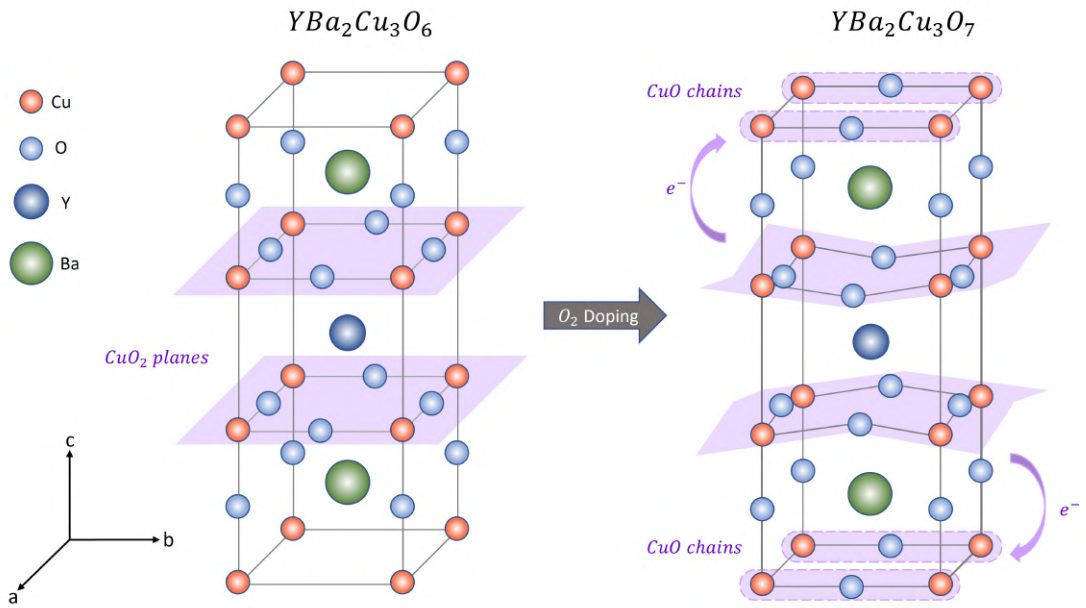

Figure 2.2: Illustration of YBCO crystal structure and the hole-doping mechanism (adapted from [34]). The parent compound ($YBa_2Cu_3O_6$) has a tetragonal structure with lattice parameters a=b=3.86 Å,c=11.82 Å. The formation of CuO chains from oxygen (hole) doping distorts the crystal structure, resulting in orthorhombic with lattice parameters a = 3.82 Å, b = 3.89Å, c = 11.68Å for the fully developed CuO chains.

The undoped parent compound (most stable form of YBCO), $YBa_2Cu_3O_6$, exhibits a tetragonal structure with Cu only chains. Empty sites are available in the chains. As oxygen is added to these chains, it forms quasi-one-dimensional CuO chains along the b-axis, modifying the crystal symmetry to orthorhombic with $b > a$ [47]. These chains introduce anisotropy and lead to subtle distortions (puckering) in the CuO_2 planes. The c-axis lattice parameter becomes doping-dependent, as observed in both thin films and single-crystals [48–50]. In fact, its length is usually used to indicate the doping level of YBCO. The superconducting parameters such as coherence length and London penetration depth also reflect this anisotropy. **Table 2.1** compares the superconducting parameters of YBCO with those of conventional superconductors [51–53].

Material	SC Type	T_C (K)	Δ (meV)	$\lambda^{a,b,c}$ (nm)	ξ^{ab}, ξ^{c} (nm)	H_{c2}^{ab} ; H_{c2}^{c} (T)
Al	I	1.175	0.18	50	1600	0.01
Pb	I	7.19	1.32	39	83	0.08
In	I	3.405	0.52	64	440	0.028
Nb	II	9.25	1.5	44	40	~3
$YBa_2Cu_3O_{6.9}$	II	93	20–25	150–300; $\lambda^a/1.2$; ~1000	1–3; ~0.24	250 ; 120

Table 2.1: Comparison of superconducting properties for optimally doped YBCO and other conventional superconductors.

2.2.3 Order Parameter and Fermi Surface in Cuprates

As mentioned above, conventional superconductors usually have an isotropic s-wave order parameter (**Figure 2.3(a)**), while in cuprates, the symmetry is predominantly $d_{x^2-y^2}$ (d-wave) (**Figure 2.3(b)**) [54]. In this form, the superconducting gap is wave vector (momentum) dependent: $\Delta_d(k) = \Delta_0(\cos k_x - \cos k_y)$, resulting in nodal points (zero gap even when the temperature is 0K) along the diagonal directions and a maximum gap at the anti-nodal points. The Fermi surface in hole-doped cuprates like YBCO typically resembles a large cylinder centered at (π, π) in the Brillouin zone, as illustrated in **Figures 2.3(c)** and **(d)**. The anti-nodal regions, where the superconducting gap is strongest, correspond to $(0, \pm\pi)$ and $(\pm\pi, 0)$. The nodal directions lie along $(\pm\pi/2, \pm\pi/2)$. It is worth noting, that this is a simplified picture, as the actual Fermi surface is more complex due to bilayer splitting and CuO chain contributions [55].

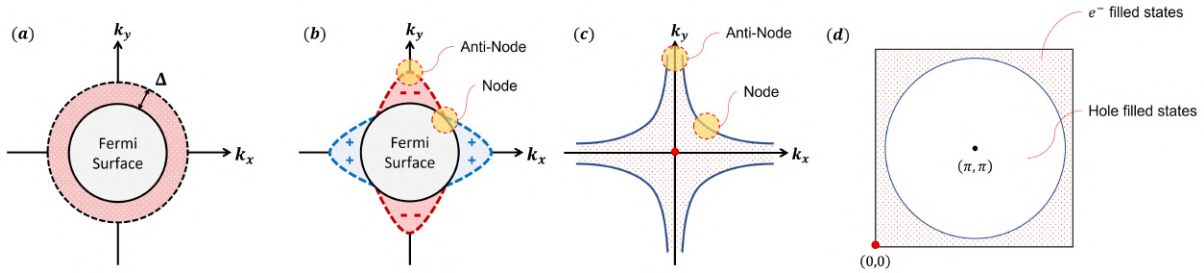

Figure 2.3: Illustration of (a) s-wave order parameter, (b) d-wave order parameter. Both (c) and (d) are the sketch of the Fermi surface where (c) is centered at (0,0) and (d) is centered at the (π, π) point of the first Brillouin zone (adapted from [1])

2.2.4 Phase Diagram of YBCO

The physical properties of YBCO can be modulated through oxygen doping (p) within the CuO chains. Based on the doping levels and its inherent complexity, YBCO has a rich and intricate phase diagram, as depicted in **Figure 2.4**. Due to many different phases acting simultaneously around the same doping region, there is a lot of added difficulty to understanding this material. The superconducting region spans a hole concentration of $0.05 < p < 0.23$, with a maximum critical temperature ($T_c \sim 93$ K) occurring at optimal doping near $p = 0.16$. Unlike, the conventional parabolic behavior associated with superconducting domes, YBCO displays an anomalous suppression around $p \sim 0.125$. This is often referred to as the "1/8 anomaly." Such a dip in T_c is attributed to a competing charge order (charge density wave - CDW) that disrupts superconductivity [56]. In addition, other orders like Charge Density Fluctuations (CDF) have been observed in

YBCO, though they still have not been properly mapped as to where they lie in the phase diagram. Pair Density Wave (PDW) order has also been hypothesized to exist in the YBCO phase diagram, as it has been confirmed in other cuprate families [57, 58]. This is a special ordering phenomena, which modulates the superconducting order parameter, such that its spatial average vanishes. Many phenomena have been theoretically related to PDW, although its existence in YBCO has not been confirmed yet. In the following sections, we will discuss the currently known phase diagram of YBCO.

The phase diagram of YBCO is commonly divided into three doping regimes: underdoped, optimally doped, and overdoped.

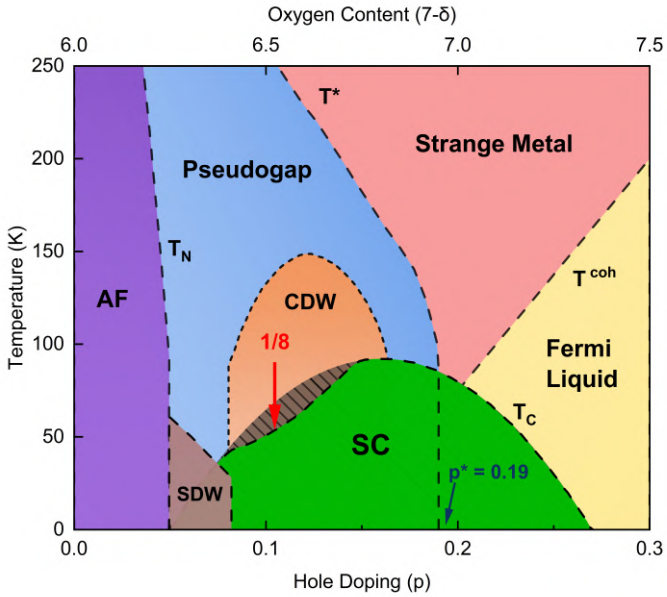

Figure 2.4: Phase diagram of YBCO as a function of hole doping (p) and oxygen content ($7-\delta$) per unit cell (adapted from [34]). YBCO is characterized by multiple intertwined orders, depending on the level of doping as shown in the diagram. T_N, T^*, and T_{coh} are Néel, pseudogap, and coherent temperatures, respectively.

Underdoped Region ($p < 0.16$)

The underdoped regime represents the most intricate part of YBCO's phase diagram. It is characterized by the coexistence of spin and charge orders. Below we outline a summary of the normal-state behavior:

- **Mott Insulating Phase:** In the absence of doping, YBCO behaves as a Mott insulator, with each Cu site hosting one localized hole. Due to the strong on-site Coulomb repulsion, the system becomes insulating instead of metallic, contrary to predictions from simple band theory [59]. This regime exhibits antiferromagnetic (AF) ordering, which is quite persistent in temperature. However, the introduction of holes around $p \sim 0.05$ destabilizes the AF phase, allowing charge carriers to delocalize.
- **Spin Order:** Following the suppression of the AF state, a Spin Density Wave (SDW) emerges. It is a periodic modulation in spin density observed in the doping window $0.05 < p < 0.08$ [60]. In contrast to other cuprates such as LSCO, where spin and charge orders overlap significantly, YBCO exhibits minimal overlap between

these two phenomena [61–63]. It may be possible for residual, weak SDW signatures to exist above $p \approx 0.08$.

- **Pseudogap Phase:** One of the most important phases of the underdoped regime is the pseudogap. It is a partial suppression of the electronic density of states along the anti-nodal directions of the Fermi surface [64, 65]. This leads to a transformation from a full hole-like cylinder Fermi Surface into disconnected segments known as Fermi arcs (**Figure 2.5(a)**). Above the pseudogap opening temperature, the full hole-like cylindrical Fermi Surface is observed (**Figure 2.3(c)**) [2, 21–23]. Two quantities define the pseudogap: the critical doping level p^* (where the pseudogap abruptly ends), and the onset temperature T^*. T^* is typically identified as the temperature where deviations from linearity in the resistivity curve $\rho(T)$ [66] start. The relationship between the pseudogap and superconductivity remains an open question to this day. Some studies suggest competition between them, as the emergence of d-wave superconductivity around T_c appears to coincide with the disappearance of Fermi arcs near the nodal regions [24]. Others propose a precursor relationship, in which the pseudogap contains at pre-formed Cooper pairs without phase coherence or spin/pairing fluctuations [25, 26, 67].

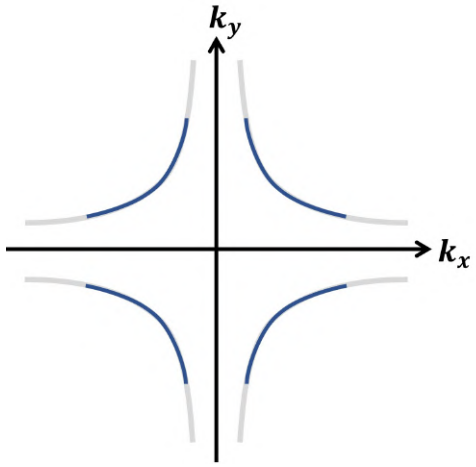

Figure 2.5: Simplified illustration of the Fermi surface in the pseudogap phase (adapted from [1]). The grey contour represents the full hole-like cylindrical Fermi surface; the blue arcs show the remaining coherent segments (Fermi arcs).

- **Charge Order:** Charge Density Wave (CDW) order occupies a broad region in the underdoped phase, specifically the doping range $0.08 < p < 0.16$. CDW in cuprates involves incommensurate modulations of the charge density within the CuO_2 planes. This order is short-ranged, quasi-two-dimensional, and exhibits biaxial symmetry with in-plane correlation lengths going up to ~ 75 Å (approximately 20 lattice constants) [68, 69]. X-ray scattering experiments reveal anisotropic charge modulations, that are particularly pronounced near $p \sim 1/8$ (this is where CDW is the strongest) [70]. Despite ongoing debates about its microscopic origin, there is strong experimental evidence for CDW's competition with superconductivity [68, 69]. For instance, CDW intensity increases with decreasing temperature down to T_c, and then weakens below it. This order is also enhanced by magnetic fields that are known to suppress superconductivity [71].

Optimally Doped Region ($p = 0.16$)

YBCO reaches its maximum critical temperature in this phase. The strange metal phase domiantes the normal state. This phase is associated with unconventional transport properties, most notably, its linear temperature dependence in resistivity $\rho(T)$ over an exceptionally wide range [72, 73]. Such behavior contrasts with the predictions of Fermi-liquid theory, where $\rho(T)$ should obey a T^2 law from electron-electron scattering [74, 75]. This deviation signals a breakdown of the quasiparticle picture.

Evidence from Angle-Resolved-Photo-Electron-Spectroscopy (ARPES) and shot-noise measurements [76, 77] indicate that the scattering rate reaches the so-called Planckian limit, $\tau_p \sim \hbar/k_B T$ [78]. This implies ultrafast decoherence and renders the conventional quasiparticle framework ineffective. Remarkably, these features are universal across many cuprate families [79].

The microscopic origin of strange metal phase remains the subject of intense debate to this date. One widely discussed hypothesis ties it to a quantum critical point (QCP) located at $T = 0$ and $p = p^*$, where quantum fluctuations dominate over thermal ones [80, 81]. Supporting this view, recent experiments have uncovered persistent charge density fluctuations (CDF), shorter in range than the CDW order but extending up to room temperature, which could be fingerprints of the strange metal regime [82–84].

Regardless of interpretation, the strange metal phase at optimal doping remains a central piece of the HTS puzzle.

Overdoped Region ($p > 0.16$)

The overdoped regime is considered simpler, as superconductivity persists only up to $p \approx 0.25$, beyond which the system returns to a Fermi-liquid state. The transition to coherent quasiparticle behavior is marked by the coherence temperature (T_{coh}), signaling the restoration of a conventional metallic phase. However, recent investigations have revealed several non-trivial features even in this region.

For instance, anisotropic quasiparticle excitations have been observed [85]. In addition, evidence has been reported for residual charge ordering beyond optimal doping [86]. These findings suggest a more nuanced picture of the overdoped phase, challenging the assumption of a complete return to Fermi-liquid behavior. Unfortunately, systematic studies for overdoped YBCO are limited by experimental constraints. Conventional oxygen doping techniques can only reach up to $p \sim 0.19$ [34]. To explore higher doping levels, more creative approaches such as chemical substitution must be employed [87, 88].

2.3 Electronic Nematicity in Cuprates

The nematic phase, often described as an electronic liquid crystal state, occurs when the electronic structure preserves translational symmetry, but spontaneously breaks the four-fold (C_4) rotational symmetry [89]. Just like in classical liquid crystals [90], the ground state lies between that of a "liquid" (dominated by large quantum fluctuations) and a "solid" (with minimal fluctuations). The concept of nematicity in cuprates emerged following the discovery of stripe orders, dynamic modulations of charge and spin forming stripe patterns in lanthanum-based cuprates [91]. Beyond cuprates, nematic signatures have also been identified in other unconventional superconductors, including iron-based systems [92], heavy-fermion compounds [93], and even topological superconductors [94].

In cuprates, detecting nematic order is challenging due to its subtle characteristics: short correlation lengths and its small associated energy scale [95, 96]. Furthermore, because nematicity is characterized by a wavevector $Q = 0$, spectroscopic detection is hindered by dominant elastic scattering signals [97]. As a result, evidence for nematicity in these materials has often been indirect, emerging from anomalies in resistivity $\rho(T)$, the Nernst coefficient, and magnetic susceptibility [98–100]. Strain appears to be an important factor that influences nematicity. This nematic transformation can also be induced by the presence of superpotential.

One way to impose a superpotential on a thin film, is by modifying the substrate morpholgy. This is done through surface treatments, by thermally annealing a MgO (110) substrate at $T = 770^0C$ for 5 hours. This annealing process creates a surface reconstruction of the MgO into nanofacets that are aligned along the b-axis of YBCO. These nanofacets lead to the formation of untwinned YBCO films [33]. This effect combined with shrinking of film's thickness from 50nm to 10nm leads to some interesting effects, associated with a modification of the YBCO's ground state [29].

Our group reported an unusual anisotropy in the $\rho(T)$ of underdoped, ultrathin ($10nm$) YBCO films grown on MgO (110) substrates and observed the nematic transformation of the Fermi Surface [2, 32, 101].

One promising approach to indirectly, probe nematicity is through c-axis transport. Suppression of anti-nodal states (expected if nematic order is present), would be directly reflected in c-axis electrical measurements, as they are the contributing states. This might manifest as a reduction of resistance in the upturn (metallic-to-semiconducting transition) associated with underdoped, c-axis transport [28].

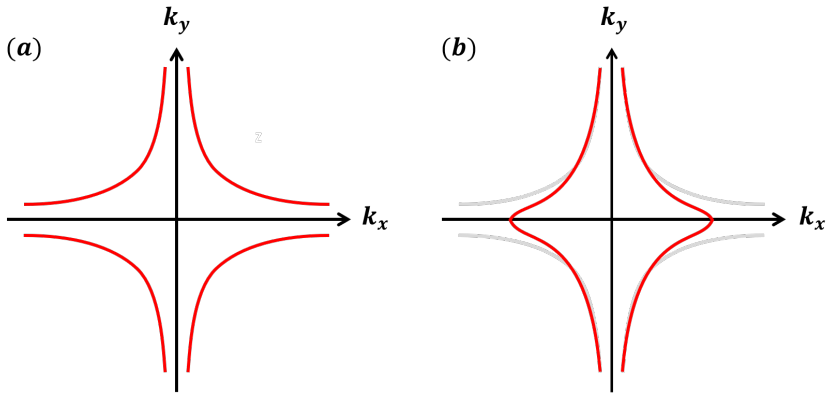

Figure 2.6: (a) Typical hole-like cylindrical Fermi surface. (b) Nematic distortion of the Fermi surface (adapted from [2]).

2.4 Andreev Reflections and Zero Energy Andreev Bound States

When a quasiparticle originating from a normal metal (N) reaches the interface of a superconductor (SC), its transport properties are affected by the presence of the superconducting gap Δ. If the incoming electron has an energy below that of the superconducting gap, it cannot enter the superconductor as a single particle, due to the absence of available states within that energy range. However, a unique process known as Andreev reflection can occur [102].

Imagine a quasi-electron approaching a superconductor from a normal metal, with an energy $E < \Delta$ (see **Figure 2.7**). The incident quasi-electron forms a Cooper pair by combining with another quasi-electron of opposite spin and momentum from the Fermi sea of the normal metal. This pair can now enter the superconductor. Simultaneously, a quasi-hole is reflected back into the normal region with opposite spin and momentum of the incident quasi-electron. This mechanism conserves both charge and momentum and enables subgap transport across the SN interface.

Andreev reflection is a phase-coherent phenomenon that couples electron and hole states. It is especially significant in the study of low-energy quasiparticle dynamics in hybrid superconducting systems and for studying transport across interfaces. Its characteristics, such as amplitude and phase, are highly sensitive to the interface quality, the symmetry of the superconducting order parameter and the geometry of the junction.

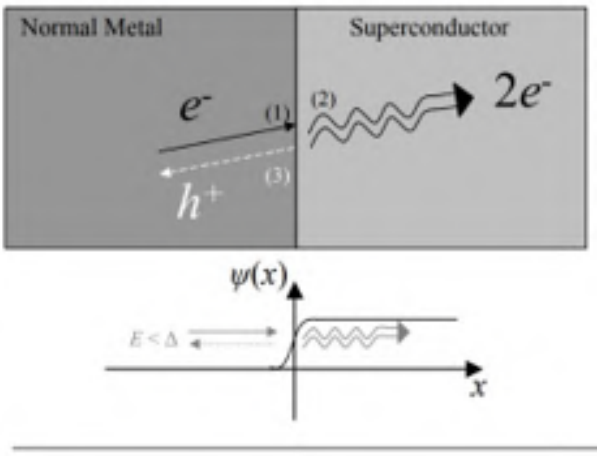

Figure 2.7: Andreev Reflection (adapted from [3])

A particularly rich manifestation of Andreev physics occurs in unconventional superconductors such as HTS cuprates, where the superconducting gap exhibits d-wave symmetry. In such materials, the order parameter Δ changes sign depending on the momentum direction. When quasiparticles reflect from a surface or interface with this sign-changing gap structure, interference effects can arise [102], such as zero energy Andreev Bound States (ABS). This process leads to the appearance of a Zero-Bias Conductance Peak (ZBCP) in tunneling spectroscopy (see **Figure 2.8**) [3, 102].

Initially, a quasi-electron in the normal metal with $E < \Delta$ specularly reflects at the interface. Then it experiences a sign change due to the d-wave superconducting order

parameter. It undergoes Andreev reflection, propagates into the superconductor, and causes a quasi-hole to be reflected back into the normal region.

This quasi-hole, too, specularly reflects at the interface, again encountering a sign change in Δ, and undergoes another Andreev reflection. As a result, a Cooper pair is transferred into the superconductor (which traces the path of the quasi-electron) and a new quasi-electron is reflected back into the normal metal. The entire cycle repeats periodically, creating a standing wave pattern of electron–hole states. This standing wave is confined near the interface.

For such resonant and periodic Andreev reflections to occur, the orientation of the interface must be special. The quasiparticle trajectory must encounter alternating regions of positive and negative Δ. The YBCO orientation that fulfills this criteria is the (110) direction. In this configuration, the initial quasi-electron sees $+\Delta$, and its reflected quasi-hole experiences $-\Delta$, leading to a π phase shift per cycle.

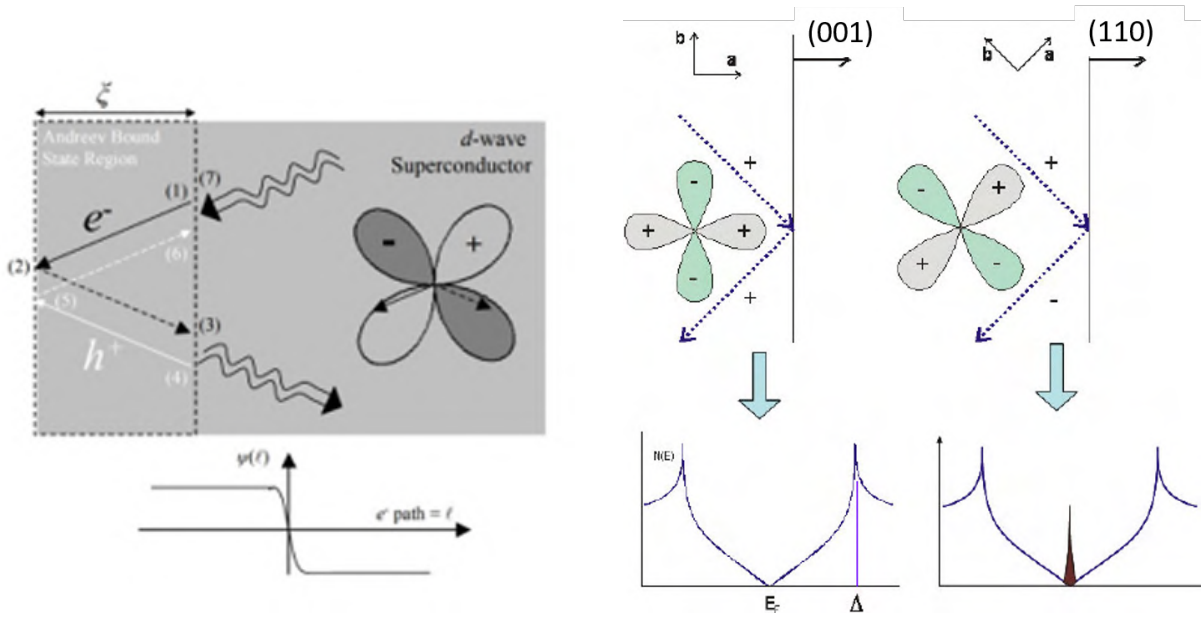

(a) Andreev Bound State formation (adapted from [3])

(b) Andreev Bound State and Zero Bias Conductance Peak (adapted from [103])

Figure 2.8: Andreev Bound State formation and Zero Bias Conduction Peak

These zero energy solutions are called zero energy ABS. They manifest as sharp peaks in the local density of states, which are detected via tunneling spectroscopy as a zero-bias conductance peak. Their presence serves as a strong fingerprint of unconventional superconductivity and indicates that the interface is aligned along a nodal direction, specifically, the (110) axis in the case of YBCO.

3

Deposition and Characterization of YBCO thin films

The first and most critical step to develop our c-axis platform and perform our measurements, is the deposition of high-quality YBCO thin films.

Thin films are the first and most essential building block for device fabrication. For example, they are the starting point in Superconducting QUantum Interference Devices (SQUIDs) [104, 105], and in single-photon detectors [106, 107]. In this thesis, we use them as the first block needed to fabricate the mesa devices, with which we will examine the c-axis transport of twinned YBCO films grown on $SrTiO_3$ (STO) substrates.

This chapter describes the thin film fabrication process, as well as the the deposition parameters used. It also introduces relevant structural considerations such as strain and twinning, which influence the physical properties of the YBCO films.

3.1 Thin Film Fabrication – Pulsed Laser Deposition (PLD)

The deposition of high-quality YBCO thin films is a complicated process that demands careful attention to multiple factors. YBCO is structurally complex and highly sensitive to stoichiometric variations, particularly with respect to oxygen content. The amount of oxygen has a direct influence on the hole doping level and thus the superconducting properties. To achieve reliable nanoscale transport measurements, we require films with exceptional homogeneity and surface smoothness.

The preferred approach to obtain high quality YBCO films is expitaxial growth. It can be realized via several techniques, like pulsed laser deposition (PLD), molecular beam epitaxy (MBE), and dc/rf magnetron sputtering. In this work, the PLD method is used and it is widely recognized for its capability to yield stoichiometric films, as well as for the high degree of control it provides over growth conditions. Nonetheless, obtaining good films requires careful optimization of several parameters including laser fluence, substrate deposition temperature, oxygen pressure, and post-annealing conditions.

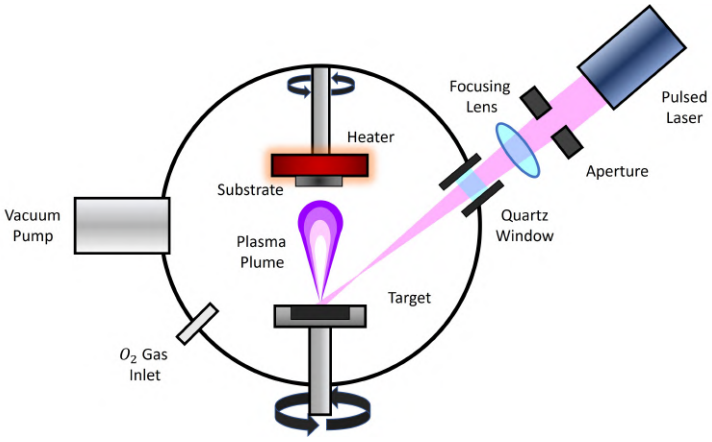

Figure 3.1: Illustration of the PLD system used to deposit YBCO thin films (adapted from [1])

The working principle of PLD is based on the ablation of a bulk YBCO target by a laser. A high-energy laser pulse, strikes the target's surface, creating a vaporized plasma plume with ions. This plasma plume propagates towards the heated substrate, where the atoms condense and grow into a thin film. The composition of the deposited film is determined by the plasma plume's dynamics, which depend on the laser fluence (E), pulse repetition rate (f), and the oxygen pressure during deposition (P_{dep}). Additionally, the deposition temperature (T_{dep}) and target–substrate distance (d) influence atom adsorption and surface diffusion. Thereby they are important parameters as they affect film nucleation and growth. These parameters are all variable and highly depend on the chosen substrate where the film will be grown (so they must be tuned for each substrate).

The number of pulses (n) determines the film thickness. After deposition, the film is deficient in oxygen due to the high deposition temperature. This results in the tetragonal parent phase $YBa_2Cu_3O_6$. To induce superconductivity, oxygen is reintroduced in the film during cooldown through a post-annealing process. The final doping level is determined by the post-annealing oxygen pressure (P_{ann}). In this thesis, the films are underdoped with a hole concentration of $p \sim 0.11$, obtained by annealing at $P_{ann} = 0.001$ mbar (corresponding to flow 5 sccm in the system).

T_{dep} (°C)	P_{dep} (mbar)	E (mJ)	f (Hz)	d (mm)	P_{ann} (mbar)
750	0.7	57–59	4	55	0.001

Table 3.1: Deposition conditions for underdoped YBCO thin films.

These deposition parameters have been chosen to get the right compromise between electrical transport properties and surface smoothness (as it is impossible to obtain both of them at the same time). For example, lowering the deposition temperature (T_{dep}) is known to generally improve the surface smoothness but broadens the superconducting transition (worse electrical property).

3.2 Substrate, Strain, and Twinning

The choice of substrate plays a critical during epitaxial thin film growth. It governs both the crystallographic orientation and the type of strain applied on the film. In order

to closely replicate the properties of bulk, single-crystal YBCO, the substrate must exhibit both structural and lattice parameter compatibility. Therefore, the lattice mismatch is a key parameter, defined as:

$$\delta^m = \frac{a_s - a_{film}}{a_s} \tag{3.1}$$

where a_s and a_{film} are the in-plane lattice parameters of the substrate and the thin film, respectively.

An excessive lattice mismatch induces strain, which can lead to film distortion, defect formation, or even strain relaxation. To have high-quality epitaxial growth, the typical acceptable lattice mismatch should be below 1%. However, due to the limited thickness (50 nm) of the films in this study, a slightly higher mismatch can be tolerated.

Oxide substrates such as $SrTiO_3$ (STO), $LaAlO_3$ (LAO), LSAT, and MgO are preferred for YBCO film growth due to their similar lattice constants and compatible thermal expansion properties. For instance, the mismatch between YBCO and STO(001) is approximately 2%, whereas YBCO/MgO(001) yields a much larger mismatch of around 9% [33]. The in-plane lattice parameters of these substrates and YBCO are summarized in Table 3.2. Note that the orientation of the substrate's surface also palys a role on the mismatch.

Material & Orientation	In-Plane Lattice Parameters (Å)
YBCO (Optimally Doped)	$a = 3.82$, $b = 3.89$
STO(001)	$a = b = 3.91$
LAO(001)	$a \approx b = 3.79$
MgO(001)	$a = b = 4.21$
MgO(110)	$a = 4.21$, $b = 5.96$

Table 3.2: In-plane lattice parameters of YBCO and common oxide substrates. Values adapted from [105] and vendor sources.

YBCO's crystal structure changes to orthorhombic upon oxygenation, due to the formation of CuO chains. This leads to anisotropy in the a and b lattice parameters. In theory, this would also result in anisotropic electronic transport. However, twinning occurs during film growth and masks this anisotropy.

Twinning is a phenomenon that refers to the formation of multiple crystallographic domains within the film, each rotated with respect to the others. This occurs when YBCO is grown on substrates that have a square in-plane symmetry, like STO(001). Hence, the $a-axes$ and $b-axes$ of the YBCO film are randomly exchanged across the twin boundaries. This exchange, effectively averages out any intrinsic anisotropy, which would arise from the CuO chains. Due to this averaging effect, we do not observe the anisotropy in transport measurements [108]. However, there are techniques (such as annealing on MgO (110)) [33] to obtain untwinned YBCO films, where the anisotropy between a and b can be observed in transport as well.

For this thesis, YBCO films were grown on (001) oriented STO substrates. This is a widely used substrate due to its close lattice match ($a_{STO} = 3.905$ Å). Given STO's cubic symmetry, the resulting YBCO films are fully twinned and experience an in-plane tensile strain, as STO's lattice constant is slightly larger than that of YBCO.

3.2.1 Transport Characterization

The electrical transport properties of the YBCO thin films were examined to assess their behavior. This characterization was carried out through resistance versus temperature ($R(T)$) measurements using the Van der Pauw technique in the Physical Property Measurement System (PPMS).

One quick and simple method to determine whether a sample lies on the underdoped or overdoped side of the phase diagram, is by analyzing the shape of the $R(T)$ curve. In slightly overdoped samples (**Figure 3.2(a)**), the linear dependence of $R(T)$ bend upwards just before the onset of superconductivity [82]. In contrast, for underdoped samples, the $R(T)$ curve bends downward near the transition, as shown in **Figure 3.2(b)**. Although the origin of this downward turn is still debated, it is thought to result from the interplay between the pseudogap phase and other coexisting orders, such as CDW and superconducting fluctuations (paraconductivity) [20, 27, 109].

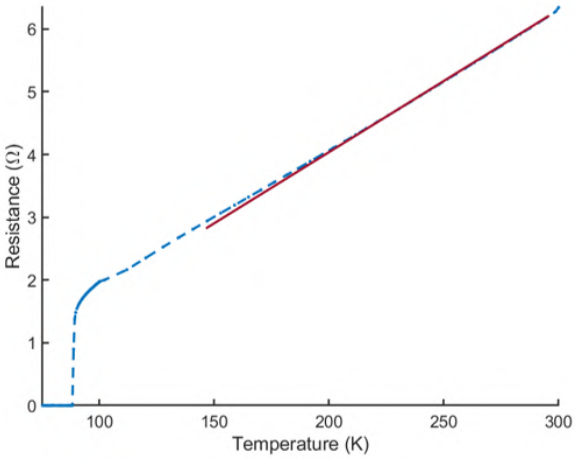

(a) Slightly overdoped YBCO thin film.

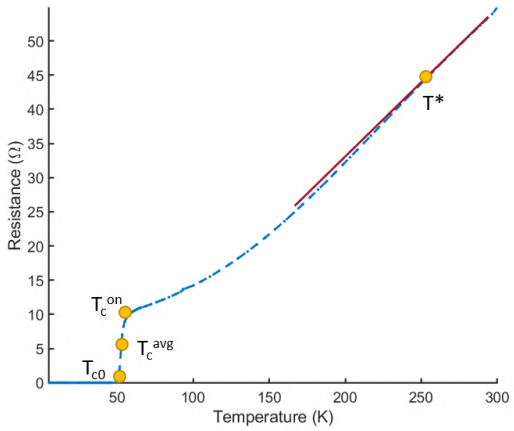

(b) Underdoped YBCO thin film and its characteristic temperatures.

Figure 3.2: Examples of $R(T)$ for (a) slightly overdoped and (b) underdoped YBCO thin films. Measurements were performed on samples grown on STO (001).

If we neglect the effects of twinning (or used untwinned films), the in-plane transport in YBCO is expected to be anisotropic due to the contribution of CuO chains. In particular, the resistance is lower along the direction parallel to the chains. However, in twinned YBCO films, where domains are randomly oriented along the a- and b-axes, the transport becomes isotropic as the CuO chains are distributed along both directions (there is an averaging effect between a and b).

The doping level and its homogeneity can be inferred from the characteristics of the superconducting transition. Two key parameters are typically used: the onset temperature (T_c^{on}) and the width of the transition (ΔT_c). T_c^{on} is defined as the temperature at which resistance drops to 90% of its normal state value, while ΔT_c is obtained from the full width at half maximum (FWHM) of the first derivative dR/dT. In general, a narrower transition indicates more uniformity and better superconducting properties (narrow transitions are preferred). Alternative definitions include the average transition temperature $\bar{T}_c$ (or referred to as T_c^{avg} as well), determined at the peak of $dR(T)/dT$ (or at the midpoint of the $R(T)$ transition), and the zero-resistance temperature T_{c0}.

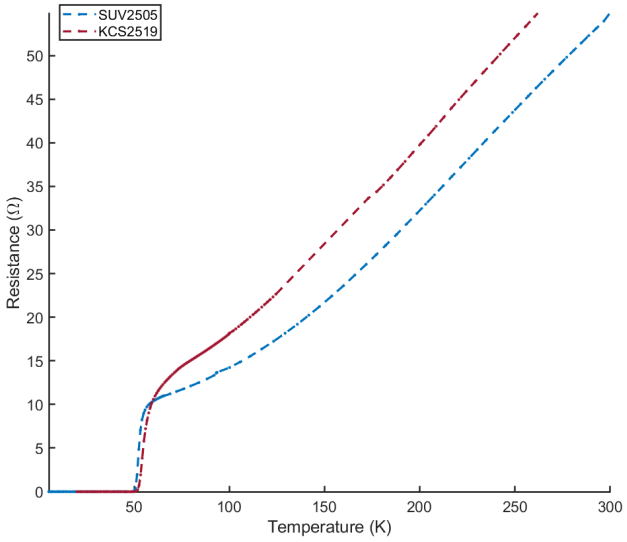

(a) $R(T)$ plots for the two thin films (SUV2505 and KCS2519) used in mesa device fabrication. These are the representative films.

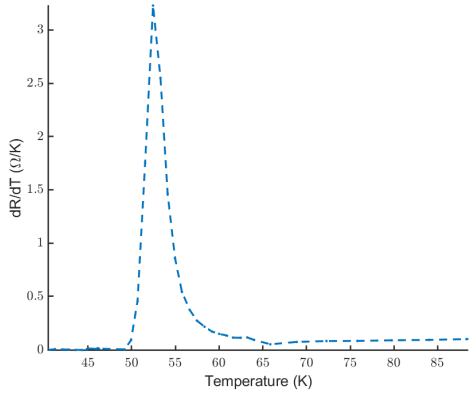

(b) dR/dT — SUV2505 of an underdoped film 50 nm thick

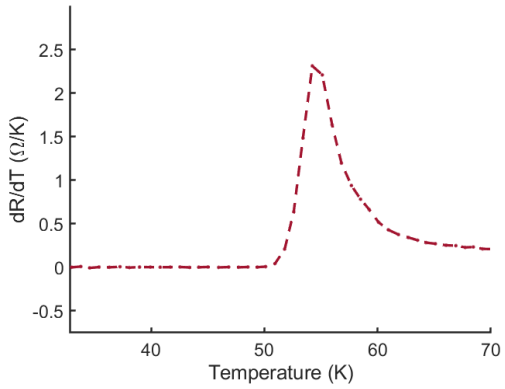

(c) dR/dT — KCS2519 of an underdoped film 50 nm thick

Figure 3.3: Representative $R(T)$ and dR/dT plots for two 50 nm underdoped YBCO thin films that were used for mesa device fabrication (SUV2505 and KCS2519).

The sample illustrated in blue in **Figure 3.3(a)** was later used to fabricate single-lithography mesas for c-axis transport measurements, while the sample in red was used to fabricate three-lithography mesas.

The transition width ΔT_c is approximately 2.5 K, which is comparable to values reported for high-quality single crystals [110]. The onset superconducting temperature for this sample was $T_c^{on} = 55.7$ K. Notably, non-uniform doping can also be inferred from the presence of multiple transitions within the same $R(T)$ curve. Achieving a sharp and single transition in 50 nm underdoped YBCO films required substantial optimization of the deposition parameters, as increased thickness and lower oxygen content tend to promote inhomogeneities.

The superconducting transition temperatures of both films suggest a doping level near $p \approx 0.11$.

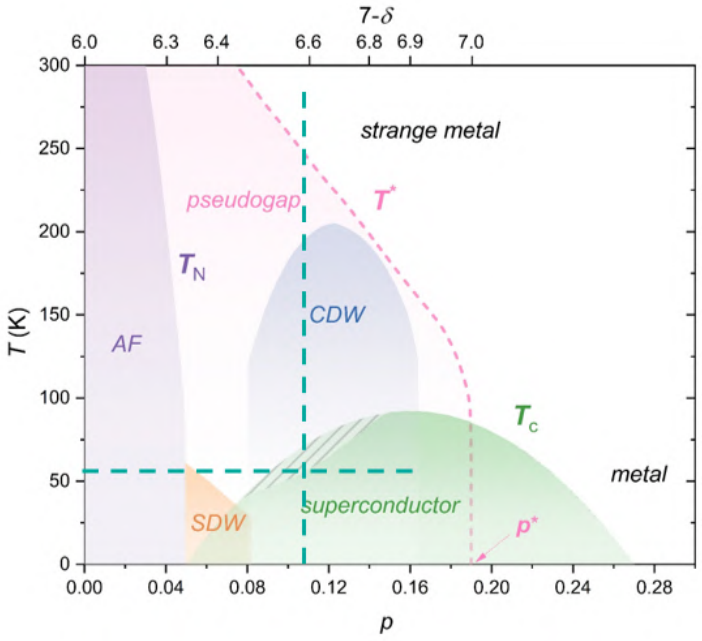

Figure 3.4: Estimated doping positions of the YBCO thin films in the superconducting phase diagram (adapted from [2])

Table 3.3: Superconducting transition parameters for SUV2505 and KCS2519 films

Sample	T_c^{on} (K)	$\bar{T}_c$ (K)	ΔT_c (K)	T_{c0} (K)
SUV2505	55.75	52.45	2.5	49.19
KCS2519	60.10	54.25	3.8	50.95

4

Fabrication of YBCO Mesas

In this thesis, mesa structures were fabricated to investigate the c-axis transport properties of YBCO thin films. One of the primary challenges in fabricating with YBCO lies in maintaining the intrinsic bulk properties of YBCO throughout the patterning steps. This difficulty arises from the compound's high sensitivity to structural defects, stoichiometry and environmental exposure, primarily due to its chemical instability (notably, oxygen can easily diffuse out and is reactive to water) and its short coherence length (ξ), which makes its superconducting properties particularly sensitive to damage. This chapter outlines the fabrication procedure, that was utilized during this thesis work and was specifically optimized to preserve the HTS characteristics of YBCO for both single-lithography and three-lithography mesa devices.

The nanofabrication techniques applied to YBCO have been systematically refined by our research group over the past decade [111–113], and have proven effective for multiple HTS materials [114]. In this work, we utilized electron-beam lithography (EBL) to pattern the devices, in conjunction with an amorphous carbon hard layer for definition of the mask and a cryogenic ion beam etching (IBE) process cooled by liquid nitrogen for etching of the patterns into YBCO. The carbon (C) mask was selected for its strong resistance to ion milling and its capability of being cleanly removed via oxygen plasma, while also offering excellent pattern fidelity and edge definition. However, the c-axis measurement configuration presented specific fabrication challenges. Oxygen mobility is reduced along the c-axis so the risk of de-doping YBCO is less. However, the ab-planes were always exposed during fabrication (oxygen-out diffusion risks), making the process highly sensitive to damage. Furthermore, the mesa geometry involved high aspect ratios, which introduced additional complexity. Several fabrication-related issues were successfully addressed during this work, in both the single-lithography and three-lithography processes.

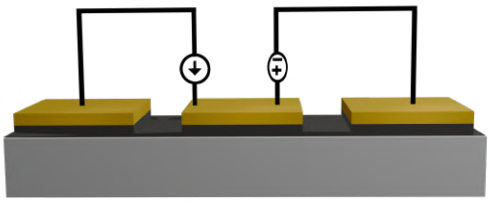

Figure 4.1: Schematic drawing of a mesa device, along with the respective current source and voltmeter

The mesa devices fabricated for c-axis transport measurements consisted of three YBCO pillars, each with a thickness of 50 nm and capped with a gold (Au) top contact,

as illustrated in **Figure 4.1**. A key requirement was to keep the slit (spacing) between adjacent pillars relatively small to ensure efficient electrical contact, although not too small, as empirical testing showed that a separation in the range of $1-2\,\mu$m was sufficient for our measurements. In order to have the required electrical conduction path, it was necessary to etch through the YBCO film while leaving behind a thin, conductive base layer approximately $10-20\,$nm thick. Due to the high sensitivity of YBCO to etching-induced damage, this step's parameters proved to be particularly critical for maintaining good device performance. This is also the reason why the slit's size was a limiting factor. Making the slit larger than 2μm would make the fabrication easier, but it would increase the risk that the remaining YBCO in the slit would turn completely insulating, disrupting our measurement scheme (see **Chapter 5** for more details). For narrower slits, this would be less of an issue, however it would make the nanofabrication process significantly harder, as we would have to reliably pattern a slit with a very large aspect ratio (very narrow, yet quite long). Nevertheless, $100nm$ slits were also achieved by our improved fabrication techniques.

4.1 Nanofabrication Mesa – One-Lithography Approach

Representative optical images of the finalized mesa devices are shown in **Figure 4.2**. Each YBCO pillar has an area of $100 \times 100\,\mu\text{m}^2$, and the spacing between two adjacent pillars (the slit) is $2\,\mu$m. During initial testing, various slit widths were explored, and slits as narrow as 100 nm were consistently achieved using our optimized nanofabrication protocol. However, a spacing of $2\,\mu$m was ultimately selected to ensure consistent YBCO thickness in the slits and around the mesas. Each pillar has a thickness of 50 nm and capped with a 70 nm Au layer. The YBCO remaining between the mesas and surrounding the structures was approximately 20 nm thick. This value was fine-tuned through IBE parameter optimization and confirmed via Atomic Force Microscopy (AFM) measurements.

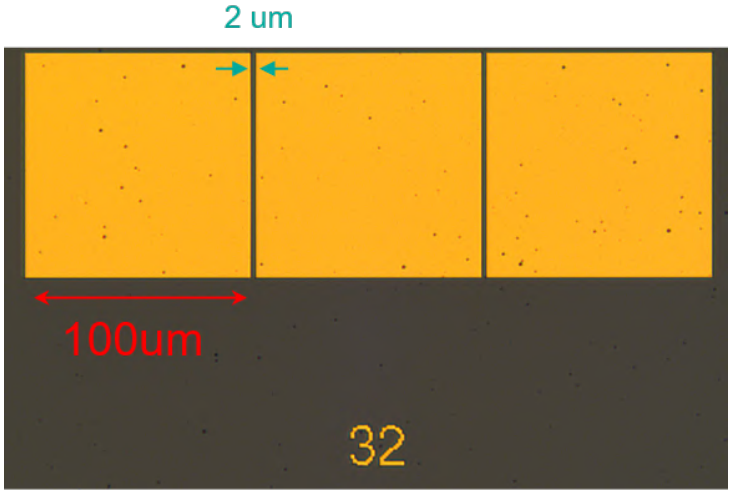

Figure 4.2: Optical image of the completed device. Each YBCO pillar has an area of $100 \times 100\ \mu\text{m}^2$ with $2\,\mu$m spacing between adjacent pillars.

The complete fabrication sequence is outlined below (illustrated in **Figure 4.3**):

1. **YBCO Deposition**: 50 nm of underdoped YBCO was deposited on a $5 \times 5\,\mathrm{mm}^2$ STO substrate via PLD. Underdoped films are more fragile and exhibit faster oxygen loss compared to optimally or overdoped counterparts. This necessitates extra caution throughout the fabrication process to preserve its properties.
2. **In-situ Au Sputtering**: Immediately following YBCO deposition, a 70 nm Au layer was sputtered in-situ (without vacuum breaking) at room temperature. This layer serves both as an electrical contact surface for wire bonding and as a protective chemical shunt, preventing oxygen out-diffusion from the underlying YBCO.
3. **Carbon Hard Mask Deposition**: An amorphous C film of approximately 100 nm thickness was deposited via PLD at ~ 75 mJ. This deposition energy ensured strong adhesion and sufficient hardness for subsequent ion milling steps.
4. **Spin Coating of Resist Layers**: Two layers of positive-tone resist were spin-coated atop the carbon mask for EBL patterning. Each layer was spun at 6000 rpm with an acceleration of 1000 rpm/s for 90 s, followed by baking at 96°C for 5 minutes on a hotplate. While this temperature is on the lower end of the resist's specification, it was chosen to reduce oxygen loss from YBCO. The bottom layer was MMA 8.5 EL4 (for adhesion), and the top layer was ARP 13 1:1 6200 (for better pattern definition). The reason we use two different resists is that they have slightly different doses in exposure. Specifically, the bottom layer will develop an undercut with respect to the top layer, which makes the lift-off of the metal much easier and precise.
5. **Electron-Beam Lithography (EBL)**: The mesa pattern was defined using EBL with a 100 kV beam, 1 nA current, and aperture 300. Development was performed in 96% o-xylene for 35 s to remove the ARP layer, followed by a 10 s IPA rinse (which stops the development). The MMA layer was then removed using MIBK 1:3 for 33 s, followed by another 10 s IPA rinse.
6. **Chromium Deposition**: A 10 nm Cr layer was deposited via e-beam evaporation (rate: 0.2 Å/s), serving as the metal mask, to which the pattern will be transferred to, and also protect the carbon underneath in the following step. The sample was then immersed in hot Remover 1165 (75°C, 20 minutes) to facilitate lift-off.
7. **Lift-Off**: Unwanted Cr was removed using sonication at 75% power: 1 min in Remover 1165 followed by 1 min in IPA. Successful lift-off was confirmed via SEM and optical microscopy.
8. **Oxygen Plasma Etching (RIE)**: Exposed areas of the carbon mask were etched with RIE at 50 W under 100 mTorr for 20 minutes. The Cr-covered regions remained protected, and the underlying YBCO was shielded by the full Au layer, protecting it from damage.
9. **Ion Beam Etching (IBE)**: Etching of exposed Au and YBCO was performed using Ar^+ ion beam milling under cryogenic conditions (liquid nitrogen cooling) to reduce heat-induced oxygen loss in YBCO. The parameters were optimized to retain a 20 nm YBCO base layer in the slits and between mesas. SIMS (Secondary Ion Mass Spectrometry) was used for in-situ depth control and compositional analysis.
10. **Carbon Mask Removal**: The remaining carbon layer was removed using a two-step RIE process—50 W for 3 min followed by 15 W for 1 h at 100 mTorr. Gentle RIE conditions were used to minimize damage to the exposed YBCO, as aggressive oxygen plasma can induce oxygen vacancies and reduce conductivity.

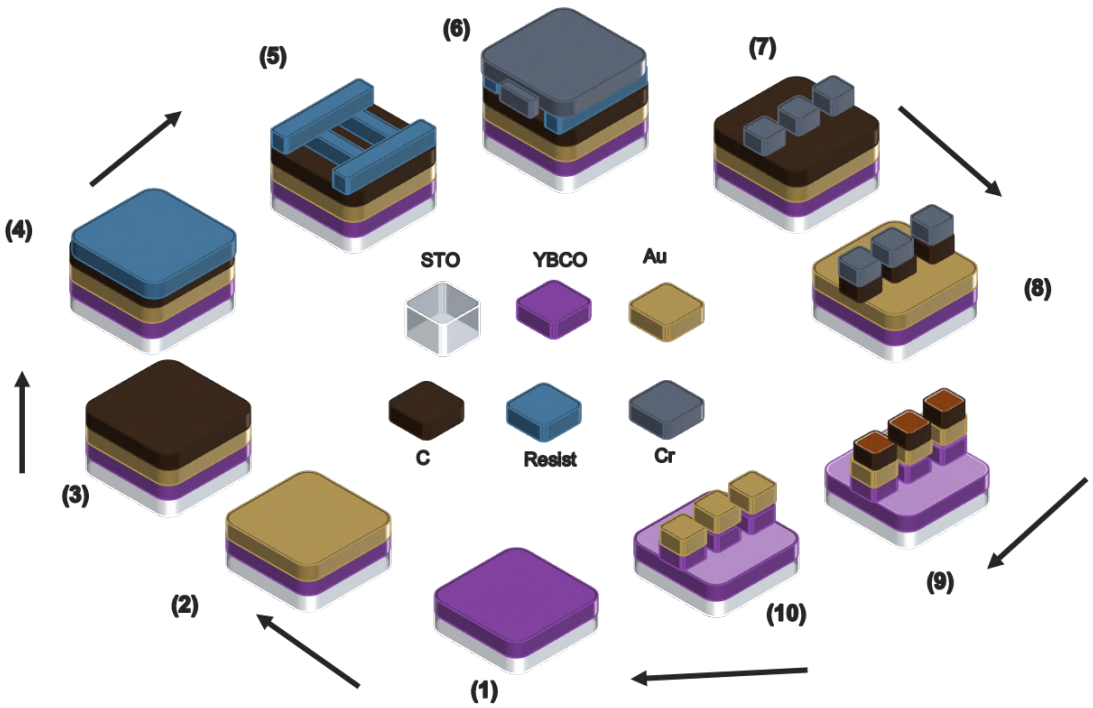

Figure 4.3: Step-by-step nanofabrication workflow for YBCO mesa devices

Several challenges arose during the definition of the mesa structures. Specifically, the large aspect ratio of the slits (100 μm long and only 2 μm wide) created complications in the lift-off process, resulting in rough sidewalls or, in some cases, electrical shorts (due to Cr failing to lift off) between adjacent pillars (see **Figure 4.4**). Although 2 μm slits posed no major issues, narrowing the slit to 100 nm significantly exacerbated these defects. To address this, we refined the fabrication process based on techniques outlined in [115]:

1. **Optimized MIBK Development Time**: Reduced from 35 s to 33 s to improve the resist profile's quality.

2. **Lowered Chromium Evaporation Rate**: Decreased from 1 Å/s to 0.2 Å/s. At higher deposition rates, tensile stress (due to thermal expansion) in the Cr layer could deform the resist profile and increase sidewall roughness due to Cr collapse during lift-off. Lowering the rate minimized stress-induced cracking and improved edge definition.

3. **Increased Sonication Power**: Raised from 50% to 75% during lift-off. This enhancement improved lift-off completeness but required close monitoring to avoid cracking of the carbon mask, which could compromise the subsequent IBE step and damage the pattern.

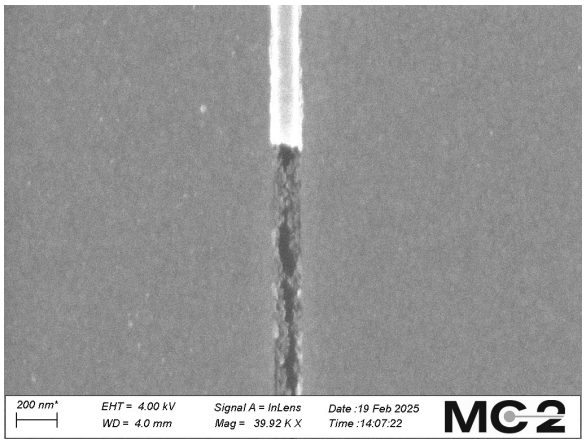

(a) Slit between two pillars prior to process improvements

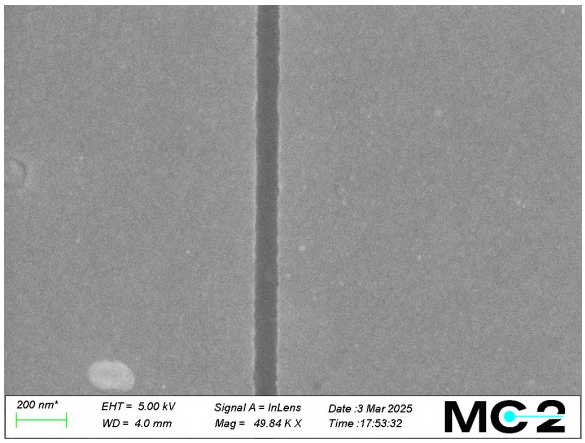

(b) Slit between two pillars after applying optimizations

Figure 4.4: Nanofabrication improvements: enhanced sidewall definition in a 100 nm slit, achieved by reducing Cr deposition rate to 0.5 Å/s. Further refinement was obtained at 0.2 Å/s.

One inherent limitation of the single-lithography process is the large contact area of the mesas, which results in low c-axis resistance, often approaching the noise threshold of the measurement system (see **Chapter 5**). However, using underdoped films with $p \sim 0.11$ allowed measurable signals to be obtained. For better signal quality, higher resistance values would be ideal, which could be realized by reducing the mesa area. Yet, this reduction poses challenges for making reliable wire bonds (needed for electrical contact with the structures). To address these concerns, a more advanced three-step lithography method was implemented (detailed in the following section).

Additionally, the contact resistance between the underdoped YBCO and the Au layer was consistently high across all samples, which masked the intrinsic c-axis transport properties. As four-point measurements were not feasible in the single-lithography design, we instead employed UV/ozone treatment.

The fabricated chip underwent UV/ozonation at 150^0C for 2 hours, followed by a 2-hour cooldown to room temperature under continuous UV/ozone exposure. This ozonation protocol, as previously established by our group [116], was effective in improving transport in YBCO nanowires. Their results showed that the transition temperature became sharper and the critical current density J_c improved, due to partial oxygen reintroduction into damaged regions. This effect helped reduce contact resistance and enabled the observation of the characteristic c-axis upturn behavior expected for underdoped YBCO More details are discussed in **Chapter 6**.

4.2 Nanofabrication of Mesa Devices – Three-Lithography Process

To address the issue of low resistance values in the previous design, we implemented a new mesa structure with a significantly reduced pillar area to $10 \times 10\ \mu m^2$. Achieving this reduction required transitioning from a single-lithography process to a more complex three-step lithography procedure. In parallel, we attempted to eliminate contact resistance by converting the setup into a four-point measurement configuration. This involved

splitting the Au layer on the central pillar. However, due to a minor oversight in the design, the middle pillar remained laterally connected through the Au layer, preventing successful four-point isolation. Despite this, the issue is relatively minor and can be corrected in future device iterations.

Employing multiple lithography steps on YBCO presents a significant challenge, as the material is highly sensitive and prone to degradation, especially due to oxygen out-diffusion. Nevertheless, we developed a reliable approach that involved protecting the YBCO with an insulating CeO_2 layer. This allowed us to successfully fabricate working mesa structures with reduced pillar areas and large contact pads suitable for wire bonding (to ensure electrical connection to the devices), as shown in **Figure 4.5**.

Amorphous CeO_2 was selected (after careful evaluation among other potential options), due to its excellent insulating properties, which mitigate the risk of lateral shorts during contact patterning. Additionally, it can be sputtered at room temperature, which is ideal for preserving YBCO integrity. Our group also has prior experience using CeO_2 as a buffer layer in SQUID magnetometer fabrication on bicrystals [117]. This novel process, though initially untested and risky, was ultimately successful after optimization.

The YBCO film thickness remained at 50nm, while the residual YBCO in the surrounding areas after etching was approximately 10nm. The slit spacing between pillars was reduced to 1 μm, and the contact pad dimensions were set to 200×400 μm. Two fabrication paths were pursued in parallel: on chip KCS2520, contact patterning was done via ion beam etching (IBE), while on chip KCS2521, a wet etch using Au etchant was employed.

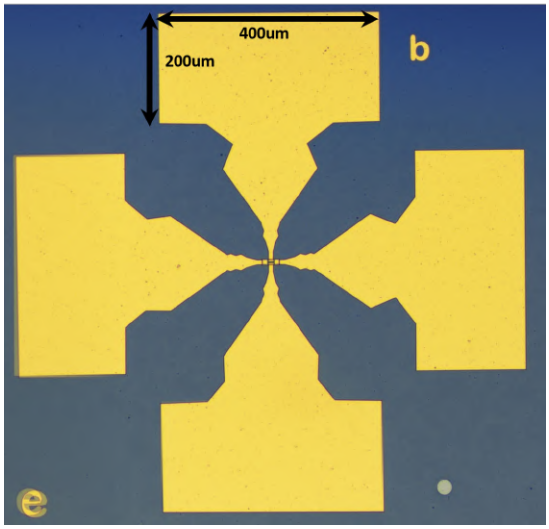

(a) Optical image of mesa device after three lithography steps

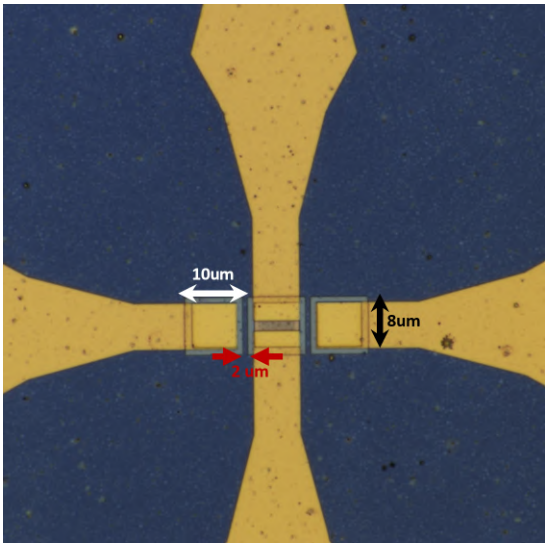

(b) Zoomed optical image of the pillar region

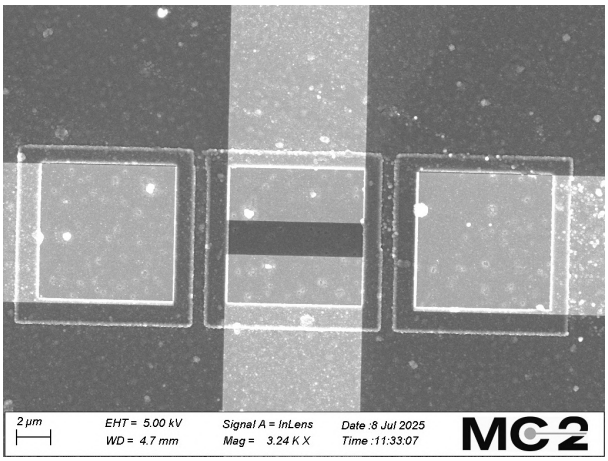

(c) SEM image of the pillar region

Figure 4.5: Optical and SEM images of the finalized mesa devices.

The fabrication steps of the first lithography round followed the same procedure outlined in the previous section for the 100×100 μm^2 mesas, with the only difference being the reduced pillar area (10×10 μm^2) and slit spacing (1 μm). Chips KCS2520 and KCS2521 were processed in parallel and only diverged during the third lithography step.

Overview of the Second Lithography Process

The second lithography was necessary to define the contact pad openings in the CeO_2 insulating layer, allowing for contact patterning in the subsequent lithography step. The process is illustrated in **Figure 4.6** and summarized as follows:

1. Devices were ozonated after the first lithography step. While not essential, this step was performed to repair potential damage in the YBCO layer [116].
2. A 115 nm, thick amorphous CeO_2 layer was sputtered over the entire chip. This layer acts as an insulating barrier, protecting YBCO during subsequent fabrication stages and preventing lateral shorts, as it is highly insulating.
3. Approximately 100 nm of amorphous C was deposited via PLD. As in the first lithography, this carbon layer functioned as a hard mask. Good adhesion of C on CeO_2 was observed.
4. The same two-layer EBL resist system used previously was spin-coated: MMA 8.5 EL4 and ARP 13 6200 (1:1 ratio).
5. Electron-beam lithography was used to define the negative of the $8\times8\mu$m contact pad openings. The chip was fully exposed due to the use of a positive resist (so everything but the contact pads were exposed). A 100 kV, 1 nA beam was used, and a multipass strategy was adopted to avoid stitching errors. Standard development was performed using Oxylene, IPA, and MIBK (3:1). The $8\times8\mu$m openings were initially chosen to have a good tolerance on alignment mistakes, since it is fundamental that we don't access the YBCO on the sides of the pillar (to avoid ab-plane conduction). However, this revealed a small issue which would affect our measurements. In future fabrications the size of the holes (contact pad openings) will be corrected to match almost exactly the dimensions of the pillar, since our lithography alignment is very robust.

6. A 10 nm Cr layer was deposited via e-beam evaporation at a rate of 0.2 Å/s to serve as a lift-off mask.
7. Lift-off was carried out using heated Remover 1165 (20 minutes), followed by 1 minute of sonication in Remover 1165 at 75% power, and 1 minute in IPA with the same power. The resulting structures were inspected via optical microscopy and SEM.
8. The unprotected carbon was removed using a gentle oxygen plasma process. RIE was performed for 5 minutes at 50W, 100mTorr, followed by a 1-hour etch at 15W, 100mTorr.
9. Cryogenic IBE was then used to etch through the CeO_2 layer in the defined openings, stopping at the Au layer beneath. The cryo stage was chosen to minimize YBCO damage. This step was particularly challenging due to the weak Au signal in SIMS. It is worth noting that a thin Ti layer was added to enhance the SIMS signal and give better indication of when we are fully touching Au in the holes, without any CeO_2 remaining.
10. A final gentle oxygen plasma step (3 minutes at 50 W and 1 hour at 15 W, 100 mTorr) was used to remove any remaining carbon.
11. As a final step, the chips were ozonated again to heal any microcracks potentially formed in the CeO_2 layer. These microcracks would otherwise result in lamination (and therefore destruction) of the CeO_2 layer later in the process.

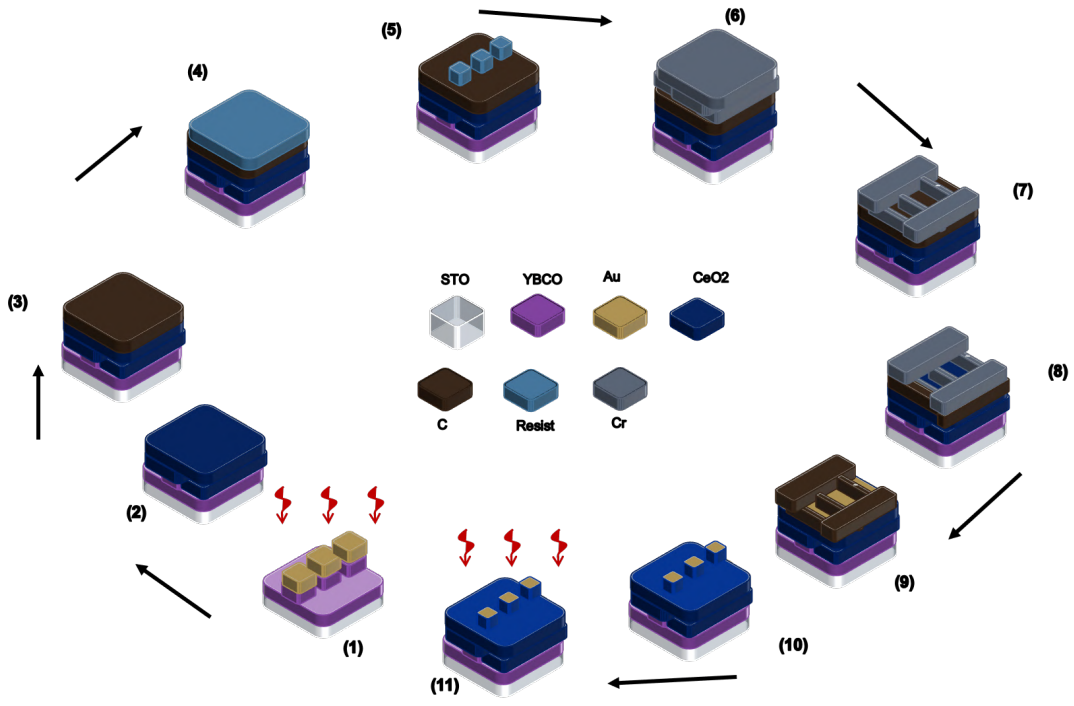

Figure 4.6: Nanofabrication process flow for the second lithography step

As shown in the SEM images (**Figure 4.7**), the holes are clearly visible and match the expected dimensions from our design.

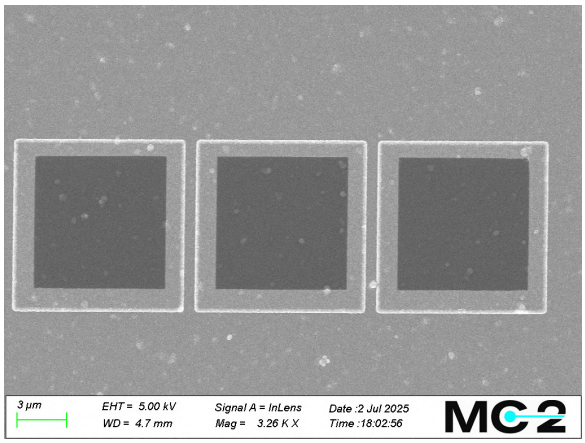

(a) SEM image of mesa device

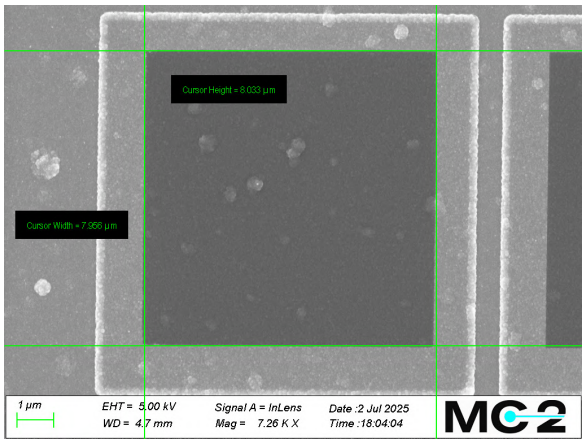

(b) Zoomed-in SEM image of mesa device

Figure 4.7: SEM images of the holes through CeO_2 for both chips

The overall logic and workflow of this fabrication round followed a similar methodology to the first nanofabrication round. However, introducing CeO_2 as a new material introduced various unforeseen issues. While C adhesion on CeO_2 proved unproblematic, microcracks developed in CeO_2 during IBE and oxygen plasma steps, alongside weak adhesion of Au. These problems were hidden during the second lithography round, and manifested quite visibly during the third round, as shown in **Figure 4.8**.

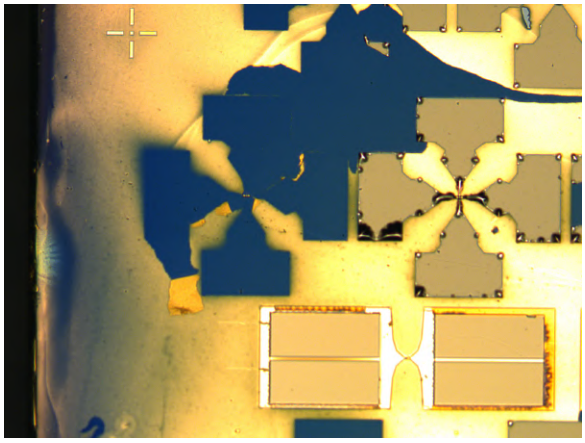

(a) Optical image showing poor Au adhesion on CeO_2

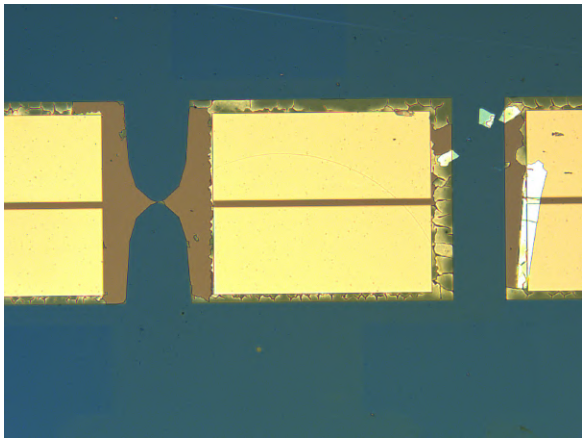

(b) Optical image showing cracks in CeO_2

Figure 4.8: Optical images of problems encountered during the third lithography step

It was discovered then that both IBE and oxygen plasma induced microcracks in the CeO_2 layer. These cracks grew further during thermal steps such as Au evaporation, or chemical treatments like Au etching. This is evident in **Figure 4.8(b)**. The local heating during the evaporation of thick Au films induces stress on CeO_2, potentially expanding the cracks and in the worst-case, interfacial delamination (visible as wrinkles), especially in large structures like the nanobridges. In addition, Au exhibited poor adhesion to CeO_2, as observed in **Figure 4.8(a)**, where Au wrinkles and lifts off, removing entire contact pads.

Overview of the Third Lithography Process

The following outlines the nanofabrication procedure during the third lithography, required to define the large contact pads for wire bonding. **Figure 4.9** shows the process for KCS2520, where IBE was used for patterning, while **Figure 4.10** depicts the Au-etchant method used for KCS2521.

KCS2520 - The IBE sample

1. 130nm of Au was sputtered at room temperature over the entire chip to form the contact layer.
2. 100nm of C was deposited using pulsed laser deposition (PLD).
3. A bilayer of MMA 8.5 EL4 and ARP 6200 1:1 was spin-coated.
4. Contact patterns were exposed via EBL at 100 kV, 1 nA. Standard development followed.
5. A 10 nm Cr layer was evaporated at 0.2Å/s to serve as a lift-off mask.
6. Lift-off was performed in heated Remover 1165 at 75^0C for 20 minutes, followed by 1 minute sonication in Remover 1165 and 1 minute in IPA.
7. Oxygen plasma was applied at 50 W, 100 mTorr for 20 minutes to remove unprotected C. No gentle RIE step was necessary, as Au was already present beneath the C layer, hence protecting CeO_2.
8. Cryogenic IBE was used to etch Au shorts and define the contact pads.
9. A final gentle oxygen plasma cleaning step (5 minutes at 50W + 1 hour at 15W, both at 100 mTorr) was done to eliminate residual C.
10. Ozonation was performed to enhance Au adhesion. Although adhesion was acceptable prior to this step, ozonation improved bonding reliability.

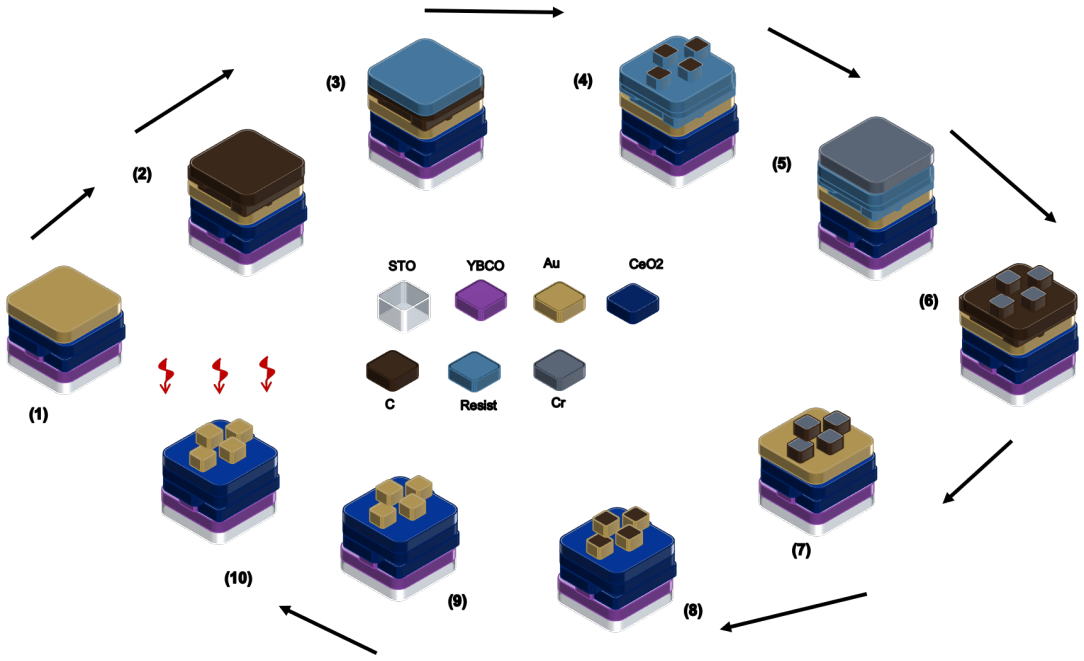

Figure 4.9: Nanofabrication flow during the third lithography for KCS2520, with contacts patterned via IBE

KCS2521 - The Au-etchant sample

1. 130nm of Au was sputtered at room temperature to form the contact layer.
2. The standard bilayer EBL resist was spin-coated. No C deposition was done, since Au-etchant induced cracks in amorphous C even after just 3 seconds (**Figure4.11**).
3. EBL exposure of the entire chip was done here. Multipass was again utilized to avoid stitching issues, as large areas were involved. Development times were also modified. Oxylene process remained the same, but MIBK was different. 30s in MIBK:IPA 3:1 for the MMA layer, followed by the usual 10 seconds in IPA to stop the developer's action. This ensured a smaller undercut to protect the Au contacts during wet etching.
4. The chip was dipped in Au-etchant for 3s, followed by immediate rinsing in H_2O to neutralize the etchant. This wet process removes Au laterally and must be carefully timed. Au on the contact pads is protected by the resist layer. However, prolonged exposure in Au-etchant would remove them as well. This happens because wet etching does not affect the resist itself and can easily get underneath it, aided as well by the smaller, yet still present, undercut. In addition, water is very well known to damage the superconducting properties of YBCO, especially in underdoped samples. However, CeO_2 was acting as a protection and encapsulating mask for the ab-planes at this stage, so that only a very small section of c-axis YBCO was exposed on top of the pillars. Therefore this minimizes the risk of damage to the material, as oxygen mobility is reduced in c-axis (out-difussion of oxygen is slower). To conclude, our short rinse and CeO_2 encapsulation minimized this risk.
5. The sample was placed in hot acetone at 50^0C for 12 minutes to remove remaining resist.
6. Ozonation was performed to improve Au adhesion.

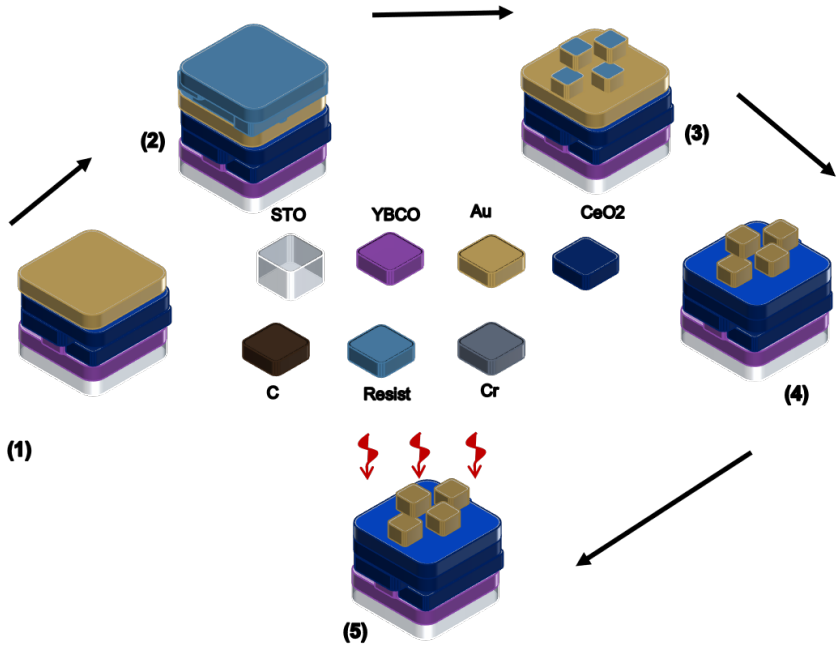

Figure 4.10: Nanofabrication flow during the third lithography for KCS2521, with contacts patterned via Au-etchant

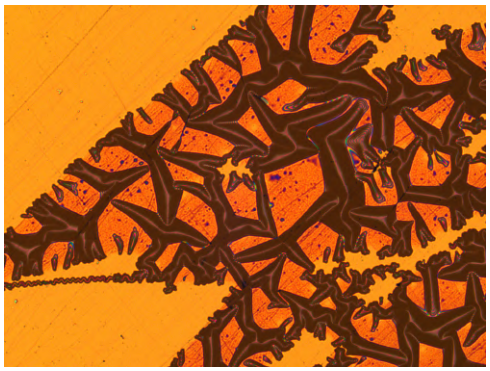

Figure 4.11: YBCO covered by in-situ Au and C. Cracks formed in C after only 3s immersion in Au-etchant

Conclusions of the Three-Lithography Process

As we hinted at the end of the previous sections (**Overview of the Second Lithography Process and Overview of the Third Lithography Process**), we faced several problems and had to introduce changes in the nanofabrication process to resolve them:

1. We introduced an ozonation step after the second IBE. In [118], CeO_2 was employed as an insulating layer for memory devices. They demonstrated that UV/ozone treatment could suppress crack formation due to chemical processes. We adopted a similar treatment to reduce microcrack formation and heal CeO_2.
2. The in-situ Au thickness was reduced from 70nm to 20nm to alleviate stress. Moreover, Au evaporation was replaced with Au sputtering, which ensures better adhesion, more uniform coverage (especially in the etched holes), and is considered less damaging.
3. To further improve Au adhesion on CeO_2, ozonation was repeated. As discussed in [119], UV/ozone treatment oxidizes Au slightly, enabling electron sharing with the oxide layer and improving interfacial adhesion. Since Au oxide is unstable, it naturally disappears later. In that work, noticeable improvement of both Au and Pt adhesion to oxides was reported. We observed improved adhesion in KCS2520 and KCS2521, despite performing the ozonation after the contacts had been patterned and not immediately after deposition of Au as suggested in [119]. However, it is important to note that washing ozonated Au in solvents, especially H_2O, can reduce adhesion effectiveness.

An important consideration was the effect of ozonation on the encapsulated YBCO layer. This was previously investigated in [116], where nanowires encapsulated with Pt and Au were subjected to ozonation. The study found that UV/ozone treatment primarily affects the ab-plane exposed YBCO, where oxygen has higher mobility. For fully encapsulated YBCO, the encapsulation blocks oxygen in-diffusion. Nonetheless, the UV/ozone environment at 150^0C helps redistribute the existing oxygen content, leading to a slightly increased T_c and a narrower transition width. Additionally, contact resistance was improved.

Despite the challenges faced throughout the three lithography steps, we successfully fabricated smaller area mesa devices using both IBE and Au-etching techniques.

(a) Optical image of KCS2520 with IBE-patterned contacts

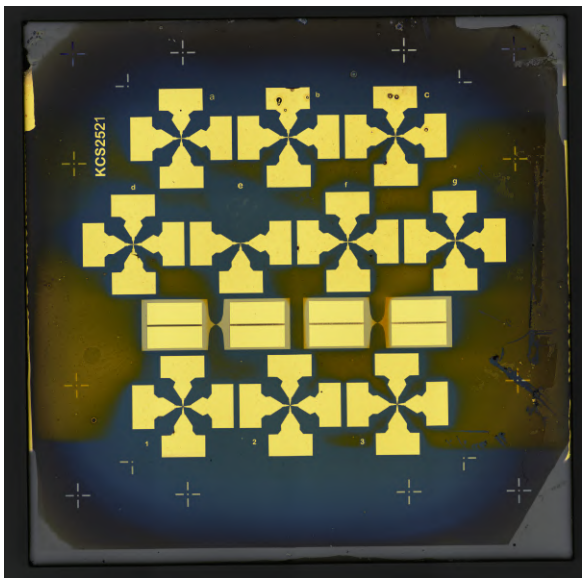

(b) Optical image of KCS2521 with Au-etched contacts

Figure 4.12: Final fabricated chips after third lithography step

Unfortunately, wire bonding could not be performed on KCS2521 due to continued poor Au adhesion on CeO_2, even after ozonation. In contrast, the KCS2520 sample, with IBE-defined contacts, exhibited good adhesion and all devices were functional.

Potential improvements for future fabrication rounds include:

1. Correcting the CAD mask design to enable proper four-point measurements, eliminating the influence of contact resistance. As hinted at earlier, the 8×8μm openings were initially chosen to have a good tolerance on alignment mistakes and avoid lateral contact with YBCO (on the sides of the pillar). However, this extra precaution step, made all of our measurements effectively three-point (more explained in **Chapter 5** about the experimental setup and measurement scheme), due to Au-shorts around the opened holes. This meant we would always have contact resistance present in our measurements. In future fabrications, the size of the holes will be corrected to match almost exactly the dimensions of the pillar, since our lithography alignment is very robust. This would enable us to achieve 4-point measurements.
2. Reducing the mesa pillar area further to $3 \times 3\ \mu m^2$ or even $1 \times 1\ \mu m^2$ to achieve higher resistance values. However, this will introduce additional challenges, which are the reason we have not managed yet at this point.
3. Refining fabrication steps by minimizing the number of ozonation treatments by introducing interfacial adhesion layers such as Ti, which may improve both adhesion and SIMS signal quality. Additionally, using other encapsulation materials like Parylene-N, which can be removed with oxygen plasma alone, could simplify the process and eliminate IBE steps.

5

Transport in YBCO Mesas

In this thesis, nanofabricated mesa structures are used to investigate the c-axis transport properties of underdoped YBCO thin films. This chapter presents an overview of the transport measurements performed on these mesas, with particular focus on temperature-dependent resistance ($R(T)$), current–voltage characteristics (IVCs), as well as on the design strategies used to isolate and probe the c-axis conduction.

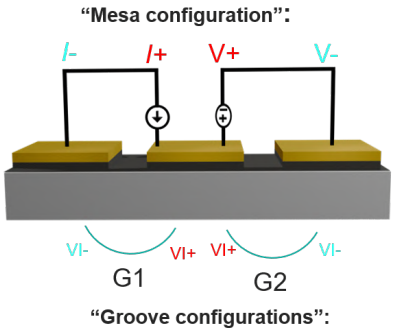

(a) Mesa device fabricated with a single lithography step. Voltage probe and current source are connected for out-of-plane transport measurements.

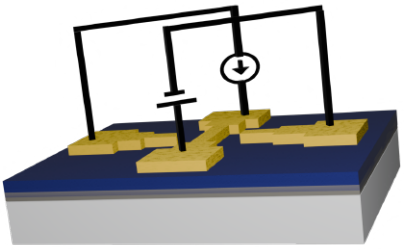

(b) Mesa device fabricated using three lithography steps

Figure 5.1: Measurement schematics for YBCO mesa devices

5.1 Experimental Setup

Transport measurements were carried out using a Physical Property Measurement System (PPMS) with a base temperature of 300 mK and a magnetic field capability of up to 14 T. The mesa devices were designed to access the c-axis transport in underdoped YBCO. Two device architectures were used: a simpler one-step lithography process (Fig. 5.1a) and a more refined three-step lithography design (Fig. 5.1b).

Our measurements focus on underdoped YBCO films with a hole concentration $p \approx 0.11$ and an average superconducting transition temperature $\bar{T}_c$ in the range of 52–55 K. At this doping level, YBCO is expected to exhibit enhanced anisotropy between ab-plane and c-axis, revealing YBCO's quasi-two-dimensional nature more prominently.

R(T) Measurements

One of the key goals of this work is to study the temperature dependence of the c-axis resistance, $R_c(T)$. These measurements allow us to observe the characteristic transport behavior of c-axis, in the pseudogap phase. In underdoped YBCO, the c-axis resistance exhibits a crossover from metallic to semiconducting behavior as temperature is lowered as reported by [28] in single crystals. There are many theories, attempting to explain this behavior.

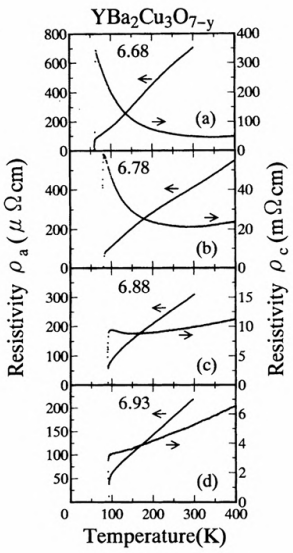

(a) Temperature dependence of in-plane (ρ_a) and out-of-plane (ρ_c) resistivity for YBCO crystals with different oxygen contents (adapted from [28]).

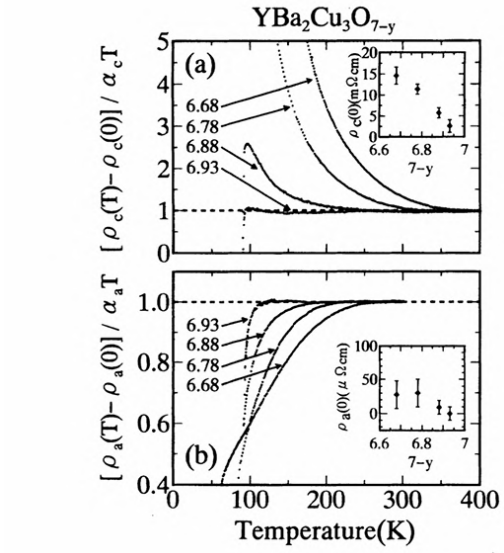

(b) Normalized resistivity plots $[\rho(T) - \rho(0)]/\alpha T$ for (a) c-axis and (b) a-axis transport, showing correlated crossover behavior for different doping levels (adapted from [28]).

Figure 5.2: $R_c(T)$ in single crystals

Through these measurements, we aim to identify this transition through detailed $R_c(T)$ measurements and compare the behavior to in-plane transitions, shedding light on the anisotropic superconducting properties.

Current–Voltage Characteristics and Conductance Spectroscopy

We also characterized the YBCO–Au interface by performing superconductor–normal metal (SN) conductance spectroscopy on the mesa structures. This is achieved by measuring the I–V characteristics (IVCs) at various temperatures and extracting the differential conductance dI/dV.

The IVCs are obtained by applying a bias current in fine steps and recording the corresponding voltage response. The differential conductance is calculated by numerical differentiation. Features such as zero-bias conductance peaks (ZBCPs), subgap features,

or Andreev reflection signals can provide crucial information about the superconducting order symmetry.

In the case of *c*-axis transport, the YBCO surface is oriented along the (001) crystallographic plane, which yields a characteristic V-shaped conductance profile, as shown in **Figure 5.3** (a). Typically in BCS-like superconductors, the conductance profile has more of a U-shape. The reason for the V-shape in our case, is due to the symmetry of the order parameter, which is d-wave. This means that along the nodal directions, the superconducting gap is 0, even at 0 K. Therefore the shape of the conductance is different for YBCO compared to conventional, BCS-like superconductors.

Due to surface roughness in the grown YBCO films and the size of the mesa pillars junctions, other crystallographic orientations may be present during measurements. This means there will also be (100), (010), and (110) surfaces potentially exposed. The shape of the measured conductance curve can thus provide insight into the actual surface orientation. For instance, the appearance of a Zero Bias Conductance Peak is indicative of an *ab*-plane (110) orientation. This feature also suggests the presence of Andreev Bound States (ABS) at zero energy.

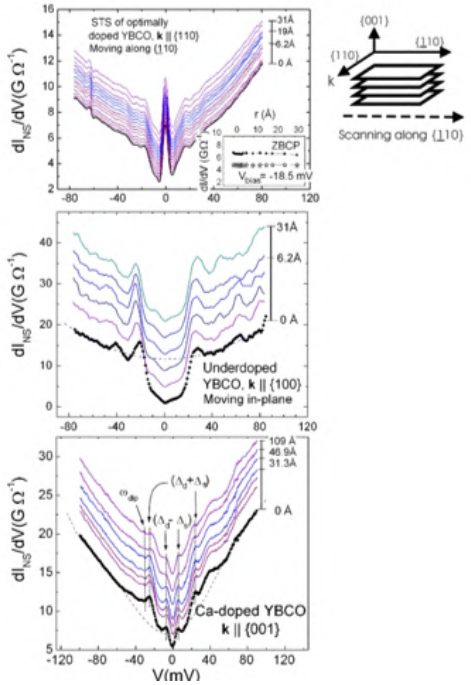

Figure 5.3: Different conductance shapes depending on the YBCO surface orientation (adapted from [4])

In addition, our mesa devices offer a new way of performing conductance spectroscopy measurements, without relying on Scanning-Tunneling-Microscopy (STM) tips.

These measurements are essential both for understanding fundamental superconducting phenomena and for optimizing device performance in hybrid superconductor structures, where the quality of the interface plays a decisive role.

5.2 Measurement Configurations and Resistance Extraction

Figure 5.4 shows the equivalent circuit used to model the mesa structure and its various resistive components during transport measurements. The goal is to extract the c-axis resistance, R_c, of the YBCO mesas. Due to the current device layout, two primary measurement configurations are employed, based on three-point (Mesa) and two-point (Groove) measurements respectively.

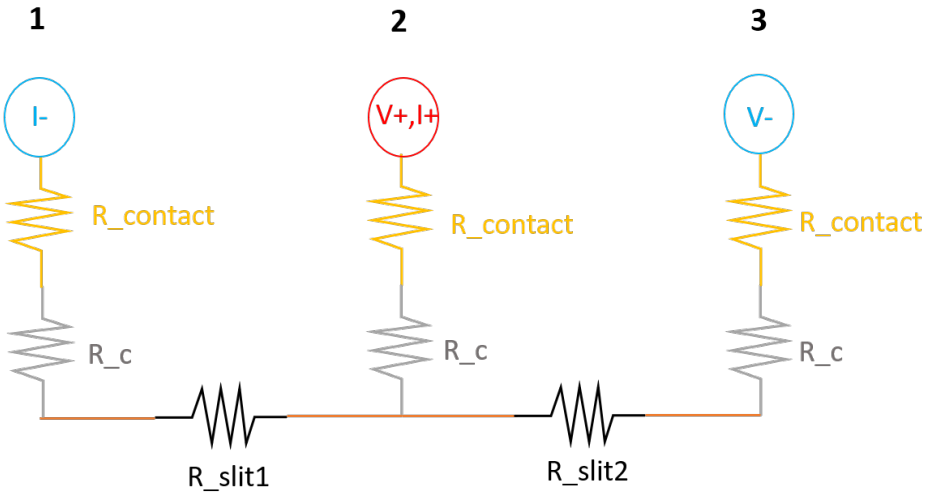

Figure 5.4: Equivalent electrical circuit for the mesa device, illustrating the two measurement configurations.

The first approach is referred to as the Mesa configuration, which corresponds to a three-point measurement. In this configuration, we use a current bias between pillars 1 and 2, while probing the voltage between pillars 2 and 3. The total measured resistance in this case includes both the intrinsic c-axis resistance and the contact resistance at the central pillar:

$$R_{\text{mesa}} = R_c + R_{\text{contact}} \tag{5.1}$$

This configuration is optimized to measure R_c with minimal contributions from lateral transport. However, it does include one R_{contact} term, making absolute extraction of R_c dependent on contact quality. As we will see in **Chapter 6**, the contact resistance was quite high and has an unknown temperature dependence.

The second configuration, termed the Groove configuration, is essentially a two-point measurement across two pillars and the slit in-between. We send a current bias through pillars 1 and 2, while probing the voltage between these two pillars as well. This is what we referred to as Groove 1 (G1) measurement in **Chapter 6**. When current biasing pillars 2 and 3, as well as measuring the voltage between them, we called it Groove 2 (G2). In this case, the measured resistance includes contributions from two pillars, two contacts, and the intervening exposed YBCO region:

$$R_{\text{groove}} = 2R_c + 2R_{\text{contact}} + R_{\text{slit}} \tag{5.2}$$

The R_{slit} term refers to the resistance of the ion-milled YBCO region between the two pillars. During later parts and **Chapter 6**, we refer to this part specifically as the "Slit", not to be confused with "Groove", which includes the contributions from the 2 pillars as well. This slit region has undergone additional processing and thus often exhibits degraded superconductivity or enhanced scattering, resulting in a significant resistance contribution. In practice, R_{slit} tends to dominate this configuration. While it would be ideal for the slit region to retain some superconducting properties, the measurement remains useful as long as the region remains conductive and Ohmic.

5.3 Estimation of c-axis Resistance and Underdoped samples

This section provides a quantitative estimation of the expected resistance values for mesa devices fabricated with both single- and three-step lithography processes, using both optimally doped and underdoped YBCO. These calculations help justify the use of underdoped films for effective detection of c-axis transport. As the value of the contact resistance is unknown, we neglect it in the following sections.

5.3.1 One-step Lithography: Resistance Limitations in Optimally/Overdoped YBCO

The following estimates are based on the known resistivity values for YBCO thin films from our group [34] and the anisotropy ratios reported in [28]. For overdoped YBCO, the in-plane resistivity at 100 K is approximately:

$$\rho_{ab}^{100\,\text{K}} = 65\ \mu\Omega \cdot \text{cm} = 65 \times 10^{-8}\ \Omega \cdot \text{m} \tag{5.3}$$

The anisotropy ratio at this temperature is:

$$r = \frac{\rho_c^{100\,\text{K}}}{\rho_{ab}^{100\,\text{K}}} \approx 75 \tag{5.4}$$

Using this ratio, the estimated out-of-plane resistivity is:

$$\rho_c^{100\,\text{K}} = r \cdot \rho_{ab^{100\text{K}}} = 4.88 \times 10^{-5}\ \Omega \cdot \text{m} \tag{5.5}$$

Assuming a typical mesa thickness of $t = 50$ nm $= 50 \times 10^{-9}$ m and a contact area $A = 10000\ \mu\text{m}^2 = 10^{-8}\ \text{m}^2$, we can estimate the c-axis resistance using:

$$R_c = \rho_c \cdot \frac{t}{A} = 4.88 \times 10^{-5} \cdot \frac{50 \times 10^{-9}}{10^{-8}} = 2.44 \times 10^{-4}\ \Omega = 0.244\ \text{m}\Omega \tag{5.6}$$

As seen, the expected R_c at 100K for optimally or overdoped YBCO with this mesa area is extremely small. It is in the order of a few hundred micro-ohms. To generate a detectable voltage signal (e.g., 1 μV), one would need to apply a current of approximately 4.1 mA:

$$V = IR \Rightarrow I = \frac{V}{R} = \frac{1\ \mu\text{V}}{0.244\ \text{m}\Omega} \approx 4.09\ \text{mA} \tag{5.7}$$

1μV of signal is still very small signal close to the noise floor of the measurement setup. Meanwhile the current to obtain is already half of the operational limit of the PPMS system, which is restricted to 8 mA. These low current levels are to avoid sample heating and equipment damage. Although external setups were attempted to reach higher than 8 mA current levels, these devices tended to overheat, which made a proper interpretation of the data cumbersome.

In the groove configuration, the current flows laterally from one mesa pillar to the other through the ion-milled slit region. This configuration introduces a significant resistance contribution from the exposed YBCO area, especially after etching. Based on fabrication parameters, the thickness of the YBCO film in the slit is estimated to be approximately 20 nm.

From prior measurements, the sheet resistance at room temperature for a 30 nm thick YBCO film [34] is known to be:

$$R_{\square}^{30\,\mathrm{nm},\,300\,\mathrm{K}} = 63\ \Omega \tag{5.8}$$

Using the inverse scaling with thickness, the sheet resistance for a 20 nm film becomes:

$$R_{\square}^{20\,\mathrm{nm},\,300\,\mathrm{K}} = 63\ \Omega \times \frac{30}{20} = 94.5\ \Omega \tag{5.9}$$

In optimally or overdoped YBCO, the sheet resistance typically decreases by a factor of 3 when cooling down from 300 K to 100 K. Therefore, the sheet resistance at 100 K is estimated as:

$$R_{\square}^{20\,\mathrm{nm},\,100\,\mathrm{K}} = \frac{94.5}{3} = 31.5\ \Omega \tag{5.10}$$

The geometry of the slit, where current travels from one pillar to the other, has a length $l = 2\ \mu$m and width $w = 100\ \mu$m. The resistance of the slit at 100 K is given by:

$$R_{\mathrm{slit}}^{100\,\mathrm{K}} = R_{\square}^{100\,\mathrm{K}} \cdot \frac{l}{w} = 31.5\ \Omega \cdot \frac{2}{100} = 0.63\ \Omega \tag{5.11}$$

Similarly, at room temperature:

$$R_{\mathrm{slit}}^{300\,\mathrm{K}} = R_{\square}^{300\,\mathrm{K}} \cdot \frac{l}{w} = 94.5\ \Omega \cdot \frac{2}{100} = 1.89\ \Omega \tag{5.12}$$

Taking into account the contribution of the two mesa pillars, each with $R_c \approx 0.244$ mΩ at 100 K, the total resistance measured in the groove configuration becomes:

$$R_{\mathrm{groove}}^{100\,\mathrm{K}} = R_{\mathrm{slit}}^{100\,\mathrm{K}} + 2R_c^{100\,\mathrm{K}} = 0.63\ \Omega + 2 \cdot 0.000244\ \Omega = 0.630488\ \Omega \tag{5.13}$$

As evident from the estimation above, the total groove resistance is overwhelmingly dominated by the resistance of the slit region. The contribution from the intrinsic *c*-axis resistance of the two pillars is negligible, on the order of sub-milliohms (only 0.08% of the R_{groove}), compared to the slit's value.

Furthermore, this high slit resistance not only masks the *c*-axis contribution but also introduces practical challenges during measurement. When higher currents are applied in an attempt to improve signal levels, the large power dissipation in the slit region leads to localized Joule heating. This thermal effect causes overheating issues.

These results further reinforce the earlier conclusion: in optimally or overdoped YBCO mesa devices, neither the mesa nor the groove configuration provides a viable path

to reliably extract the c-axis resistance with the current design. The use of underdoped YBCO, which exhibits higher out-of-plane resistivity, is therefore essential for enabling measurable and thermally stable R_c values within the operational current range (internal setup) of the PPMS system, which is limited to $I_{\max} = 8$ mA. For IVC measurements, we used an external setup, allowing us to reach higher currents.

5.3.2 One-step Lithography: C-axis Resistance Estimations in Underdoped YBCO

For underdoped YBCO with a hole concentration of approximately $p = 0.11$, the in-plane resistivity at 100 K is reported in [34] to be:

$$\rho_{ab}^{100\,\mathrm{K}} = 103\ \mu\Omega \cdot \mathrm{cm} = 103 \times 10^{-8}\ \Omega \cdot \mathrm{m} \tag{5.14}$$

The corresponding anisotropy ratio between the c-axis and ab-plane resistivities at this temperature is [28]:

$$r = \frac{\rho_c^{100\,\mathrm{K}}}{\rho_{ab}^{100\,\mathrm{K}}} \approx 2000 \tag{5.15}$$

From this, the c-axis resistivity can be estimated as:

$$\rho_c^{100\,\mathrm{K}} = r \cdot \rho_{ab}^{100\,\mathrm{K}} = 2000 \times 103 \times 10^{-8} = 0.0021\ \Omega \cdot \mathrm{m} \tag{5.16}$$

Using the mesa geometry with a thickness $t = 50$ nm $= 50 \times 10^{-9}$ m and a contact area $A = 10000\ \mu\mathrm{m}^2 = 10^{-8}\ \mathrm{m}^2$, the estimated c-axis resistance is:

$$R_c = \rho_c \cdot \frac{t}{A} = 0.00206\ \Omega \cdot \mathrm{m} \cdot \frac{50 \times 10^{-9}\ \mathrm{m}}{10^{-8}\ \mathrm{m}^2} = 0.011\ \Omega = 11\ \mathrm{m}\Omega \tag{5.17}$$

Compared to overdoped devices, the R_c value is significantly enhanced in underdoped films, bringing it within a measurable range. For instance, a detectable voltage signal of 1 μV would now require a current of:

$$I = \frac{V}{R} = \frac{1\ \mu\mathrm{V}}{11\ \mathrm{m}\Omega} \approx 91\ \mu\mathrm{A} \tag{5.18}$$

Although this is still a relatively small signal, we can increase the bias current without running into the potential trouble of overheating and setup limitations. Moreover, as we will detail in **Chapter 6**, imperfect contact resistance at the pillars, led to a low-transparency interface, which enabled conductance spectroscopy measurements and the manifestation of some interesting transport related to Andreev reflection phenomena.

In the same one-lithography design, the slit region is also composed of YBCO, with an estimated remaining thickness of 20 nm after ion milling. Based on our group's prior measurements [34]:

$$R_{\square}^{30\,\mathrm{nm},\,300\,\mathrm{K}} = 104\ \Omega \tag{5.19}$$

Using the inverse scaling with thickness, the room-temperature sheet resistance for a 20 nm thick film is:

$$R_{\square}^{20\,\mathrm{nm},\,300\,\mathrm{K}} = 104\ \Omega \times \frac{30}{20} = 156\ \Omega \tag{5.20}$$

Assuming a similar temperature dependence as in optimally doped YBCO, we estimate the sheet resistance at 100 K to decrease by a factor of approximately 3:

$$R_{\square}^{20\,\mathrm{nm},\,100\,\mathrm{K}} \approx \frac{156}{3} = 52\ \Omega \tag{5.21}$$

With the slit dimensions remaining the same ($l = 2\ \mu$m, $w = 100\ \mu$m), the resistance of the slit region at 100 K becomes:

$$R_{\mathrm{slit}}^{100\,\mathrm{K}} = R_{\square}^{100\,\mathrm{K}} \cdot \frac{l}{w} = 52\ \Omega \cdot \frac{2}{100} = 1.04\ \Omega \tag{5.22}$$

Likewise, the slit resistance at 300 K is:

$$R_{\mathrm{slit}}^{300\,\mathrm{K}} = 156\ \Omega \cdot \frac{2}{100} = 3.12\ \Omega \tag{5.23}$$

Including the two mesa pillar resistances ($R_c = 0.011\ \Omega$ each), the total resistance in the groove configuration at 100 K is:

$$R_{\mathrm{groove}}^{100\,\mathrm{K}} = R_{\mathrm{slit}}^{100\,\mathrm{K}} + 2R_c^{100\,\mathrm{K}} = 1.04\ \Omega + 2 \cdot 0.011\ \Omega = 1.062\ \Omega \tag{5.24}$$

While the contribution of R_c is still small compared to the slit, it is no longer negligible (now it is 2% of the R_{groove}), and subtle changes in c-axis transport can now be resolved, especially when temperature-dependent behavior is considered.

The analysis confirms that by reducing the doping level, and consequently increasing the c-axis resistivity, the one-lithography mesa design with $100 \times 100\ \mu\mathrm{m}^2$ pillar areas becomes viable for probing out-of-plane transport properties. The resulting resistance values fall within an accessible range for standard transport and spectroscopy techniques, without requiring excessive currents that could jeopardize device stability.

5.3.3 Three-step Lithography: Enhanced C-axis Resistance in YBCO Mesas

In this section, we focus on the three-lithography mesa design, which enables reduced contact areas. While all measurements were performed on underdoped samples, despite being more challenging to fabricate, this approach is, in principle, also applicable to optimally doped or overdoped YBCO films. The underdoped film used here exhibited an average transition temperature $\bar{T}_c$ of 55 K, suggesting a doping level close to $p = 0.11$, which justifies the use of the same resistivity values from the previous section.

Mesa Resistance Estimation

In the three-lithography geometry, the mesa thickness remains $t = 50\ \mathrm{nm} = 50 \times 10^{-9}$ m, but the contact area was significantly reduced to $A = 100\ \mu\mathrm{m}^2 = 10^{-10}\ \mathrm{m}^2$. The estimated c-axis resistance at 100 K is then:

$$R_c = \rho_c \cdot \frac{t}{A} = 0.00206\ \Omega \cdot \mathrm{m} \cdot \frac{50 \times 10^{-9}}{10^{-10}} = 1.1\ \Omega \tag{5.25}$$

By shrinking the pillar area by a factor of 100 compared to the one-lithography design, we achieved a hundred-fold increase in R_c. This improvement directly translates to enhanced voltage signals. For instance, a voltage of 1 μV can now be obtained with just 1 μA of current:

$$I = \frac{V}{R} = \frac{1\ \mu\text{V}}{1.1\ \Omega} \approx 1\ \mu\text{A} \tag{5.26}$$

This is a substantial improvement over the previous geometry and allows for clearer detection of the characteristic c-axis behavior, such as the expected upturn in resistance indicating a crossover from metallic to semiconducting transport. In fact, further reduction of the pillar area to $1 - 3 \times 1 - 3\ \mu\text{m}^2$ would push R_c into the 10s of Ω range at 100 K.

In the same three-lithography device, the slit region also consists of YBCO, with an estimated thickness of 10 nm after ion milling. Using previous calibration data [34], the sheet resistance at room temperature is:

$$R_{\square}^{30\,\text{nm},\,300\,\text{K}} = 104\ \Omega \quad \Rightarrow \quad R_{\square}^{10\,\text{nm},\,300\,\text{K}} = 104 \cdot \frac{30}{10} = 312\ \Omega \tag{5.27}$$

Assuming a similar temperature dependence as in optimally doped films, we estimate a threefold reduction in resistance at 100 K:

$$R_{\square}^{10\,\text{nm},\,100\,\text{K}} \approx \frac{312}{3} = 104\ \Omega \tag{5.28}$$

With the slit dimensions of $l = 1\ \mu$m and $w = 10\ \mu$m, the slit resistance becomes:

$$R_{\text{slit}}^{100\,\text{K}} = R_{\square}^{100\,\text{K}} \cdot \frac{l}{w} = 104\ \Omega \cdot \frac{1}{10} = 10.4\ \Omega \tag{5.29}$$

$$R_{\text{slit}}^{300\,\text{K}} = 312\ \Omega \cdot \frac{1}{10} = 31.2\ \Omega \tag{5.30}$$

Including the contributions from the two mesa pillars ($R_c = 1.1\ \Omega$ each), the total groove resistance at 100 K is:

$$R_{\text{groove}}^{100\,\text{K}} = R_{\text{slit}}^{100\,\text{K}} + 2R_c = 10.4\ \Omega + 2 \cdot 1.1\ \Omega = 12.6\ \Omega \tag{5.31}$$

This value clearly demonstrates a measurable impact of c-axis resistance on the total signal (the contribution is increased to 17.5% of the R_{groove}), making it possible to resolve c-axis effects even in standard groove configurations.

Comparison to Overdoped Case

If instead an overdoped film was used, where c-axis transport is less resistive—the expected R_c with the same mesa geometry would be:

$$R_c^{\text{OD}} = 0.0244\ \Omega = 24.4\ \text{m}\Omega \tag{5.32}$$

This is two orders of magnitude greater than the R_c values obtained in our one-lithography devices using overdoped films. However, this is not yet a sufficient rescaling of the resistance. Therefore, overdoped samples would benefit from a further reduction in area to more reliably extract c-axis behavior.

To conclude this chapter, probing c-axis transport in YBCO remains a delicate task, requiring careful control of fabrication, geometry, and contact interfaces. Both the single-lithography and three-lithography approach allowed us to successfully resolve out-of-plane resistance contributions.

6

Results and Discussions

In this section, we present measurement results from two chips of mesa devices. Specifically, we discuss $R(T)$ and current-voltage characteristics (IVC) obtained from both single-lithography and triple-lithography fabricated mesas. The single-lithography devices are referred to as **KCS2512**, while the triple-lithography structures are labeled **KCS2520**. These names are related to the names of the chips, from which they were fabricated onto. The KCS2520 chip contains seven mesa devices and two Au-shunted nanobridges, whereas KCS2512 consists of thirty-six mesa structures only (arranged in a matrix layout). No nanobridges were present on the KCS2512 sample.

As a reminder from **Chapter 5**, three-point measurements are called "Mesa" measurements, while two-point measurements are referred to as "Groove" measurements. In the Groove measurements, when referring specifically and only to the ion-milled YBCO remaining between 2 pillars, it is called "Slit".

6.1 Single-lithography Mesas KCS2512 - Before Ozonation

In this part we will discuss the results of devices from chip KCS2512, made with the single-lithography process. The dimensions of the devices are pillar area = $100 \times 100 \mu m^2$, pillar thickness = $50nm$, size of the slit's width = $2\mu m$ and the remaining YBCO thickness in the slit = $20nm$.

R(T) Measurements

Figure 6.1 (a) displays the $R(T)$ for three mesa devices, recorded using Mesa configuration. The only difference between these devices is that they are in different locations of the same chip. These different locations are included in the device name, where the device name contains the type of measurement (mesa or groove) and its location on the chip (for example device 21 refers to row 2, column 1 position on the chip). The observed $R(T)$ behavior deviates significantly from what is typically expected for c-axis transport in underdoped YBCO, as previously reported in [28]. Notably, there is no large characteristic upturn in resistance that would indicate a transition from metallic to semiconducting behavior, but only a very small one. Additionally, the absolute resistance values are roughly 40–50 times higher than our estimated R_c at 100 K (see **Chapter 5**), which strongly suggests excessive contact resistance, as that is the only factor outside of our calculations.

Although the Au contacts were deposited in-situ, immediately following the YBCO film growth, the interface between Au and underdoped YBCO appears to exhibit poor electrical coupling, likely due to intrinsic interfacial issues. This is believed to be the

main reason behind the elevated contact resistance, which obscures the intrinsic c-axis transport characteristics (meaning the upturn is less pronounced than expected).

In **Figure 6.1 (b)**, a subtle kink is visible around 38–40 K in all three devices, measured on different days but on the same chip. Due to its low temperature, we interpret this consistent feature as indicative of the superconducting transition along the c-axis. The hint of Andreev reflections at the interface, also makes us think of this as a superconducting feature [102].

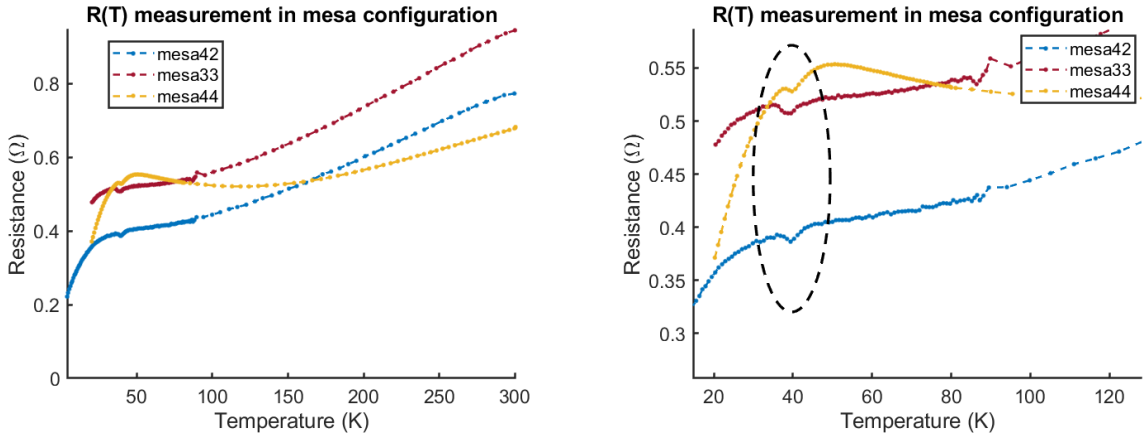

(a) R(T) for mesa devices 33, 42, 44

(b) Zoomed-in view near the upward kink region

Figure 6.1: R(T) curves for three different mesa devices using 3-point measurement configuration. The measured resistance includes both R_c and contact resistance.

Additional measurements were performed using the groove configuration, shown in **Figure 6.2 (a)**. Similar to the mesa measurements, the resistance values in the grooves also far exceed the expected estimates at 100 K by a factor of 40. This again suggests a dominant contribution from contact resistance, as well as damage of the slit region. Groove 1 (G1) corresponds to a two-point measurement between the central and left pillar, while Groove 2 (G2) measures between the central and right pillar.

Each groove consists of two pillars with c-axis transport contributions, separated by a narrow slit representing the ab-plane component. The $R(T)$ behavior indicates that the slit region is not superconducting, but ohmic. Nevertheless, the influence of the pillar structures on the measurement becomes evident upon closer inspection. As seen in **Figure 6.2 (b)**, we normalized each dataset by its resistance at 300 K (R_{300K}) to enable meaningful comparison. A distinct upward kink is present in both groove measurements as well as in the mesa configuration, occurring around 38–40 K. This further supports our identification of this feature as the c-axis superconducting transition, as the behavior is reflected both in mesa and groove configurations at the same temperature.

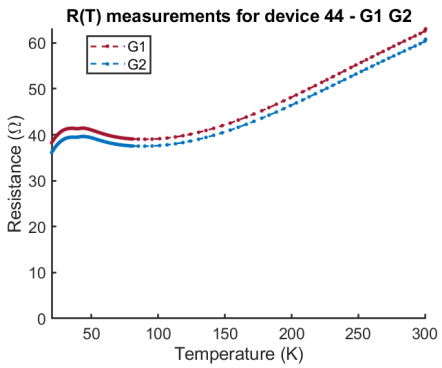

(a) R(T) for device 44 in Groove 1 (G1) and Groove 2 (G2) configurations

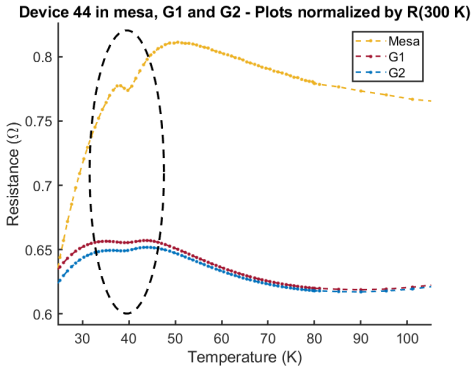

(b) Comparison of mesa, G1, and G2 configurations for device 44. All curves normalized by R_{300K}.

Figure 6.2: R(T) of device 44 measured in both mesa and groove geometries. The features around 38–40 K are consistent across configurations.

IVC Measurements

Figures 6.3 (a) and **(b)** show the differential conductance versus voltage characteristics for mesa devices 42 and 44, respectively. In both devices, a pronounced Zero Bias Conductance Peak (ZBCP) is observed at low temperatures, which gradually diminishes as the temperature increases. This behavior is indicative of superconductivity and is consistent with the formation of zero energy Andreev Bound States (ABS).

The presence of ZBCPs is characteristic of transport involving *ab*-plane (110) surface orientations rather than the expected *c*-axis (001) orientation. This effect is due to the roughness of the thin film combined with the large area of the pillar. As we will see when discussing the results of the three-lithography mesas, the differential conductance plots all show the expected V-shape, associated with (001) surfaces.

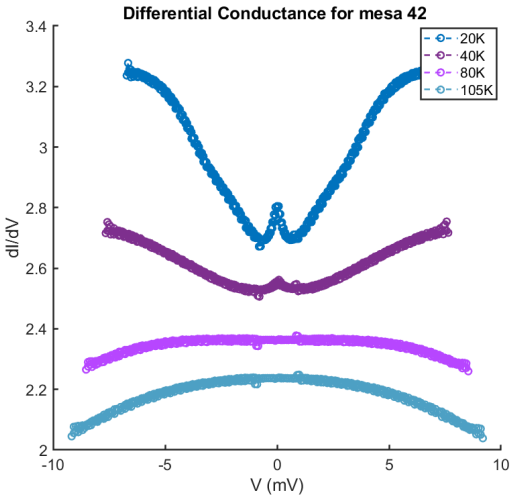

(a) Differential conductance plot for mesa 42

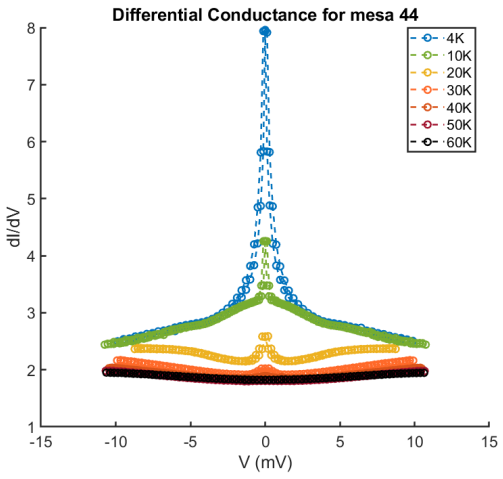

(b) Differential conductance plot for mesa 44

Figure 6.3: Differential conductance plots for mesa devices 42 and 44

Figure 6.4 shows the conductance behavior of mesa 33, which displayed a distinctly different profile compared to the other two devices. The reason for this different behavior is unknown to us, as this device experienced an unexpected increase of its resistance values by a factor of 10 within just 2 days. Other devices on the chip have been rather stable and showed no changes within the span of a month. Specifically, after this change, the mesa 33 device exhibited the desired V-shaped differential conductance curve, associated with c-axis (001) transport. Within this V-shaped feature, we observed an unusual subgap feature located around 3 meV.

By monitoring the evolution of this feature with temperature, we found that it gradually disappears above 10 K, as seen in **Figure 6.4 (b)**.

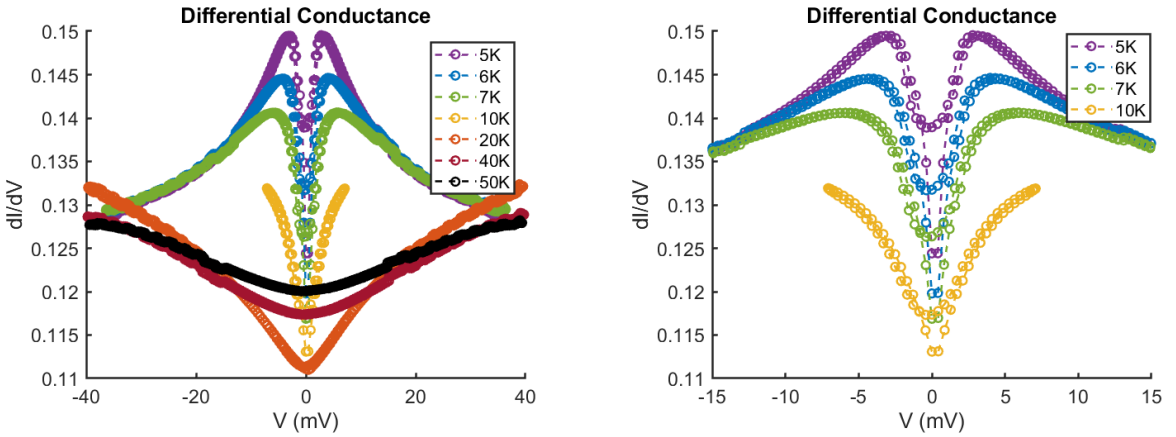

(a) Differential conductance for mesa 33

(b) Zoom-in on the subgap region for mesa 33

Figure 6.4: Differential conductance for mesa 33 at different temperatures

One possible explanation for this subgap feature involves the mixing of the d-wave superconducting order parameter from the CuO_2 planes with the s-wave order parameter from the CuO chains. Such mixing can give rise to new subgap states at energies corresponding to $d + s$ and $d - s$. Similar subgap features have previously been reported in overdoped YBCO, particularly in samples with Ca doping [3, 120], where they typically appear around 5 meV. However, since the CuO chain contribution is significantly stronger in overdoped compounds than in underdoped ones (as is the case in our samples), it is possible for the subgap feature to appear at a lower energy, such as the 3 meV observed here.

Of course, we cannot rule out that this is a feature related to the contacts, or a form of device degradation. In this regard, a future check would be to apply magnetic field, in order to suppress this subgap feature. Such an approach could help determine whether the feature is indeed linked to superconductivity.

Performing conductance spectroscopy in our current mesa devices is quite challenging due to the low resistance of our devices. The main reason is because it is difficult to observe high-energy features such as the superconducting gap (15–20 meV) or the pseudogap (around 35 meV), as we would need to supply very large currents, which would force our devices out of the superconducting state by overheating issues or surpassing the critical current (I_c) that the mesa device can sustain. Detecting these features would serve as confirmation that we are indeed probing intrinsic YBCO characteristics rather than contact-related effects. And would indicate that any other features observed would

be linked to YBCO properties. Although the low transparency of our interface increases resistance, (thereby assists conductance spectroscopy), still the currents required to reveal such features are larger than our devices can sustain. This is a limitation of the mesas under the current design.

6.2 Single-lithography Mesas KCS2512 - After Ozonation

Since contact resistance seemed to be cloaking the c-axis transport (weaker upturns), we performed ozonation on the fabricated chip. As previously reported by our group for nanowires [116], ozonation on non-encapsulated YBCO improves superconducting parameters and homogenizes the oxygen distribution at the interface, effectively reducing contact resistance. This improvement is also evident in our c-axis measurements. However, due to wire bonding challenges, even with 100×100 μm^2 contact pads, bonding on the same device proved difficult because the spacing between pillars is only 2 μm. Attempting to place two bonds on the middle pillar (position 2 in **Figure 5.4**) while keeping both wedges within the contact pad area was highly challenging. As a result, the measurements in this section were performed on newly bonded devices rather than those used in the previous section.

R(T) measurements

The improvement in contact resistance is clearly visible in **Figure 6.5**, where the $R(T)$ for device 31 is shown in both mesa and groove configurations.

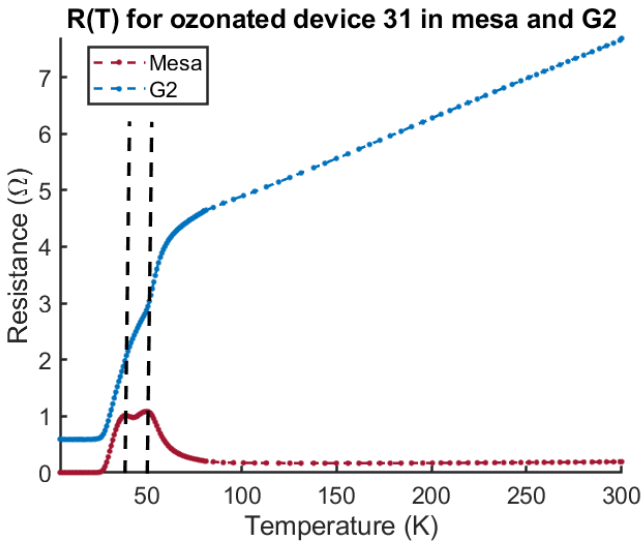

Figure 6.5: $R(T)$ of ozonated device 31 in mesa and groove configuration. The first dashed line at 50K is speculated to correspond with the few healed layers near the contact interface. The second dashed line at 38-40K is associated with the intrinsic c-axis transition of the pillar, which corresponds to the layers of YBCO which were not affected by ozonation. There are also two features evident in the G2 measurements, corresponding to these temperatures as well.

Despite this improvement, the measured resistance values are still higher than our estimations, by a factor of 16 for the mesa and 5 for the groove configuration. This discrepancy arises because the slit corresponds to the ion-milled region of the YBCO, which is the most damaged. Since ozonation is a non-homogenous healing process that redistributes oxygen to areas that have been depleted of it. It would seem the majority of the healing, or the greatest impact, is felt by the slit, which is quite reasonable as it is the area where ion-milled YBCO lies. Following ozonation, both the mesa and the groove regions exhibit superconductivity, with the residual resistance in the $R(T)$ curve attributable solely to contacts. The contact resistance for G2 seems to be higher than that of the mesa. A likely reason for this, is that ozonation is not a homogenous process, so the redistribution of oxygen at the interface is not the same for all contacts and in the G2 measurement, there are 2 contacts involved (that of the middle pillar in position 2, shared with the mesa, plus the contact of the pillar in position 3 **Figure 5.4**). One could conclude that the contact in position 3 is less healed than that of position 2. In addition, the groove measurement includes the slit as well, so that can account for some part of the high resistance observed in G2.

From **Figure 6.5**, two additional features are noteworthy. The first peak in the mesa $R(T)$, occurring at approximately 52K, likely corresponds to the transition of a few healed YBCO layers near the interface. The groove $R(T)$ curve also changes slope at this temperature and its resistance is higher than $2R_c + 2R_{contact}$, indicating that the slit is not yet superconducting. This suggests that this first kink could be associated with the pillar. The second peak occurs around 38–40K, which aligns with the c-axis temperatures previously observed in devices 42, 44, and 33 (before ozonation). This feature seems to persist after ozonation. At this temperature, the slit becomes fully superconducting. This is further corroborated by the resistance values: $R_{\text{groove}} = 2R_c + 2R_{\text{contact}}$, with $R_c = 1\ \Omega$ per pillar and the total groove resistance measured at 2 Ω. This correlation between the second kink in the mesa measurement and the fact that the $R_{G2} = 2R_c + 2R_{contact}$, leads us to believe that this kink is related to c-axis superconductivity. As for a potential reason, as to why we observe two transitions during our mesa measurement (unlike what has been reported in single crystals), we believe that due to ozonation, the first transition creates a healed layer near the interface by redistributing the oxygen, while the second corresponds to the other layers of YBCO which were not affected by the ozonation, therefore retaining the same temperature transition, as the one observed prior to ozone treatment. Of course, we cannot exclude the possibility, that there could be another explanation for this behavior.

As mentioned earlier, the effects of ozonation are not uniform across the chip, as the initial damage distribution is also non-uniform. Thus, different devices benefited differently from the healing process. **Figure 6.6(a)** presents the $R(T)$ of mesa 21, which showed more significant contact resistance reduction.

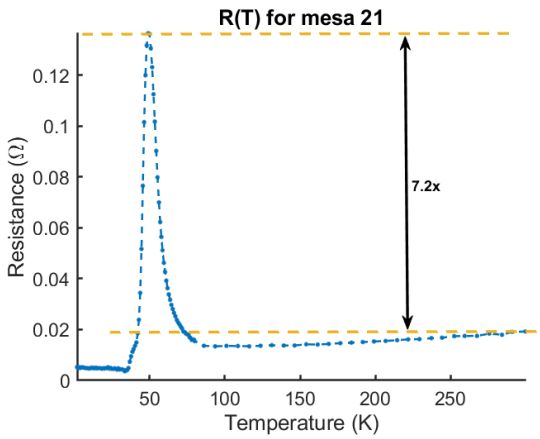

(a) $R(T)$ for ozonated mesa 21

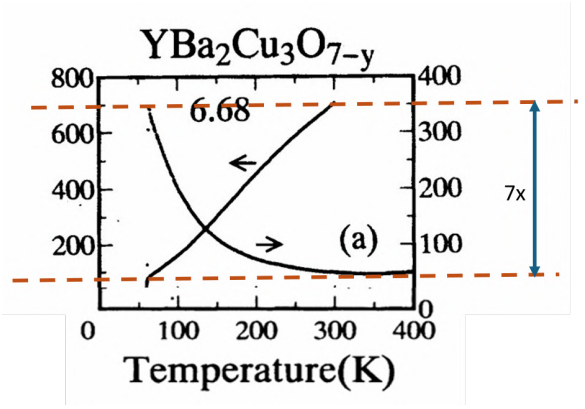

(b) Resistivity as a function of temperature for a single crystal with similar doping (adapted from [28])

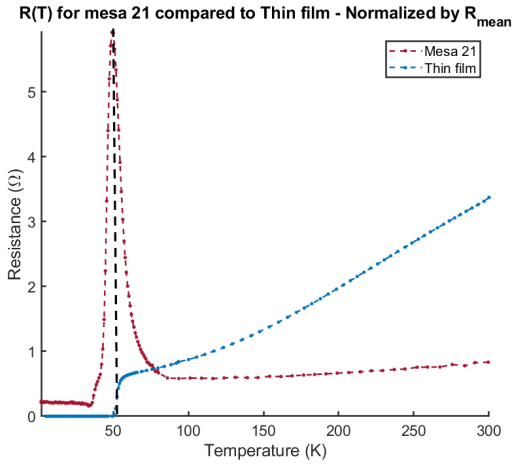

(c) Comparison of $R(T)$ between mesa 21 and the thin film

Figure 6.6: Comparisons with $R(T)$ in our thin film and $\rho(T)$ in single crystals.

Figure 6.6(a) clearly exhibits the desired upturn in c-axis transport. However, the transition between metallic and semiconducting behavior begins at a lower temperature compared to the one observed in single crystals. This discrepancy may still be influenced by residual contact resistance, which could have its own, unknown temperature dependence. As shown in **Figure 6.6(a)** and **(c)**, two transitions are evident: the first at 50K and the second at 39K (for which we attribute the same explanation as the one given for device 31 above). Comparing with the thin film data in **Figure 6.6(d)**, we observe that the first transition aligns closely with the thin film $\bar{T}_c$. This indicates that our ozone treatment does not change the YBCO doping above that of the thin film. Such a result aligns with has been observed before in our group [116].

Comparing the second transition, which we consider to be the true c-axis transition (layers unaffected by ozonation) with the thin film's ab-plane transition, they seem to occur at different temperatures. This could be an indication of anisotropy in transport between the two orientations, which is introduced by the reduced doping and dampening of the coupling between the CuO_2 planes. From this measurement and comparison alone, we cannot rule out the possibility, that the observed discrepancy is due to damage induced

during the fabrication (there were no nanobridges on this chip to represent ab-plane transport) or some influences by contact behavior.

For this device, the resistance values are also consistent with our estimates. Specifically, $R_{100K} = 0.013\ \Omega$, which is close to the calculated value of $0.011\ \Omega$. Furthermore, the increase in resistivity from 300 K to the onset of the upturn is approximately $7.2\times$, which aligns well with the $7\times$ increase reported in [28].

In conclusion, ozonation significantly improved the device interfaces, allowing us to observe the expected c-axis upturn behavior, consistent with the low doping level in YBCO. It also reinforced our earlier speculation that the pre-ozonation transition is indeed linked to c-axis superconductivity. Moreover, ozonation healed the slit regions, enabling superconductivity in them as well. Lastly, the effect of ozonation on the pillar's (c-axis) superconducting properties (besides a few layers near the interface), seem to have been mostly negligible, which can be attributed to the large area of the pillar and that only one ozonation was performed.

IVC measurements

The ozonation has improved the interface by lowering the resistance; however, this improvement has also made it more difficult to observe interesting spectroscopic features.

In **Figure 6.7(a)**, we observe the transition into the superconducting state, previously invisible due to contact resistance. What we mean by this, is that the ozonation improved the YBCO-Au interface, and left the superconducting properties of the pillar mainly unaffected. Therefore, the current (I) that we used to supply causes a smaller voltage drop than before ozonation. To reach voltage levels where gap-related features could be observed, we would need larger currents, which drive the system out of the superconducting state (as the supplied current becomes larger than the I_c of the pillar). Therefore, it is impossible to resolve these features as their voltages stand at $I > I_c$ now.

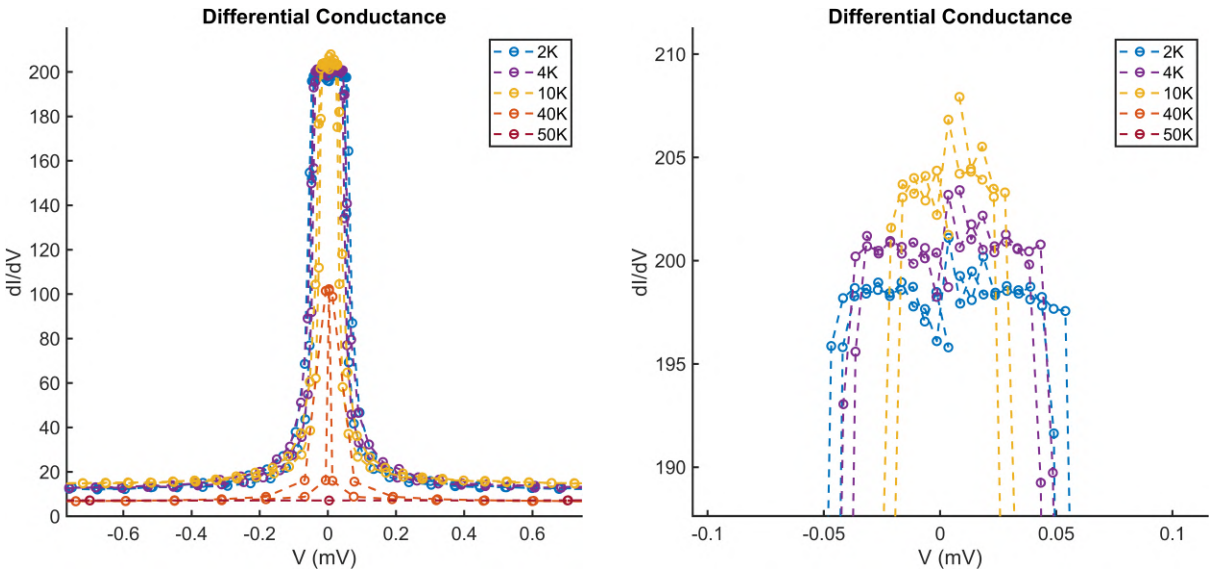

(a) Differential conductance for mesa 21 **(b)** Zoom-in on the superconducting region

Figure 6.7: Differential conductance for mesa 21 at different temperatures

The zoomed-in region in **Figure 6.7(b)** highlights the actual spectroscopic features observable in this device, corresponding to the superconducting state. The widening of

the central peak at lower temperatures is likely due to the sample's increased ability to sustain higher supercurrents as temperature decreases. A similar behavior was also observed in mesa 31.

Although ozonation improved the R(T) characteristics, it proved disadvantageous for conductance spectroscopy in the current configuration. This is due to the now much higher interface transparency and reduced contact resistance.

6.3 Three-lithography Mesas KCS2520

Single-lithography mesas treated with ozonation enabled the observation of the upturn behavior in c-axis transport. However, this approach introduced challenges such as low R_c and high contact resistances (before ozonation treatment), making c-axis $R(T)$ measurements difficult. Moreover, conductance spectroscopy predominantly revealed *ab*-plane features (from the (110) surface), such as zero-energy ABS, rather than the expected V-shaped spectra for the c-axis (001) orientation.

To overcome these limitations, we fabricated three-lithography mesas with smaller pillar areas ($10 \times 10\,\mu\mathrm{m}^2$), resulting in an increased R_c. The measurements remained in a three-point configuration, as described in **Chapter 5**. As mentioned in **Chapter 4**, multiple ozonation steps were used during fabrication, which likely enhanced the interface transparency, beyond what would be ideal for our measurements.

The dimensions of the mesa devices here were: pillar area = $100\mu m^2$, pillar thickness = $50nm$, slit width = $1\mu m$ and the YBCO thickness in the slit = $10nm$. This chip also contained 2 Au-shunted nanobridges with length = $3\mu m$ and width = $1\mu m$.

For these devices, we performed $R(T)$, $R(T)$ with magnetic field, and IVC measurements.

R(T) measurements

In **Figure 6.8(a)**, we compare the $R(T)$ of a Au-shunted nanobridge (length $l = 3\,\mu$m, width $w = 1\,\mu$m) to that of the pristine, bare thin film. The nanobridge was included for two primary reasons: (1) to quantify fabrication-induced damage by comparing it to the pristine film, and (2) to serve as a reference for *ab*-plane transport, complementing the mesa measurements. In **Figure 6.8(b)**, plotting the resistance on a log scale highlights two transitions in the Au-shunted nanobridge: the first corresponding to the electrodes (closer to the thin film), and the second to the constriction region of the bridge itself.

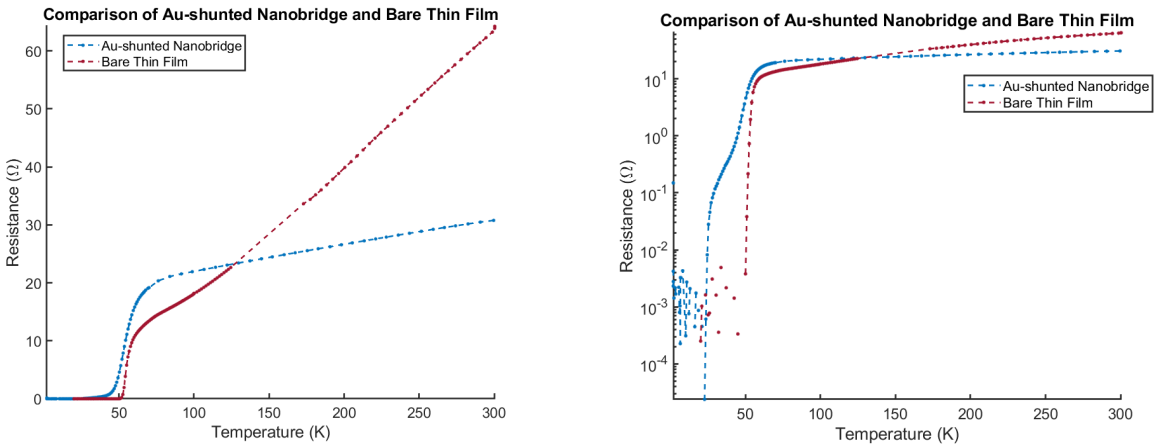

(a) Au-shunted Nanobridge vs. Bare thin film

(b) Log-scale: Comparison of Au-shunted Nanobridge and Bare Thin film

Figure 6.8: $R(T)$ comparison between Au-shunted nanobrige and bare thin film

This two transitions behavior has previously been observed by our group [121] for narrower nanowires and has been attributed to thermal phase slips, modeled using the vortex entry framework, but in higher YBCO dopings than the one used here. In this case, the tailing behavior was not expected to appear in nanobridges (width is much larger compared to the nanowires where the effect has been reported). However, in recent measurements of our group, in 10 nm thick, underdoped nanowires ($p \approx 0.11$), this tailing behavior was also observed for widths = 500 nm. As a further confirmation of this phenomena, in a previous sample, where the same Au-shunted nanobridge pattern (same dimensions and similar doping level) was fabricated, it revealed a tailing effect. Though the tailing of the single-lithography nanobridge was not as broad in temperature as the one of the three-lithography. This could imply that with underdoped samples (p=0.11) there is some degree of phase slips even for wider constrictions (bridges), though they may not be modeled with the standard vortex entry theory. Of course, some damage is expected to occur and influence the broadening observed in the three-lithography nanobridge's $R(T)$ data.

Based on **Figure 6.8**, we extract and compare the superconducting parameters of the Au-shunted nanobridge and the bare thin film:

Table 6.1: Extracted superconducting parameters for the bare thin film and the Au-shunted nanobridge

	T_c^{on}	$\bar{T}_c$	ΔT_c
Bare Thin Film	61 K	52.45 K	3.8 K
Au-shunted Nanobridge	64 K	52 K	11–12 K

The slight increase in T_c^{on} for the nanobridge aligns with expected ozonation effects [116]. However, the broader transition width (ΔT_c) suggests there has been some damage introduced during the multi-step fabrication process.

All devices on this chip exhibited superconductivity, and the mesa structures showed the upturn behavior in c-axis transport, a strong indication of a successful fabrication. Despite the challenges of underdoped YBCO and multiple lithography steps, the superconducting

properties were mostly preserved. Compared to large single-lithography mesas, the three-lithography design allowed c-axis features to emerge more evidently.

In **Figure 6.9**, we show $R(T)$ curves for devices A and C, comparing mesa and groove (G1) configurations. Both exhibit superconducting behavior. For device C, c-axis superconductivity's onset begins around 55 K, where the groove resistance is $R_{G1} \approx 41\,\Omega$ and the mesa resistance is $R_{\text{mesa}} \approx 20.4\,\Omega$, implying $R_{G1} = 2R_c + 2R_{\text{contact}}$. Similarly, for Device A, superconductivity starts near 58 K with $R_{G1} \approx 35\,\Omega$ and $R_{\text{mesa}} \approx 17.4\,\Omega$. This shows that the slit (area between 2 pillars where the $10nm$ ion-milled YBCO remains) is superconducting for both of these devices, as the only resistance visible in the groove measurement, is that of the 2 pillars (c-axis contribution plus contact). The remaining resistance at very low temperatures is attributed to the three-point contact geometry (residual contact resistance left).

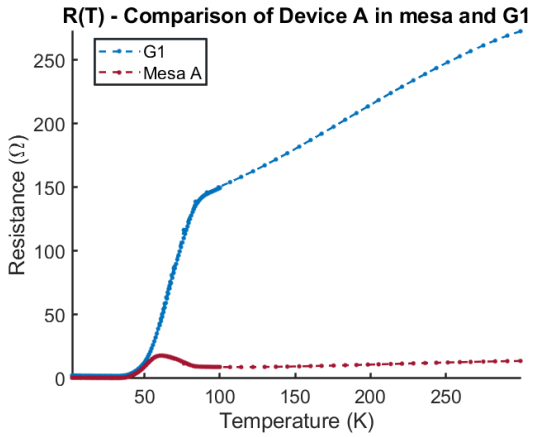

(a) $R(T)$ for Device A in mesa and G1 configurations

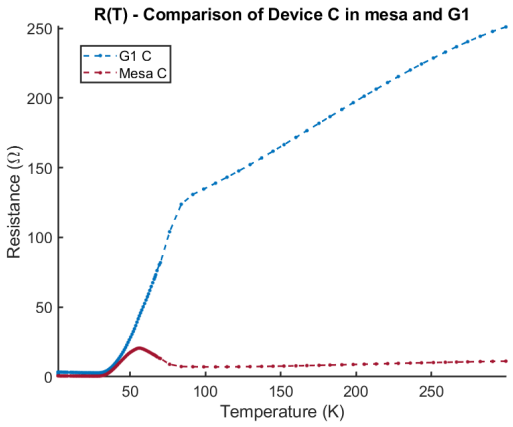

(b) $R(T)$ for Device C in mesa and G1 configurations

Figure 6.9: $R(T)$ for Devices A and C in mesa and groove (G1) configurations

The measured resistances for both configurations are significantly higher than expected, about 8× for mesas and 12× for grooves. This is likely due to contact resistance. Although multiple ozonation steps were used to enhance oxygen homogenization, their effect across the chip is nonuniform. Additionally, because mesas are encapsulated, ozone penetration is less effective compared to exposed *ab*-planes [116]. Furthermore, the presence of a new material, CeO_2, capping YBCO, may contribute to oxygen exchange between the two oxides during processing. This could introduce local oxygen inhomogeneities that are not fully recoverable by ozonation. Despite these limitations, observing upturns in mesas, and superconductivity in the slit, demonstrates a successful novel fabrication technique.

In **Figure 6.10**, we focus on Mesa Device C and summarize its superconducting parameters in table 6.3:

Table 6.2: Superconducting parameters for Mesa C

T_c^{on}	$\bar{T}_c$	ΔT_c	T_{c0}
55 K	43 K	18 K	32 K

In **Figure 6.10**, we also compare Mesa C with the Au-shunted nanobridge on the same chip. This contrast between in-plane and out-of-plane transport reveals some level of

anisotropy, indicating that at low doping, YBCO behaves as a quasi-2D superconductor. From panels (a) and (b) we can see a hint of 2D superconducting fluctuations in the ab-planes, as there is a decrease in the $R(T)$ of the nanobridge, while the c-axis remains resistive (the resistance even increases). This indicates a worsening of the Josephson interlayer coupling. Unfortunately, the temperature-dependent behavior of R_{ab} is not fully visible in the nanobridge measurement as the Au shunting, masks the true $R(T)$ start of the superconducting transition.

The behavior observed in these plots could be a hint of pair-density wave (PDW) order in YBCO, as it seems to follow a similar phenomenology reported in La-based cuprates [57, 58]. Although this is not conclusive evidence and further, complementary measurements are required to confirm this. In addition, proper 4-point investigation is needed to eliminate all contact effects.

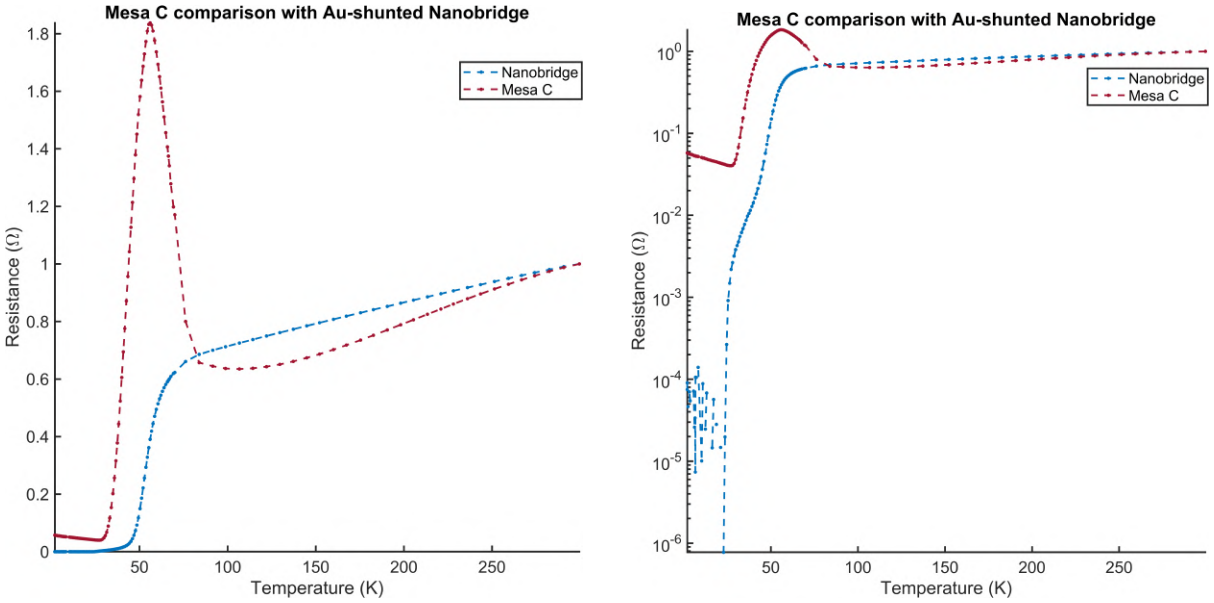

(a) $R(T)$ comparison: Mesa C vs. Au-shunted Nanobridge. Normalized by R_{300K}.

(b) Log scale $R(T)$ comparison: Mesa C vs. Au-shunted Nanobridge. Normalized by R_{300K}.

Figure 6.10: (a) and (b) display the $R(T)$ measurements in linear and log scale, comparing mesa C with the Au-shunted Nanobridge.

Figure 6.11 provides a summary of the $R(T)$ characteristics for various mesa devices on this chip. Each device exhibits a different value of $R_{300\,\mathrm{K}}$, pointing to variability in contact resistance. Devices E, C, and D display a T_c^{on} of approximately 55 K, while devices A and B reach $T_c^{\mathrm{on}} \approx 60\,\mathrm{K}$, and Mesa F shows $T_c^{\mathrm{on}} \approx 58\,\mathrm{K}$. The T_{c0} also vary: Device E reaches $T_{c0} \sim 24\,\mathrm{K}$; B and D, $\sim 42\,\mathrm{K}$; A and F, $\sim 38\,\mathrm{K}$—with A and F exhibiting nearly identical behavior after the onset; and C at approximately 32 K. These variations suggest both nonuniform contact resistances and oxygen inhomogeneities across the sample. Three primary factors could contribute to this variation:

1. **Oxygen exchange between YBCO and CeO_2**: During fabrication, several thermal processing steps may promote oxygen migration between the YBCO and CeO_2 layers.
2. **Nonuniform ozonation effect**: Ozonation of encapsulated YBCO induces oxygen redistribution, and this process likely differs between devices (in the previous section

we showed that the ozonation process is nonuniform across the chip for YBCO with ab-planes exposed). In contrast to Pt/Au-capped YBCO nanowires studied in [116], where oxygen diffusion into YBCO during ozonation is effectively blocked, our CeO_2 capping layer contains oxygen and may facilitate some oxygen exchange during this step.

3. **Thin film quality**: The film used in this fabrication appears slightly worse, compared to that employed in the single-lithography process. This impacts device performance and showcases again the challenges of working with thick (50 nm), underdoped YBCO films, as they are highly sensitive to the deposition conditions and often require repeated fine tuning over even short time periods.

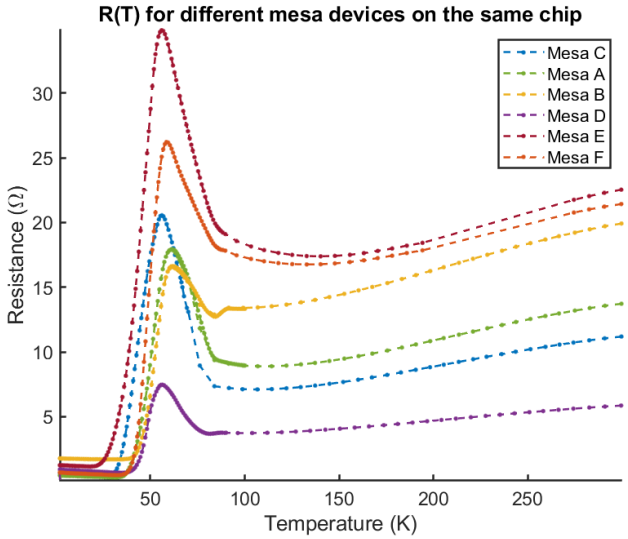

Figure 6.11: $R(T)$ summary for 6 devices on the chip

Another important aspect is the resistance increase from $R_{300\,\mathrm{K}}$ to T_c^{on}, corresponding to the onset of the c-axis transition. Based on results from single-lithography mesas and single-crystal studies in [28], for a doping level of $p \sim 0.11$, an increase of approximately 7× is expected. However, such behavior is not observed here, even though an upturn in resistance is clearly present. The measured resistance increases for each mesa device are as follows:

- Mesa E: 1.5×
- Mesa B: 0.8×
- Mesa F: 1.3×
- Mesa A: 1.3×
- Mesa C: 1.9×
- Mesa D: 1.3×

These suppressed ratios are most likely the result of contact resistance effects. In single-lithography mesas, we observed that prior to ozonation, the upturn was masked due to contact resistance, which was hiding the true c-axis behavior (upturn appeared weaker than it actually was and its starting temperature was also hidden). After ozonation, a metallic-to-semiconducting transition became clearly visible, but only Mesa 21 exhibited resistance values in agreement with our expectations and matched the 7x increase (Mesa 31 did not). In contrast, these devices show resistance values deviating from those estimations by factors ranging from 3× (Mesa D) to as high as 18× (Mesa E). To resolve this problem,

we would to need to employ 4-point measurements by fixing the design of the devices as elaborated in the end of **Chapter 4**.

A further distinction between single- and three-lithography mesas is seen in the number of transitions present in the $R(T)$ curves. In single-lithography mesas, two transitions were typically observed: one attributed to a healed region of the pillar near the interface, and the other to the unaffected layers by ozonation. In the current three-lithography devices, only a single transition is detected. Based on comparisons with Au-shunted nanobridge measurements, this has been identified as the *c*-axis transition, as it differs in behavior from the *ab* transition. The absence of the second transition in the mesa measurements, could come from a homogenization of the oxygen content in the pillar. This higher degree of homogenization, despite the encapsulation could arise from the multiple ozonation steps.

R(T) Under Magnetic Field Measurements

To further investigate the nature of c-axis transport, we performed temperature-dependent resistance measurements under various out-of-plane magnetic fields (where the magnetic field is parallel with the c-axis transport).

Figure 6.12 presents $R(T)$ curves for mesas E and F measured under applied magnetic fields of 0, 1, 3, 5, and 9 T. Both linear and logarithmic scales are shown to highlight features across a wide resistance range.

A notable feature in these measurements is that the magnetoresistance effect in the $R(T)$ curves begins at temperatures significantly higher than the c-axis's transition temperature T_c^{on}. In fact, the deviation starts around 85–90 K or higher, which exceeds even the T_c^{on} associated with ab-plane transport by at least 20-25 K.

Another unusual observation is a reduction in resistance at T_c^{on} for the c-axis under applied magnetic field. Typically, applying a magnetic field suppresses superconductivity, resulting in an increase in resistance and broadening of the transition. In our data, while the broadening is present, we do not observe the expected increase in resistance. Rather the resistance appears to decrease slightly at the onset. These behaviors were consistent and observed in all the magnetic measurements we conducted.

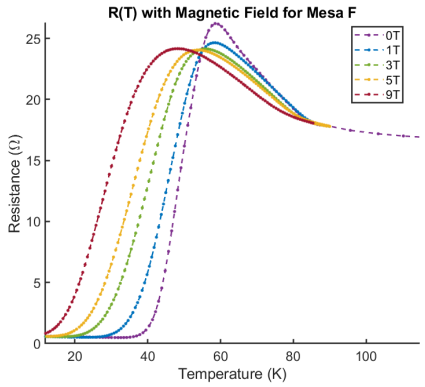

(a) $R(T)$ with magnetic field for Mesa F

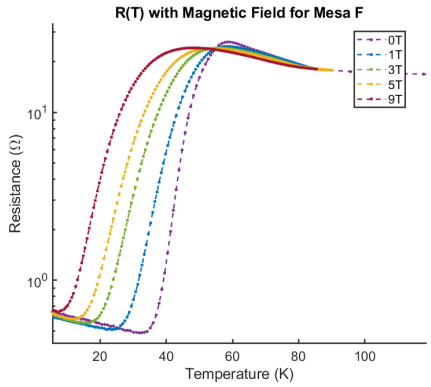

(b) $\log R(T)$ with magnetic field for Mesa F

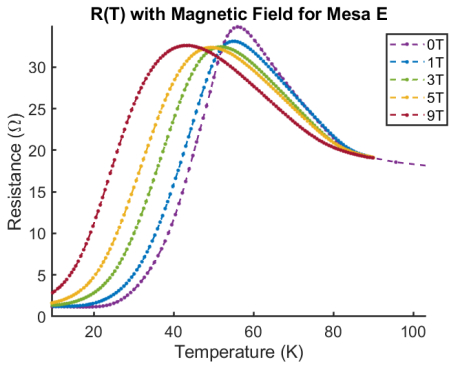

(c) $R(T)$ with magnetic field for Mesa E

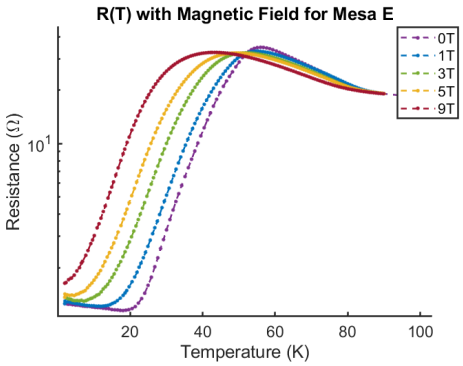

(d) $\log R(T)$ with magnetic field for Mesa E

Figure 6.12: $R(T)$ and $\log R(T)$ under magnetic fields (1, 3, 5, 9 T) for mesas E and F. The measurements show the evolution of the c-axis resistive transition with applied field.

From the observed behavior, it would seem that the magnetic field is somehow improving the coupling between the CuO_2 planes and it is affecting a state which lies 30-35 K above the c-axis transition. As for the mechanism behind it, further investigations are required and proper 4-point measurements to exclude any strange contact influences.

IVC Measurements

Lastly, we performed IVC measurements on the fabricated mesa devices. Unlike the single-lithography batch, all devices exhibited the expected V-shaped differential conductance, a hallmark of transport along the c-axis (001 direction).

However, due to the multiple ozonation steps necessary throughout the fabrication process, the Au-YBCO interface became more transparent than needed for our spectroscopy measurements. As a result, the currents required to resolve features associated with the superconducting gap or pseudogap were greater than our pillar's I_c. This was the same issue we experienced with single-lithography mesas, after ozonation.

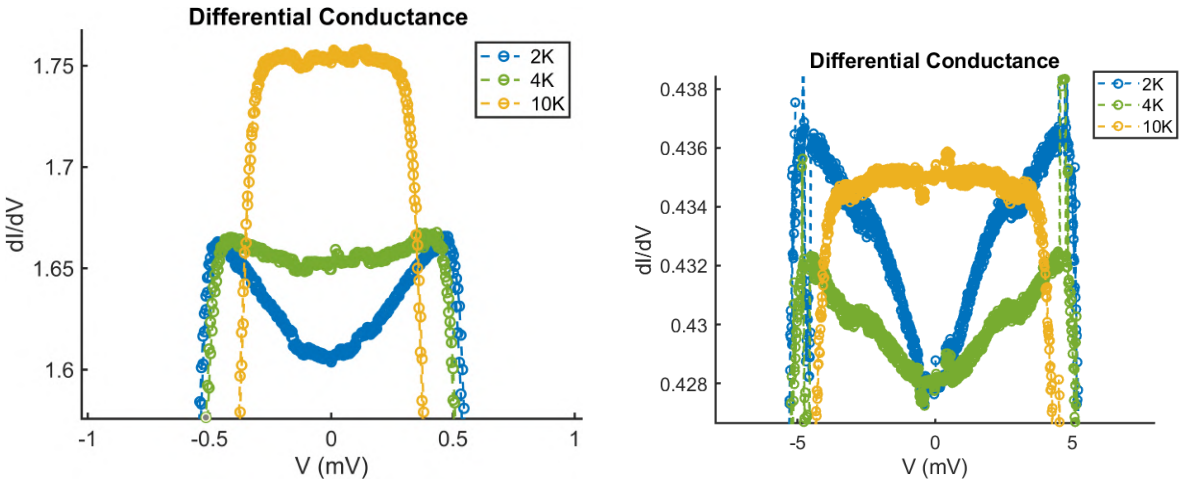

(a) Differential Conductance for mesa F **(b)** Differential Conductance for mesa B

Figure 6.13: Differential Conductance for 2 different mesa devices, F and B

In **Figure 6.13**, we present the differential conductance (dI/dV) spectra for two mesa devices, B and F. Nevertheless, a potential subgap feature was observed around 3 meV in **Figure 6.13(b)**, which appears at low temperatures and vanishes above 10 K. A similar feature was previously seen in the single-lithography mesas before ozonation (mesa 33 **Figure 6.4**). The same possibilities discussed there, apply to this device as well (see **single-lithography mesas before ozonation, the IVCs section**).

In a future work, we plan to perform differential conductance spectroscopy under magnetic fields, particularly on device B, to investigate whether this subgap feature exhibits a superconducting origin or is simply a measurement artifact.

In conclusion, the implementation of the 3-lithography process marked a clear improvement over the single-lithography approach. Specifically:

1. We successfully observed the transition from metallic to semiconducting behavior in all devices, as expected for underdoped c-axis transport.
2. $R(T)$ measurements showed a superconducting transition at lower temperatures along the c-axis, distinct from the one related to the ab-plane transport. This supports the picture of quasi-two-dimensional superconductivity in underdoped YBCO ($p \approx 0.11$), where interlayer coherence is decoupled from in-plane superconductivity (ab-planes become superconducting before the c-axis). As for any implications or confirmations of this fact, further investigations with 4-point measurements are required, as well as complementary measurements besides transport ones
3. All pillars and slit structures reached the superconducting state, indicating robust device fabrication.
4. While contact resistance remains a limiting factor, this can be addressed in future iterations by transitioning to a true 4-point measurement geometry via splitting of the central pillar's Au contact.
5. A peculiar magnetoresistance effect in $R(T, B)$ was observed, which occurred at much higher temperatures than the superconducting transition. It also improved the coupling between the CuO_2 planes, leading to a restoration of 3D superconducting behavior. Further work is required to investigate the mechanisms and origin of this effect.
6. We successfully probed the c-axis via differential conductance spectroscopy on (001) oriented surfaces, with the previously encountered zero-bias conductance peaks

(ZBCP) at zero energy, no longer present.
7. A potential subgap feature near 3 meV was detected again and warrants further investigation under field-dependent spectroscopy

7

Conclusion and Future Outlook

This thesis focused on creating a reliable platform for investigating the c-axis transport of YBCO thin films. With this goal in mind, mesa devices with a thickness of 50 nm were nanofabricated using two distinct approaches: single-lithography devices with a pillar area of 100×100 μm^2, and three-lithography devices with a reduced pillar area of 10×10 μm^2. On these devices we measured electrical, c-axis transport on underdoped ($p \approx 0.11$ YBCO thin films and compared with results from single crystal measurements to confirm the validity of our platform.

As a byproduct of our measurements and doping level of YBCO, we looked for hints of anisotropy in transport between the c-axis and ab-plane conduction, as YBCO is theorized to behave as a quasi-two-dimensional superconductor (and anisotropy should be more pronounced when going to the underdoped regime). In our three-lithography devices, we observed two different superconducting transitions, one associated with ab-plane (which started at slightly higher temperatures) and another for c-axis (which appeared at lower temperatures).

In the single-lithography devices, high contact resistance initially masked the c-axis behavior (the upturn in resistance was quite dampened compared to results from single-crystal data). Ozone treatment was used to effectively redistribute oxygen and improve the interface quality. Post-ozonation, we observed the characteristic upturn in $R(T)$, indicating a transition from metallic to semiconducting behavior, as expected for c-axis transport in underdoped YBCO. Moreover, the measured resistance values closely matched both our theoretical estimations and values reported for YBCO single crystals.

Spectroscopy measurements on the Au-YBCO interface revealed the presence of zero energy, Andreev bound states (related with (110) surfaces in YBCO) in the form of a zero-bias conductance peak in most devices prior to ozonation. One device exhibited a subgap feature near 3 meV, which may be attributed to order parameter mixing, or some other effect. A similar behavior was also observed on one of three lithography devices. This feature disappeared above 10 K.

Numerous fabrication challenges were overcome during this thesis, necessary for making the mesa devices, especially for the more complex three-lithography devices. This new process enabled the reliable fabrication of superconducting mesa nanostructures with reduced pillar areas. They provided a reliable platform for exploring c-axis transport phenomena across a wider range of doping levels, not just underdoped.

For the three-lithography devices, the transition from metallic to semiconducting in $R(T)$ was consistently observed, as expected with transport along the c-axis. Due to encapsulation, ozonation treatment was not as effective post-fabrication, leaving contact resistance still an issue. Nonetheless, all fabricated structures (including the 10 nm thick slits between pillars) exhibited superconductivity, marking this a big success for this fabrication route, especially considering the fragility of underdoped YBCO.

A peculiar magnetoresistance effect in $R(T)$ under magnetic field was observed, which

occurred at much higher temperatures than the superconducting transition. Magnetic field also improved the coupling between the CuO_2 planes, leading to a restoration of 3D superconducting behavior, which was quite odd and very unexpected. Further work is required to investigate the origin of this mechanism.

Differential conductance spectroscopy confirmed the V-shaped characteristics associated with c-axis tunneling in YBCO, and the previously observed ZBCP was absent. One device (mesa B) again showed a subgap feature at 3meV, reminiscent of the one seen in single-lithography mesa 33. This observation warrants further spectroscopy studies, particularly under magnetic field, to probe the potential superconducting origin of the feature.

Future Outlook

- **Implement true 4-point measurements in the three-lithography design.** This will eliminate contact resistance and allow more accurate probing of c-axis transport, removing the uncertainties from our results. It would also enable a detailed comparison between the upturn in $R(T)$ and the onset of the pseudogap in ab-plane transport, potentially uncovering a deeper connection between the two. Lastly, it will allow us to fully confirm the existence of two distinct transitions between the ab-plane and c-axis for underdoped samples.
- **Further reduce mesa area to $\sim 3 \times 3\ \mu\mathbf{m}^2$.** This would increase c-axis resistance to tens of ohms, enabling more stable measurements across a wider doping range, including overdoped samples. Such capability could enable the construction of a full phase diagram for c-axis transport in YBCO (to indicate at which doping level, the quasi-2D behavior appears and disappears).
- **Improve fabrication by controlling contact resistance** We propose limiting ozonation to a single step after the second IBE, to prevent the risks of CeO_2 microcracks and delamination. In addition, we plan to test alternative encapsulating materials such as Parylene-N, which can be removed via oxygen plasma. This approach would also decrease the number of ion-milling steps, which despite cryo-IBE remain the most damaging in our current process.
- **Perform shot noise measurements.** Thanks to the higher resistance in the current three-lithography platform, we can probe the nature of charge carriers in c-axis transport by analyzing shot noise characteristics.
- **Study c-axis transport in ultrathin (10 nm-20 nm) mesas** These structures could provide an indirect method for probing nematicity through its influence on c-axis transport properties.
- **Investigate the effect of induced superpotentials on c-axis transport** Testing mesa devices on substrates such as reconstructed MgO(110) surface (nanofacets are present) or those patterned with a superstructure that could induce a superpotential, modifying the ground state of YBCO. That would enable us to study these superpotential effects on the c-axis transport.This is the main, long-term goal, for which we developed the mesa platform.

Bibliography

[1] "Probing electronic nematicity and anisotropic electron-phonon coupling in strained YBCO nanowires — hdl.handle.net." `http://hdl.handle.net/20.500.12380/307676`.

[2] E. Wahlberg, R. Arpaia, G. Seibold, M. Rossi, R. Fumagalli, E. Trabaldo, N. B. Brookes, L. Braicovich, S. Caprara, U. Gran, G. Ghiringhelli, T. Bauch, and F. Lombardi, "Restored strange metal phase through suppression of charge density waves in underdoped $YBa_2Cu_3O_{7-\delta}$," *Science*, vol. 373, pp. 1506–1510, 2021.

[3] O. Millo and G. Koren, "What can andreev bound states tell us about superconductors?," *Philos. Trans. A Math. Phys. Eng. Sci.*, vol. 376, p. 20140143, Aug. 2018.

[4] C.-T. Chen, *Scanning tunneling spectroscopy studies of high-temperature cuprate superconductors*. PhD thesis, 2006.

[5] J. G. Bednorz and K. A. Müller, "Possible high T_c superconductivity in the Ba-La-Cu-O system," *Z. Phys. B Condens. Matter*, vol. 64, pp. 189–193, 1986.

[6] J. Bardeen, L. N. Cooper, and J. R. Schrieffer, "Theory of superconductivity," *Phys. Rev.*, vol. 108, p. 1175, 1957.

[7] A. Mourachkine, *Room-temperature superconductivity*. Cambridge Int Science Publishing, 2004.

[8] B. Lilia, R. Hennig, P. Hirschfeld, G. Profeta, A. Sanna, E. Zurek, W. E. Pickett, M. Amsler, R. Dias, M. I. Eremets, *et al.*, "The 2021 room-temperature superconductivity roadmap," *J. Phys. Condens. Matter.*, vol. 34, p. 183002, 2022.

[9] E. Morosan, D. Natelson, A. H. Nevidomskyy, and Q. Si, "Strongly correlated materials," *Adv. Mater.*, vol. 24, pp. 4896–4923, 2012.

[10] B. Keimer, S. A. Kivelson, M. R. Norman, S. Uchida, and J. Zaanen, "From quantum matter to high-temperature superconductivity in copper oxides," *Nature*, vol. 518, pp. 179–186, 2015.

[11] K. Chao, J. Spałek, and A. Oleś, "Canonical perturbation expansion of the Hubbard model," *Phys. Rev. B*, vol. 18, p. 3453, 1978.

[12] E. Carlson, S. Kivelson, D. Orgad, and V. Emery, "Concepts in high temperature superconductivity," *The Physics of Superconductors: Vol. II. Superconductivity in Nanostructures, High-T_c and Novel Superconductors, Organic Superconductors*, pp. 275–451, 2004.

[13] S. Sachdev and B. Keimer, "Quantum criticality," *Phys. Today*, vol. 64, pp. 29–35, 2011.

[14] J. Tahir-Kheli and W. Goddard 3rd, "Spinons and holons for the one-dimensional three-band hubbard models of high-temperature superconductors.," *Proc. Natl. Acad. Sci.*, vol. 90, pp. 9959–9962, 1993.

[15] J. Schrieffer, X. Wen, and S. Zhang, "Dynamic spin fluctuations and the bag mechanism of high-T_c superconductivity," *Phys. Rev. B*, vol. 39, p. 11663, 1989.

[16] B. Chakraverty and J. Ranninger, "Bipolarons and superconductivity," *Phil. Mag. B.*, vol. 52, pp. 669–678, 1985.

[17] P. W. Anderson, "The resonating valence bond state in La_2CuO_4 and superconductivity," *Science*, vol. 235, pp. 1196–1198, 1987.

[18] E. Fradkin, S. A. Kivelson, and J. M. Tranquada, "Colloquium: Theory of intertwined orders in high temperature superconductors," *Rev. Mod. Phys.*, vol. 87, p. 457, 2015.

[19] B. Vignolle, B. J. Ramshaw, J. Day, D. LeBoeuf, S. Lepault, R. Liang, W. N. Hardy, D. A. Bonn, L. Taillefer, and C. Proust, "Coherentc-axis transport in the underdoped cuprate superconductor YBa2Cu3Oy," *Phys. Rev. B Condens. Matter Mater. Phys.*, vol. 85, June 2012.

[20] J. Stajic, A. Iyengar, K. Levin, B. R. Boyce, and T. R. Lemberger, "Cuprate pseudogap: Competing order parameters or precursor superconductivity," *Phys. Rev. B Condens. Matter*, vol. 68, July 2003.

[21] K. M. Shen, F. Ronning, D. Lu, F. Baumberger, N. Ingle, W. Lee, W. Meevasana, Y. Kohsaka, M. Azuma, M. Takano, *et al.*, "Nodal quasiparticles and antinodal charge ordering in $Ca_{2-x}Na_xCuO_2Cl_2$," *Science*, vol. 307, pp. 901–904, 2005.

[22] D. Marshall, D. Dessau, A. Loeser, C. Park, A. Matsuura, J. Eckstein, I. Bozovic, P. Fournier, A. Kapitulnik, W. Spicer, *et al.*, "Unconventional electronic structure evolution with hole doping in $Bi_2Sr_2CaCu_2O_{8+\delta}$: Angle-resolved photoemission results," *Phys. Rev. Lett.*, vol. 76, p. 4841, 1996.

[23] K. Tanaka, W. Lee, D. Lu, A. Fujimori, T. Fujii, Risdiana, I. Terasaki, D. Scalapino, T. Devereaux, Z. Hussain, *et al.*, "Distinct fermi-momentum-dependent energy gaps in deeply underdoped Bi2212," *Science*, vol. 314, pp. 1910–1913, 2006.

[24] M. R. Norman, H. Ding, M. Randeria, J. C. Campuzano, T. Yokoya, T. Takeuchi, T. Takahashi, T. Mochiku, K. Kadowaki, P. Guptasarma, *et al.*, "Destruction of the fermi surface in underdoped high-T_c superconductors," *Nature*, vol. 392, pp. 157–160, 1998.

[25] W. Jiang, Y. Liu, A. Klein, Y. Wang, K. Sun, A. V. Chubukov, and Z. Y. Meng, "Monte carlo study of the pseudogap and superconductivity emerging from quantum magnetic fluctuations," *Nat. Commun.*, vol. 13, p. 2655, 2022.

[26] S. Hüfner, M. Hossain, A. Damascelli, and G. Sawatzky, "Two gaps make a high-temperature superconductor?," *Rep. Prog. Phys.*, vol. 71, p. 062501, 2008.

[27] J. Niu, M. O. Larrazabal, T. Gozlinski, Y. Sato, K. M. Bastiaans, T. Benschop, J.-F.

Ge, Y. M. Blanter, G. Gu, I. Swart, and M. P. Allan, "Equivalence of pseudogap and pairing energy in a cuprate high-temperature superconductor," 2024.

[28] K. Takenaka, K. Mizuhashi, H. Takagi, and S. Uchida, "Interplane charge transport in YBa2Cu3O7-y: Spin-gap effect on in-plane and out-of-plane resistivity," *Phys. Rev. B Condens. Matter*, vol. 50, pp. 6534–6537, Sept. 1994.

[29] G. Mirarchi, R. Arpaia, E. Wahlberg, T. Bauch, A. Kalaboukhov, S. Caprara, C. Di Castro, M. Grilli, F. Lombardi, and G. Seibold, "Tuning the ground state of cuprate high-critical-temperature superconducting thin films by nanofaceted substrates," *arXiv:2306.12335*, 2023.

[30] E. Wahlberg, *Reshaping the Phase Diagram of $YBa_2Cu_3O_{7-\delta}$ Through Strain in Ultrathin Films and Nanowires*. Chalmers Tekniska Hogskola (Sweden), 2021.

[31] R. Arpaia, N. Alcalde-Herraiz, A. D'Alessio, E. Stepantsov, E. Wahlberg, A. Kalaboukhov, T. Bauch, and F. Lombardi, "Engineering underdoped CuO2 nanoribbons in nm-thick a -axis YBa2Cu3O7δ films," *Phys. Rev. Mater.*, vol. 8, Apr. 2024.

[32] E. Wahlberg, R. Arpaia, D. Chakraborty, A. Kalaboukhov, D. Vignolles, C. Proust, A. M. Black-Schaffer, G. Seibold, T. Bauch, and F. Lombardi, "Boosting superconductivity: how nanofaceted surfaces transform the ground state of ultrathin $YBa_2Cu_3O_{7-\delta}$ thin films," 2025.

[33] R. Arpaia, E. Andersson, A. Kalaboukhov, E. Schröder, E. Trabaldo, R. Ciancio, G. Dražić, P. Orgiani, T. Bauch, and F. Lombardi, "Untwinned $YBa_2Cu_3O_{7-\delta}$ thin films on MgO substrates: A platform to study strain effects on the local orders in cuprates," *Phys. Rev. Materials*, vol. 3, p. 114804, 2019.

[34] R. Arpaia, E. Andersson, E. Trabaldo, T. Bauch, and F. Lombardi, "Probing the phase diagram of cuprates with $YBa_2Cu_3O_{7-\delta}$ thin films and nanowires," *Phys. Rev. Materials*, vol. 2, p. 024804, 2018.

[35] H. K. Onnes, "The resistance of pure mercury at helium temperatures. further experiments with liquid helium. IV," in *Proceedings Koninklijke Akademie van Wetenschappen te Amsterdam*, vol. 13, pp. 1274–1276, 1911.

[36] W. Meissner and R. Ochsenfeld, "Ein neuer effekt bei eintritt der supraleitfähigkeit," *Sci. Nat.*, vol. 21, pp. 787–788, 1933.

[37] F. London and H. London, "The electromagnetic equations of the supraconductor," *Proc. R. Soc. Lond.*, vol. 149, pp. 71–88, 1935.

[38] V. L. Ginzburg, V. L. Ginzburg, and L. Landau, *On the theory of superconductivity*. Springer, 2009.

[39] A. A. Abrikosov, "On the magnetic properties of superconductors of the second group," *Sov. Phys. J. Exp. Theor. Phys.*, vol. 5, pp. 1174–1182, 1957.

[40] E. Maxwell, "Isotope effect in the superconductivity of mercury," *Phys. Rev.*, vol. 78, p. 477, 1950.

[41] H. Fröhlich, "Theory of the superconducting state. I. the ground state at the absolute zero of temperature," *Phys. Rev.*, vol. 79, p. 845, 1950.

[42] J. Bardeen, "Zero-point vibrations and superconductivity," *Phys. Rev.*, vol. 79, p. 167, 1950.

[43] J. Bardeen, L. N. Cooper, and J. R. Schrieffer, "Microscopic theory of superconductivity," *Phys. Rev.*, vol. 106, p. 162, 1957.

[44] J. Bardeen, L. N. Cooper, and J. R. Schrieffer, "Theory of superconductivity," *Phys. Rev.*, vol. 108, p. 1175, 1957.

[45] W. McMillan, "Transition temperature of strong-coupled superconductors," *Phys. Rev.*, vol. 167, p. 331, 1968.

[46] M.-K. Wu, J. R. Ashburn, C. Torng, P.-H. Hor, R. L. Meng, L. Gao, Z. J. Huang, Y. Wang, and a. Chu, "Superconductivity at 93 K in a new mixed-phase Y-Ba-Cu-O compound system at ambient pressure," *Phys. Rev. Lett.*, vol. 58, p. 908, 1987.

[47] C. Namgung, J. Irvine, J. Binks, and A. West, "Orthorhombic-tetragonal transition in $YBa_2Cu_3O_x$," *Supercond. Sci. Technol.*, vol. 1, p. 169, 1988.

[48] J. Jorgensen, B. Veal, A. P. Paulikas, L. Nowicki, G. Crabtree, H. Claus, and W. Kwok, "Structural properties of oxygen-deficient $YBa_2Cu_3O_{7-\delta}$," *Phys. Rev. B*, vol. 41, p. 1863, 1990.

[49] R. Liang, D. Bonn, and W. Hardy, "Evaluation of CuO_2 plane hole doping in $YBa_2Cu_3O_{6+x}$ single crystals," *Phys. Rev. B*, vol. 73, p. 180505, 2006.

[50] J. Ye and K. Nakamura, "Quantitative structure analyses of $YBa_2Cu_3O_{7-\delta}$ thin films: Determination of oxygen content from x-ray-diffraction patterns," *Phys. Rev. B*, vol. 48, p. 7554, 1993.

[51] J. R. Waldram, *Superconductivity of metals and cuprates*. CRC Press, 1996.

[52] B. T. Matthias, T. H. Geballe, and V. B. Compton, "Superconductivity," *Rev. Mod. Phys.*, vol. 35, pp. 1–22, 1963.

[53] J. Eisenstein, "Superconducting elements," *Rev. Mod. Phys.*, vol. 26, p. 277, 1954.

[54] C. Tsuei and J. Kirtley, "Pairing symmetry in cuprate superconductors," *Rev. Mod. Phys.*, vol. 72, p. 969, 2000.

[55] M. Okawa, K. Ishizaka, H. Uchiyama, H. Tadatomo, T. Masui, S. Tajima, X.-Y. Wang, C.-T. Chen, S. Watanabe, A. Chainani, *et al.*, "Superconducting electronic state in optimally doped $YBa_2Cu_3O_{7-\delta}$ observed with laser-excited angle-resolved photoemission spectroscopy," *Phys. Rev. B*, vol. 79, p. 144528, 2009.

[56] T. Das and C. Panagopoulos, "Two types of superconducting domes in unconventional superconductors," *New J. Phys.*, vol. 18, p. 103033, 2016.

[57] D. F. Agterberg, D. S. Melchert, and M. K. Kashyap, "The physics of pair-density waves: Cuprate superconductors and beyond," *Annual Review of Condensed Matter Physics*, vol. 11, pp. 231–270, 2020.

[58] H. Huang, S.-J. Lee, Y. Ikeda, T. Taniguchi, M. Takahama, C.-C. Kao, M. Fujita, and J.-S. Lee, "Two-dimensional superconducting fluctuations associated with charge-density-wave stripes in La_{1.87}Sr_{0.13}cu_{0.99}Fe_{0.01}O_{4}," *Phys. Rev. Lett.*, vol. 126, p. 167001, Apr. 2021.

[59] P. A. Lee, N. Nagaosa, and X.-G. Wen, "Doping a Mott insulator: Physics of high-temperature superconductivity," *Rev. Mod. Phys.*, vol. 78, p. 17, 2006.

[60] D. Haug, V. Hinkov, Y. Sidis, P. Bourges, N. B. Christensen, A. Ivanov, T. Keller, C. Lin, and B. Keimer, "Neutron scattering study of the magnetic phase diagram of underdoped $YBa_2Cu_3O_{6+x}$," *New J. Phys.*, vol. 12, p. 105006, 2010.

[61] M. Kofu, S.-H. Lee, M. Fujita, H.-J. Kang, H. Eisaki, and K. Yamada, "Hidden quantum spin-gap state in the static stripe phase of high-temperature $La_{2-x}Sr_xCuO_4$ superconductors," *Phys. Rev. Lett.*, vol. 102, p. 047001, 2009.

[62] S. Badoux, S. Afshar, B. Michon, A. Ouellet, S. Fortier, D. LeBoeuf, T. Croft, C. Lester, S. Hayden, H. Takagi, *et al.*, "Critical doping for the onset of fermi-surface reconstruction by charge-density-wave order in the cuprate superconductor $La_{2-x}Sr_xCuO_4$," *Phys. Rev. X*, vol. 6, p. 021004, 2016.

[63] S. Lee, E. W. Huang, T. A. Johnson, X. Guo, A. A. Husain, M. Mitrano, K. Lu, A. V. Zakrzewski, G. A. de la Peña, Y. Peng, *et al.*, "Generic character of charge and spin density waves in superconducting cuprates," *Proc. Natl. Acad. Sci.*, vol. 119, p. e2119429119, 2022.

[64] A. Kanigel, M. R. Norman, M. Randeria, U. Chatterjee, S. Souma, A. Kaminski, H. M. Fretwell, S. Rosenkranz, M. Shi, T. Sato, T. Takahashi, Z. Z. Li, H. Raffy, K. Kadowaki, D. Hinks, L. Ozyuzer, and J. C. Campuzano, "Evolution of the pseudogap from fermi arcs to the nodal liquid," *Nat. Phys.*, vol. 2, pp. 447–451, July 2006.

[65] F. Cilento, G. Manzoni, A. Sterzi, S. Peli, A. Ronchi, A. Crepaldi, F. Boschini, C. Cacho, R. Chapman, E. Springate, H. Eisaki, M. Greven, M. Berciu, A. F. Kemper, A. Damascelli, M. Capone, C. Giannetti, and F. Parmigiani, "Dynamics of correlation-frozen antinodal quasiparticles in superconducting cuprates," *Sci. Adv.*, vol. 4, p. eaar1998, Feb. 2018.

[66] O. Cyr-Choinière, R. Daou, F. Laliberté, C. Collignon, S. Badoux, D. LeBoeuf, J. Chang, B. Ramshaw, D. Bonn, W. Hardy, *et al.*, "Pseudogap temperature T* of cuprate superconductors from the nernst effect," *Phys. Rev. B*, vol. 97, p. 064502, 2018.

[67] M. Zhu, D. Voneshen, S. Raymond, O. Lipscombe, C. Tam, and S. Hayden, "Spin fluctuations associated with the collapse of the pseudogap in a cuprate superconductor," *Nat. Phys.*, vol. 19, pp. 99–105, 2023.

[68] J. Chang, E. Blackburn, A. Holmes, N. B. Christensen, J. Larsen, J. Mesot, R. Liang, D. Bonn, W. Hardy, A. Watenphul, *et al.*, "Direct observation of competition between superconductivity and charge density wave order in $YBa_2Cu_3O_{6.67}$," *Nat. Phys.*, vol. 8, pp. 871–876, 2012.

[69] M. Huecker, N. B. Christensen, A. Holmes, E. Blackburn, E. M. Forgan, R. Liang, D. Bonn, W. Hardy, O. Gutowski, M. v. Zimmermann, *et al.*, "Competing charge, spin, and superconducting orders in underdoped $YBa_2Cu_3O_y$," *Phys. Rev. B*, vol. 90, p. 054514, 2014.

[70] S. Blanco-Canosa, A. Frano, E. Schierle, J. Porras, T. Loew, M. Minola, M. Bluschke,

E. Weschke, B. Keimer, and M. Le Tacon, "Resonant x-ray scattering study of charge-density wave correlations in $YBa_2Cu_3O_{6+x}$," *Phys. Rev. B*, vol. 90, p. 054513, 2014.

[71] J. Chang, E. Blackburn, A. T. Holmes, N. B. Christensen, J. Larsen, J. Mesot, R. Liang, D. A. Bonn, W. N. Hardy, A. Watenphul, M. v. Zimmermann, E. M. Forgan, and S. M. Hayden, "Direct observation of competition between superconductivity and charge density wave order in YBa2Cu3O6.67," *Nat. Phys.*, vol. 8, pp. 871–876, Dec. 2012.

[72] P. Fournier, P. Mohanty, E. Maiser, S. Darzens, T. Venkatesan, C. Lobb, G. Czjzek, R. A. Webb, and R. Greene, "Insulator-metal crossover near optimal doping in $Pr_{2-x}Ce_xCuO_4$: Anomalous normal-state low temperature resistivity," *Phys. Rev. Lett.*, vol. 81, p. 4720, 1998.

[73] M. Gurvitch and A. Fiory, "Resistivity of $La_{1.825}Sr_{0.175}CuO_4$ and $YBa_2Cu_3O_7$ to 1100 K: absence of saturation and its implications," *Phys. Rev. Lett.*, vol. 59, p. 1337, 1987.

[74] G. Baym and C. Pethick, "Landau fermi-liquid theory: concepts and applications," 2008.

[75] N. Hussey, K. Takenaka, and H. Takagi, "Universality of the Mott–Ioffe–Regel limit in metals," *Phil. Mag.*, vol. 84, pp. 2847–2864, 2004.

[76] S.-D. Chen, M. Hashimoto, Y. He, D. Song, K.-J. Xu, J.-F. He, T. P. Devereaux, H. Eisaki, D.-H. Lu, J. Zaanen, *et al.*, "Incoherent strange metal sharply bounded by a critical doping in Bi2212," *Science*, vol. 366, pp. 1099–1102, 2019.

[77] L. Chen, D. T. Lowder, E. Bakali, A. Andrews, W. Schrenk, M. Waas, R. Svagera, G. Eguchi, L. Prochaska, Q. Si, *et al.*, "Shot noise indicates the lack of quasiparticles in a strange metal," *Science*, vol. 382, pp. 907–911, 2023.

[78] J. Zaanen, "Planckian dissipation, minimal viscosity and the transport in cuprate strange metals," *SciPost Phys.*, vol. 6, p. 061, 2019.

[79] A. Legros, S. Benhabib, W. Tabis, F. Laliberté, M. Dion, M. Lizaire, B. Vignolle, D. Vignolles, H. Raffy, Z. Li, *et al.*, "Universal T-linear resistivity and Planckian dissipation in overdoped cuprates," *Nat. Phys.*, vol. 15, pp. 142–147, 2019.

[80] S. Sachdev, "Where is the quantum critical point in the cuprate superconductors?," *Phys. Status Solidi B*, vol. 247, pp. 537–543, 2010.

[81] B. Michon, C. Girod, S. Badoux, J. Kačmarčík, Q. Ma, M. Dragomir, H. Dabkowska, B. Gaulin, J.-S. Zhou, S. Pyon, *et al.*, "Thermodynamic signatures of quantum criticality in cuprate superconductors," *Nature*, vol. 567, pp. 218–222, 2019.

[82] G. Seibold, R. Arpaia, Y. Y. Peng, R. Fumagalli, L. Braicovich, C. Di Castro, M. Grilli, G. C. Ghiringhelli, and S. Caprara, "Strange metal behaviour from charge density fluctuations in cuprates," *Commun. Phys.*, vol. 4, p. 7, 2021.

[83] R. Arpaia and G. Ghiringhelli, "Charge order at high temperature in cuprate superconductors," *J. Phys. Soc. Jpn.*, vol. 90, p. 111005, 2021.

[84] R. Arpaia, L. Martinelli, M. M. Sala, S. Caprara, A. Nag, N. B. Brookes, P. Camisa, Q. Li, Q. Gao, X. Zhou, M. Garcia-Fernandez, K.-J. Zhou, E. Schierle, T. Bauch, Y. Y. Peng, C. Di Castro, M. Grilli, F. Lombardi, L. Braicovich, and G. Ghiringhelli, "Signature of quantum criticality in cuprates by charge density fluctuations," *Nat. Commun.*, vol. 14, p. 7198, 2023.

[85] J. Chang, M. Maansson, S. Pailhes, T. Claesson, O. Lipscombe, S. M. Hayden, L. Patthey, O. Tjernberg, and J. Mesot, "Anisotropic breakdown of Fermi liquid quasiparticle excitations in overdoped $La_{2-x}Sr_xCuO_4$," *Nat. Commun.*, vol. 4, p. 2559, 2013.

[86] Y. Peng, R. Fumagalli, Y. Ding, M. Minola, S. Caprara, D. Betto, M. Bluschke, G. De Luca, K. Kummer, E. Lefrançois, *et al.*, "Re-entrant charge order in overdoped $(Bi,Pb)_{2.12}Sr_{1.88}CuO_{6+\delta}$ outside the pseudogap regime," *Nat. Mater.*, vol. 17, pp. 697–702, 2018.

[87] L. Sederholm, S. D. Conradson, T. H. Geballe, C.-Q. Jin, A. Gauzzi, E. Gilioli, M. Karppinen, and G. Baldinozzi, "Extremely overdoped superconducting cuprates via high pressure oxygenation methods," *Condens. Matter*, vol. 6, p. 50, 2021.

[88] A. Augieri, T. Petrisor, G. Celentano, L. Ciontea, V. Galluzzi, U. Gambardella, A. Mancini, and A. Rufoloni, "Effect of Ca doping in YBCO superconducting thin films," *Physica C*, vol. 401, pp. 320–324, 2004.

[89] S. Nakata, M. Horio, K. Koshiishi, K. Hagiwara, C. Lin, M. Suzuki, S. Ideta, K. Tanaka, D. Song, Y. Yoshida, *et al.*, "Nematicity in a cuprate superconductor revealed by angle-resolved photoemission spectroscopy under uniaxial strain," *npj Quantum Mater.*, vol. 6, p. 86, 2021.

[90] S. A. Kivelson, E. Fradkin, and V. J. Emery, "Electronic liquid-crystal phases of a doped mott insulator," *Nature*, vol. 393, pp. 550–553, 1998.

[91] J. Tranquada, B. Sternlieb, J. Axe, Y. Nakamura, and S. Uchida, "Evidence for stripe correlations of spins and holes in copper oxide superconductors," *Nature*, vol. 375, pp. 561–563, 1995.

[92] H.-H. Kuo, J.-H. Chu, J. C. Palmstrom, S. A. Kivelson, and I. R. Fisher, "Ubiquitous signatures of nematic quantum criticality in optimally doped Fe-based superconductors," *Science*, vol. 352, pp. 958–962, 2016.

[93] F. Ronning, T. Helm, K. Shirer, M. Bachmann, L. Balicas, M. K. Chan, B. Ramshaw, R. D. Mcdonald, F. F. Balakirev, M. Jaime, *et al.*, "Electronic in-plane symmetry breaking at field-tuned quantum criticality in $CeRhIn_5$," *Nature*, vol. 548, pp. 313–317, 2017.

[94] R. Tao, Y.-J. Yan, X. Liu, Z.-W. Wang, Y. Ando, Q.-H. Wang, T. Zhang, and D.-L. Feng, "Direct visualization of the nematic superconductivity in $Cu_xBi_2Se_3$," *Phys. Rev. X*, vol. 8, p. 041024, 2018.

[95] R. S. Markiewicz, J. Lorenzana, G. Seibold, and A. Bansil, "Short range smectic order driving long range nematic order: example of cuprates," *Sci. Rep.*, vol. 6, pp. 1–7, 2016.

[96] A. Fedorov, A. Yaresko, T. Kim, Y. Kushnirenko, E. Haubold, T. Wolf, M. Hoesch,

A. Grüneis, B. Büchner, and S. Borisenko, "Effect of nematic ordering on electronic structure of FeSe," *Sci. Rep.*, vol. 6, pp. 1–7, 2016.

[97] S. Mukhopadhyay, R. Sharma, C. K. Kim, S. D. Edkins, M. H. Hamidian, H. Eisaki, S. Uchida, E.-A. Kim, M. J. Lawler, A. P. Mackenzie, *et al.*, "Evidence for a vestigial nematic state in the cuprate pseudogap phase," *Proc. Natl. Acad. Sci.*, vol. 116, pp. 13249–13254, 2019.

[98] Y. Ando, K. Segawa, S. Komiya, and A. Lavrov, "Electrical resistivity anisotropy from self-organized one dimensionality in high-temperature superconductors," *Phys. Rev. Lett.*, vol. 88, p. 137005, 2002.

[99] R. Daou, J. Chang, D. LeBoeuf, O. Cyr-Choiniere, F. Laliberté, N. Doiron-Leyraud, B. Ramshaw, R. Liang, D. Bonn, W. Hardy, *et al.*, "Broken rotational symmetry in the pseudogap phase of a high-T_c superconductor," *Nature*, vol. 463, pp. 519–522, 2010.

[100] Y. Sato, S. Kasahara, H. Murayama, Y. Kasahara, E.-G. Moon, T. Nishizaki, T. Loew, J. Porras, B. Keimer, T. Shibauchi, *et al.*, "Thermodynamic evidence for a nematic phase transition at the onset of the pseudogap in $YBa_2Cu_3O_y$," *Nat. Phys.*, vol. 13, pp. 1074–1078, 2017.

[101] G. Mirarchi, R. Arpaia, E. Wahlberg, T. Bauch, A. Kalaboukhov, S. Caprara, C. Di Castro, M. Grilli, F. Lombardi, and G. Seibold, "Tuning the ground state of cuprate superconducting thin films by nanofaceted substrates," *Commun. Mater.*, vol. 5, Aug. 2024.

[102] Guy Deutscher, "Andreev–Saint-James reflections: A probe of cuprate superconductors," *Rev. Mod. Phys.*, vol. 77, pp. 109–135, Mar. 2005.

[103] R. Prozorov and R. W. Giannetta, "Magnetic penetration depth in unconventional superconductors," *Supercond. Sci. Technol.*, vol. 19, pp. R41–R67, Aug. 2006.

[104] R. Arpaia, M. Arzeo, R. Baghdadi, E. Trabaldo, F. Lombardi, and T. Bauch, "Improved noise performance of ultrathin YBCO dayem bridge nanosquids," *Supercond. Sci. Technol.*, vol. 30, p. 014008, 2016.

[105] E. Trabaldo, C. Pfeiffer, E. Andersson, R. Arpaia, A. Kalaboukhov, D. Winkler, F. Lombardi, and T. Bauch, "Grooved dayem nanobridges as building blocks of high-performance $YBa_2Cu_3O_{7-\delta}$ SQUID magnetometers," *Nano Lett.*, vol. 19, pp. 1902–1907, 2019.

[106] R. Arpaia, M. Ejrnaes, L. Parlato, F. Tafuri, R. Cristiano, D. Golubev, R. Sobolewski, T. Bauch, F. Lombardi, and G. P. Pepe, "High-temperature superconducting nanowires for photon detection," *Physica C*, vol. 509, pp. 16–21, 2015.

[107] R. Arpaia, D. Golubev, R. Baghdadi, R. Ciancio, G. Dražić, P. Orgiani, D. Montemurro, T. Bauch, and F. Lombardi, "Transport properties of ultrathin $YBa_2Cu_3O_{7-\delta}$ nanowires: A route to single-photon detection," *Phys. Rev. B*, vol. 96, p. 064525, 2017.

[108] D. Schweitzer, T. Bollmeier, B. Stritzker, and B. Rauschenbach, "Twinning of $YBa_2Cu_3O_7$ thin films on different substrates," *Thin Solid Films*, vol. 280, pp. 147–151, 1996.

[109] B. Leridon, J. Vanacken, T. Wambecq, and V. V. Moshchalkov, "Paraconductivity of underdopedLa2xSrxCuO4thin-film superconductors using high magnetic fields," *Phys. Rev. B Condens. Matter Mater. Phys.*, vol. 76, July 2007.

[110] R. Liang, P. Dosanjh, D. Bonn, D. Baar, J. Carolan, and W. Hardy, "Growth and properties of superconducting YBCO single crystals," *Physica C*, vol. 195, pp. 51–58, 1992.

[111] R. Arpaia, S. Nawaz, F. Lombardi, and T. Bauch, "Improved nanopatterning for YBCO nanowires approaching the depairing current," *IEEE Trans. Appl. Supercond.*, vol. 23, pp. 1101505–1101505, 2013.

[112] S. Nawaz, R. Arpaia, F. Lombardi, and T. Bauch, "Microwave response of superconducting $YBa_2Cu_3O_{7-\delta}$ nanowire bridges sustaining the critical depairing current: Evidence of josephson-like behavior," *Phys. Rev. Lett.*, vol. 110, p. 167004, 2013.

[113] E. Andersson, R. Arpaia, E. Trabaldo, T. Bauch, and F. Lombardi, "Fabrication and electrical transport characterization of high quality underdoped $YBa_2Cu_3O_{7-\delta}$ nanowires," *Supercond. Sci. Technol.*, vol. 33, p. 064002, 2020.

[114] S. Charpentier, R. Arpaia, J. Gaudet, D. Matte, R. Baghdadi, T. Löfwander, P. Fournier, T. Bauch, and F. Lombardi, "Hot spot formation in electron-doped PCCO nanobridges," *Phys. Rev. B*, vol. 94, p. 060503, 2016.

[115] "Accurate nanofabrication techniques for high-index-contrast microphotonic devices — hdl.handle.net." `http://hdl.handle.net/1721.1/33169`.

[116] R. Baghdadi, R. Arpaia, S. Charpentier, D. Golubev, T. Bauch, and F. Lombardi, "Fabricating nanogaps inYBa2Cu3O7$\delta$for hybrid proximity-based josephson junctions," *Phys. Rev. Appl.*, vol. 4, July 2015.

[117] M. Chukharkin, A. Kalabukhov, J. F. Schneiderman, F. Öisjöen, O. Snigirev, Z. Lai, and D. Winkler, "Noise properties of high-tc superconducting flux transformers fabricated using chemical-mechanical polishing," *Appl. Phys. Lett.*, vol. 101, p. 042602, July 2012.

[118] Y. Qin, "Fabrication of cracking-free CeO2 thin film using UV/O3 and plasma treatment and their applications in wearable devices," 2019.

[119] H. Le-The, R. M. Tiggelaar, E. Berenschot, A. van den Berg, N. Tas, and J. C. T. Eijkel, "Postdeposition UV-ozone treatment: An enabling technique to enhance the direct adhesion of gold thin films to oxidized silicon," *ACS Nano*, vol. 13, pp. 6782–6789, June 2019.

[120] R. Prozorov and R. Giannetta, "Topical review: Magnetic penetration depth in unconventional superconductors," *Superconductor Science Technology - SUPERCONDUCT SCI TECHNOL*, vol. 19, 08 2006.

[121] R. Arpaia, D. Golubev, R. Baghdadi, M. Arzeo, G. Kunakova, S. Charpentier, S. Nawaz, F. Lombardi, and T. Bauch, "Resistive state triggered by vortex entry in YBa 2 cu 3 O 7δ nanostructures," *Physica C Supercond.*, vol. 506, pp. 165–168, Nov. 2014.